

BIOMECHANICAL ANALYSIS OF ACETABULAR DYSPLASIA:
FOUNDATIONS FOR IMPROVED CLINICAL CARE

by

Christine Louise Abraham

A dissertation submitted to the faculty of
The University of Utah
in partial fulfillment of the requirements for the degree of

Doctor of Philosophy

Department of Bioengineering

The University of Utah

December 2014

Copyright © Christine Louise Abraham 2014

All Rights Reserved

The University of Utah Graduate School

STATEMENT OF DISSERTATION APPROVAL

The dissertation of Christine Louise Abraham
has been approved by the following supervisory committee members:

Andrew E. Anderson, Chair 8/7/2014
Date Approved

Kenneth K. Foreman, Member 8/7/2014
Date Approved

Jeffrey A. Weiss, Member 8/7/2014
Date Approved

Richard D. Rabbitt, Member 8/7/2014
Date Approved

Christopher L. Peters, Member 8/7/2014
Date Approved

and by Patrick A. Tresco, Chair of
the Department of Bioengineering

and by David B. Kieda, Dean of The Graduate School.

ABSTRACT

Altered mechanics are believed to initiate osteoarthritis in hips with acetabular dysplasia. Periacetabular osteotomy (PAO) is the preferred surgical treatment; however, it is unknown if the procedure normalizes joint anatomy and mechanics. Changes in three-dimensional (3D) morphology and chondrolabral mechanics were quantified after PAO. Finite element (FE) models demonstrated that PAO improved the distribution of coverage, reduced stress, increased congruity, and prevented cartilage thinning. However, changes in mechanics were not consistent. In fact, one patient exhibited increased stress after surgery, which was believed to be a result of over-correction. Therefore, methods to integrate morphologic and biomechanical analysis with clinical care could standardize outcomes of PAO.

FE simulations are time-intensive and require significant computing resources. Therefore, the second aim was to implement an efficient method to estimate mechanics. An enhanced discrete element analysis (DEA) model of the hip that accurately incorporated cartilage geometry and efficiently calculated stress was developed and analyzed. Although DEA model estimates predicted elevated magnitudes of contact stress, the distribution corresponded well with FE models. As a computationally efficient platform, DEA could assist in diagnosis and surgical planning.

Imaging is a precursor to analyzing morphology and biomechanics. Ideally, an imaging protocol would visualize bone and soft-tissue at high resolution without ionizing

radiation. Magnetic resonance imaging (MRI) with 3D dual-echo-steady-state (DESS) is a promising sequence to image the hip noninvasively, but its accuracy has not been quantified. Therefore, the final aim was to implement and validate the use of 3D DESS MRI in the hip. Using direct measurements of cartilage thickness as the standard, 3D DESS MRI imaged cartilage to ~ 0.5 mm of the physical measurements with 95% confidence, which is comparable to the most accurate hip imaging protocol presented to date.

In summary, this dissertation provided unique insights into the morphologic and biomechanical features following PAO. In the future, DEA could be combined with 3D DESS MRI to efficiently analyze contact stress distributions. These methods could be incorporated into preoperative planning software, where the algorithm would predict the optimal relocation of the acetabulum to maximize femoral head coverage while minimizing contact stress, and thereby improve long-term outcomes of PAO.

To my parents, for their endless love, support, and encouragement

TABLE OF CONTENTS

ABSTRACT.....	iii
LIST OF TABLES.....	ix
LIST OF FIGURES.....	x
ACKNOWLEDGEMENTS.....	xii
CHAPTER	
1 BACKGROUND AND INTRODUCTION	1
1.1 The Hip Joint and Osteoarthritis.....	1
1.1.1 Hip Anatomy.....	1
1.1.2 Hip Osteoarthritis.....	3
1.2 Acetabular Dysplasia	5
1.2.1 Diagnosis.....	6
1.2.2 Treatment	7
1.3 Evaluation of Hip Joint Morphology	10
1.3.1 Radiographic Measures.....	10
1.3.2 Three-dimensional Characterization.....	12
1.4 Hip Joint Mechanics	15
1.4.1 Direct Measurement of Intra-articular Contact Mechanics	15
1.4.2 Computational Modeling Techniques.....	16
1.4.3 Finite Element Analysis (FEA) in the Hip.....	17
1.4.4 Discrete Element Analysis (DEA) in the Hip	20
1.5 Imaging the Hip Joint.....	25
1.5.1 Computed Tomography (CT) Imaging	25
1.5.2 Magnetic Resonance Imaging (MRI).....	27
1.6 Overall Motivation and Summary of Chapters.....	32
1.7 References.....	37
2 CHANGES IN FEMORAL COVERAGE AND CARTILAGE THICKNESS AFTER PERIACETABULAR OSTEOTOMY.....	60
2.1 Abstract.....	60
2.2 Introduction.....	61

2.3 Methods.....	63
2.3.1 Subject Selection and Image Acquisition	63
2.3.2 Three-dimensional Analysis of Femoral Head Coverage.....	64
2.3.3 Three-dimensional Plots of Cartilage Thickness	66
2.3.4 Statistical Analysis.....	66
2.4 Results.....	67
2.4.1 Femoral Head Coverage	67
2.4.2 Cartilage Thickness.....	68
2.5 Discussion.....	68
2.6 Acknowledgements.....	74
2.7 References.....	75
3 PATIENT-SPECIFIC CHONDROLABRAL MECHANICS IN ACETABULAR FOLLOWING PERIACETABULAR OSTEOTOMY	84
3.1 Abstract.....	84
3.2 Introduction.....	85
3.3 Methods.....	88
3.4 Results.....	90
3.5 Discussion.....	92
3.6 Acknowledgements.....	99
3.7 References.....	100
4 A NEW DISCRETE ELEMENT ANALYSIS METHOD FOR PREDICTING HIP JOINT CONTACT STRESSES	112
4.1 Abstract.....	112
4.2 Introduction.....	113
4.3 Methods.....	115
4.3.1 Discrete Element Analysis Implementation.....	115
4.3.2 Finite Element Analysis.....	117
4.3.3 Loading and Boundary Conditions	117
4.3.4 Data Analysis.....	118
4.3.5 Model Verification.....	119
4.4 Results.....	120
4.4.1 Contact Area	120
4.4.2 Contact Stress.....	121
4.4.3 Verification Results	121
4.4.4 Convergence and Computation Time	121
4.5 Discussion.....	122
4.6 Acknowledgements.....	127
4.7 References.....	128
5 3D DUAL ECHO STEADY STATE (DESS) MRI ACCURATELY QUANTIFIES ACETABULAR CARTILAGE THICKNESS	137

5.1 Abstract	137
5.2 Introduction	138
5.3 Methods	141
5.3.1 Injection, Traction, and Initial MRI Scan	141
5.3.2 Physical Measurements of Cored Cartilage Samples	142
5.3.3 Second MRI Scan	143
5.3.4 MRI Postprocessing	143
5.3.4.1 Segmentation and Three-dimensional Reconstruction	144
5.3.4.2 Spherical Cropping	146
5.3.4.3 Surface Alignment and Transformation	146
5.3.4.4 Cartilage Thickness	147
5.3.5 Data Analysis and Statistics	146
5.4 Results	147
5.5 Discussion	149
5.6 Acknowledgements	154
5.7 References	155
6 CONCLUSION	168
6.1 Summary and Impact	168
6.1.1 Morphology and Mechanics in PAO	169
6.1.2 Accurate and Time-efficient Predictions of Mechanics	170
6.1.3 3D DESS MRI of the Hip	172
6.2 Limitations and Future Directions	173
6.3 References	180

LIST OF TABLES

2.1 Radiographic Measures and Femoral Coverage by Quadrant Pre- and Postoperatively.....	78
--	----

LIST OF FIGURES

1.1. Surface reconstructions of a normal left hip joint.....	56
1.2. Differences in coverage between normal and dysplastic hips	57
1.3. Schematic of periacetabular osteotomy (PAO) for treatment of acetabular dysplasia	58
1.4. Midcoronal images of the hip joint.....	59
2.1. Radiographic measures of the anteroposterior pelvis view commonly used in the diagnosis of acetabular dysplasia.....	79
2.2. Pre- and postoperative 3D surface reconstructions of the femur and pelvis for each patient.....	80
2.3. Femoral coverage by quadrant displayed on the femur for patient # 1 pre- and postoperatively	81
2.4. Plots of acetabular and femoral cartilage thickness pre- and postoperatively for patient # 5.....	82
2.5. Average acetabular and femoral cartilage thickness overall and by region pre- and postoperatively	83
3.1. Finite element model representation for a single patient.	104
3.2. Regions of acetabular cartilage and labrum analyzed.....	105
3.3. Contact stress pre- and postoperatively for walking at midstance for each patient.	106
3.4. Average contact stress of all five patients pre- and postoperatively during all activities	107
3.5. Changes in acetabular cartilage mechanics postoperatively	108
3.6. Changes in labral mechanics postoperatively	109
3.7. Peak congruency (most congruent point indicated by minimum RMS value) and average congruency during WM and AH overall, and by region	110
3.8. Displacement of cartilage and labrum for a representative dysplastic hip during walking at toe-off.....	111

4.1. Sagittal view of DEA representation.....	131
4.2. Schematic of verification problem under 2000 N load.....	132
4.3. Contact stress patterns corresponded well between DEA and FEA for walking (W), descending stairs (DS), and ascending stairs (AS)	133
4.4. DEA contact areas were comparable to FEA predictions for walking (W), descending stairs (DS), and ascending stairs (AS).	134
4.5. Box plots of cartilage contact stress for the DEA and FEA models under conditions of walking (W), descending stairs (DS), and ascending stairs (AS).....	135
4.6. Comparisons of contact stresses predicted by FEA and DEA to an analytical solution.....	136
5.1. Schematic of custom traction frame made of polyvinylchloride.....	160
5.2. Photo illustration of cartilage core positioning and cross-sectional measurements.....	161
5.3. MRI postprocessing workflow.....	162
5.4. Segmentation and surface reconstructions of cortex and cartilage.....	163
5.5. Regions where automatic segmentation failed to delineate bone-cartilage and cartilage-saline boundaries correctly on qualitative visual inspection	164
5.6. Cartilage thickness plots of both hips from one cadaver..	165
5.7. Bland Altman plots comparing physical and MRI measurements.....	166
5.8. Scatterplot of physical thickness versus MRI thickness	167

ACKNOWLEDGEMENTS

First and foremost, I would like to express my deepest gratitude to my advisor, Dr. Andrew Anderson, for his continuous support, patience, and motivation throughout my graduate studies. This dissertation would not have been possible without his diverse knowledge of biomechanical modeling, hip pathology, and imaging. I would also like to recognize Dr. Jeffrey Weiss for his expertise, guidance, and active involvement in my research, especially in regard to computational modeling. Thank you to Dr. Christopher Peters for being a strong advocate of my research and providing clinical perspective and technical support when needed. I am also greatly appreciative of the extensive knowledge that Dr. Bo Foreman bestowed upon me, which helped shape this dissertation. I would like to thank Dr. Richard Rabbitt for providing critical feedback and offering a fresh perspective on my research.

Thank you to the many individuals who I have learned from over the years: Dr. Neal Bangerter, Dr. Kent Bachus, Dr. Heath Henninger, Dr. Steve Aoki, Jill Erickson, Dr. Bruce MacWilliams, Dr. Ashley Kapron, Dr. Michael Harris, Dr. Corinne Henak, Dr. Niccolo Fiorentino, Dr. Shawn Reese, Dr. Lowell Edgar, Dr. Benjamin Ellis, Andrew Guss, Alex Drew, Steve Maas, David Rawlins, Penny Atkins, Koren Roach, and Christopher Kolz. Finally, thank you to the many undergraduates who assisted throughout my tenure: Lance McGavin, Spencer Knight, Mikey Kutschke, Blake Zimmerman, Sean Kelly, Trevor Hafer, Tyler Skinner, Austin West, and Justine Goebel.

I would also like to recognize the financial support I received through scholarships and fellowships. A special thanks to the donors, orchestrators, and distributors of the College of Engineering Wayne Brown Fellowship, Department of Orthopaedics Obyn Memorial Endowed Scholarship, and the Louis S Peery Discovery Program in Musculoskeletal Restoration. Specifically, I cannot thank LeAnn Chandler and Art Swindle enough for their assistance and support.

To all my friends and family, thank you for being my biggest supporters throughout this arduous process. I could not have done this without you.

CHAPTER 1

BACKGROUND AND INTRODUCTION

1.1 The Hip Joint and Osteoarthritis

The hip is a diarthrodial joint comprised of the proximal head of the femur and acetabulum of the pelvis (Fig. 1.1). It is the largest weight-bearing joint of the body and carries loads of 2.5 to 5 times bodyweight²⁻⁴. The hip joint is central to mobility, and plays an active role in nearly all activities of daily living. Therefore, diseases of the hip have a debilitating effect, impacting mobility and overall quality of life⁵⁻⁷.

1.1.1 Hip Anatomy

The hip is described as a ball and socket joint, where the femoral head represents the ball and the acetabulum is the socket (Fig. 1.1). The acetabulum forms at the union of the ilium, ischium, and pubis bones. The articulating surfaces of the acetabulum and femoral head are covered with hyaline cartilage. In the acetabulum, cartilage has a horseshoe-shape and covers the lunate surface of the bone. On the femur, cartilage covers the entire femoral head, approximating a sphere (Fig. 1.1).

Hyaline cartilage provides a smooth, lubricated surface for low friction articulation between the femoral head and acetabulum. In the hip joint, average acetabular cartilage thickness is approximately 1.5 mm in healthy hips⁸⁻¹⁰. Despite being

thin, the internal structure of cartilage enables effective distribution of loads to underlying subchondral bone¹⁰⁻¹². Cartilage is composed of a dense extracellular matrix (ECM) and a sparse distribution of specialized cells termed chondrocytes¹¹⁻¹⁵. The ECM is a highly organized structure consisting of water, collagen, and proteoglycans with glycosaminoglycan side chains^{11,14,16}. Although porous, the components of the ECM help to retain water within the matrix, which is critical for maintaining the mechanical properties of cartilage. ECM is produced and repaired by the only metabolically active cells in cartilage, chondrocytes. In the absence of blood supply and lymphatics, nutrient delivery of cartilage relies on diffusion and osmosis, which is facilitated by movement of interstitial fluid through the ECM^{15,17}.

Cartilage structure is classified into zones by depth. Each zone has specific material properties that reflect its functional role. The superficial zone is the thinnest and contains collagen fibrils that lie parallel to the articular surface, which results in greater tensile stiffness and strength than deeper zones^{11,13-15}. The middle zone is the largest, accounting for 40% to 60% of total cartilage volume^{12,15}. Compared to the superficial zone, chondrocytes are more spherical and thicker collagen fibrils are randomly arranged¹³⁻¹⁵. The deep zone provides the greatest resistance to compressive forces^{12,15}. Here, collagen fibrils have the largest diameter and are aligned perpendicular to the articular surface^{11,12,15,18}. The deepest layer is partially calcified and anchors collagen fibrils of the deep zone to underlying subchondral bone^{13-15,18}.

The acetabular labrum is a triangular-shaped, fibrocartilaginous ring that encircles the acetabular rim¹⁹⁻²¹. The labrum is continuous with the acetabular cartilage, and attaches to the bony acetabular rim and joint capsule^{20,22} (Fig. 1.1). It provides extra joint

stability by effectively deepening the socket and increases the surface area of the acetabulum by as much as 27%^{1,23-25}. Similar to cartilage, the structure of the labrum is separated by layers. The inner layer primarily consists of circumferential bundles of type I collagen, while the outer layer of the labrum contains mostly types I and II collagen²⁶. The ability of the labrum to repair is likely limited as vascular supply is only available at the peripheral regions²⁶.

1.1.2 Hip Osteoarthritis

Osteoarthritis (OA) is the painful degradation of tissues within the joint, and is characterized by articular cartilage deterioration, hypertrophy of subchondral bone, and thickening of the capsule²⁷⁻²⁹. Hip OA affects approximately 10% of the population over age 60³⁰, and accounts for nearly 200,000 total hip replacements per year in the US³¹. Known risk factors for idiopathic hip OA include increased age, elevated body-mass index, genetic predisposition, and a history of participation in activities that excessively load the hip³¹⁻³³. Secondary hip OA can occur from systemic diseases that affect joint tissue health^{29,31} or from localized damage to the joint due to trauma or developmental deformities, such as acetabular dysplasia^{31,34,35}.

The symptoms of hip OA can be debilitating and include persistent pain, stiffness, and limited range of motion^{14,29}. Diagnosis involves patient history, physical exam, and radiographic findings of cartilage and/or bone degeneration^{11,31}. Pain in the lateral and anterior thigh and groin, morning stiffness, and pain with prolonged activity are characteristic of hip OA^{29,31}. Typical findings on physical examination include antalgic gait, restricted motion, pain with internal rotation, and crepitus with motion^{11,29}.

Radiographic examination of hips with OA reveals joint space narrowing indicative of cartilage thinning, the presence of subchondral sclerosis and cystic formation, and femoral head and neck remodeling^{29,36}.

OA affects all tissues in the joint including articular cartilage, subchondral bone, synovium, ligaments, joint capsules, and surrounding musculature. However, the primary changes involve the loss of cartilage, remodeling of subchondral bone, and formation of osteophytes^{11,37}. The early changes observed in cartilage degeneration include tissue swelling and reduced proteoglycan content^{11,38,39}. Impaired chondrocytes are unable to properly maintain the ECM, which disrupts regulation of interstitial fluid flow, and ultimately results in increased water content^{11,39,40}. Surface fibrillation and cracking are the initial signs of matrix failure; degeneration progresses to eventual full thickness cartilage loss^{11,39}. At end-stage OA, subchondral cysts and osteophytes form over regions of eroded cartilage³⁹.

Treatment for hip OA aims to relieve pain and preserve joint function. In the earlier stages of hip OA, exercise and physical therapy regimes have demonstrated mixed results at relieving symptoms^{41,42}. Patient education and the use of a walking aide to reduce load transfer of the affected hip can be efficacious at reducing symptoms^{43,44}. Conservative management with pharmacologic agents has demonstrated the most success. However, side-effects of medication are common, especially with prolonged use^{31,45-47}. Ultimately, many patients with hip OA require total hip arthroplasty to relieve symptoms^{31,48}.

No single intervention has been shown to restore cartilage or completely curtail the degenerative processes of OA. Therefore, prevention of advanced hip OA is critical,

and perhaps the most effective “treatment”. While certain risk factors are unavoidable, lifestyle modifications including activity restrictions and maintenance of healthy weight can reduce the risk of joint damage. Underlying bony deformities including acetabular dysplasia have been identified as a primary cause of hip OA^{34,35,49}. When present, correction of structural deformities may improve biomechanics and protect the hip from mechanical overload. Therefore, a large component of OA treatment, especially within the last decade, is focused on early diagnosis and surgical correction of geometrical abnormalities to delay or prevent end-stage arthrosis.

1.2 Acetabular Dysplasia

Acetabular dysplasia is defined by an under-developed, shallow acetabulum, which results in reduced femoral coverage and joint instability (Fig. 1.2). In cases of severe and untreated dysplasia, the femur can be chronically dislocated, creating a pseudo-acetabulum⁵⁰. Acetabular dysplasia often presents at birth, and is termed developmental dysplasia of the hip (DDH). Screening for DDH is standard for newborns and consists of manipulation of the hips to ensure normal motion^{51,52}. While cases of moderate to severe dysplasia are often diagnosed and treated during infancy or early childhood, dysplasia may go unnoticed until skeletal maturity in many individuals. It is unclear if acetabular dysplasia in adults is a mild form of DDH, or if it is a variant of dysplasia that presents differently, perhaps during the final period of growth^{53,54}. The focus of the work herein is treatment of acetabular dysplasia in adults.

The prevalence of radiographic acetabular dysplasia in adults is estimated at between 1.7% and 20% depending on the radiological measurement method^{55,56}. Many of

the risk factors for dysplasia are related to development in the womb^{50,52}. It is believed that the position of the fetus and exposure to certain hormones in utero may have a large influence on the development of the hip^{50,52}. Additional risk factors for dysplasia include being female, first-born, breech position, and having a high birth weight^{50-52,57,58}. Finally, a family history of dysplasia may also increase risk through an autosomal dominant inheritance pattern with variable expression in some cases⁵⁹.

1.2.1 Diagnosis

Acetabular dysplasia is diagnosed based on patient history and radiographic findings⁶⁰. Patients may present with symptoms of persistent groin pain exacerbated by activity, reports of an unstable hip that “gives way”, hypermobility, or mechanical symptoms^{51,60,61}. The onset of pain is typically insidious; however, in some cases a traumatic event or dramatic change in activity level (i.e. training for a marathon) may trigger symptoms. A gradual onset of pain points to damage associated with chronic overload, while a sudden onset may be indicative of labral injury.

Clinical evaluation of patients with dysplasia may reveal subtle alterations in gait, strength, and range of motion. Patients with dysplasia ambulate with reduced hip extension and increased pelvic drop⁶²⁻⁶⁴. Changes in hip extension are likely a consequence of pain avoidance, while pelvic drop may be a result of muscle weakness. Trendelenburg gait presents if the abductors are profoundly weakened; it is characterized by a drop in the contralateral pelvis during the single leg stance phase of walking. During ambulation, the lateral trunk moves towards the weight-bearing limb to counterbalance the drop in the contralateral pelvis^{60,65}. Patients with acetabular dysplasia usually

demonstrate normal passive range of motion or even hypermobility due to reduced femoral coverage allowing a larger range of motion⁶⁰. To identify chondrolabral damage at the acetabular rim, an impingement exam is performed. In this test, the hip is passively flexed to 90 degrees, adducted by 10 degrees, and internally rotated by 10-15 degrees^{61,66}. If damage is present, the impingement test typically reproduces symptoms of pain⁶¹. The apprehension test is more specific for identifying hip dysplasia as it is an evaluation of hip stability and anterior coverage. Here, with the patient supine, the hip is extended and externally rotated. Patients who have reduced femoral coverage anteriorly describe a feeling of discomfort and instability⁶⁷.

The combination of clinical exam and radiographic findings are necessary to confirm the diagnosis of acetabular dysplasia. Radiographic measures indicative of femoral coverage and acetabular geometry are most commonly used to evaluate dysplasia. A more thorough discussion of radiographic exams and abnormalities detected with volumetric imaging will be discussed in Section 1.3.

1.2.2 Treatment

If left untreated, acetabular dysplasia will lead to early joint degeneration and eventually result in end-stage hip OA^{50,68-70}. Conservative management of dysplasia includes avoiding high impact activities, strengthening the surrounding musculature to support the joint, and managing symptoms with anti-inflammatories and/or the use of a walking aid⁷¹. However, conservative management does not address the underlying bony pathology. Therefore, hip preserving surgeries have been popularized in recent decades to prevent or delay OA. The lack of femoral coverage is believed to reduce contact area

between the femoral head and acetabulum. Deficient coverage is believed to increase contact stress primarily along the lateral acetabulum^{72,73}. The presumed damage mechanism of overload to the lateral acetabulum corroborates with characteristic damage patterns observed clinically. Labral injuries, chondral lesions, and subchondral cysts are often reported in the lateral compartment of the acetabulum⁷⁴⁻⁷⁶.

Corrective pelvic osteotomies have become the accepted surgical treatment of acetabular dysplasia. In skeletally mature patients, periacetabular osteotomy (PAO) is the preferred hip preserving surgery. In PAO, the acetabulum is transected from the pelvis and reoriented into a position that increases femoral coverage^{77,78} (Fig. 1.3). A key difference in PAO compared to other pelvic osteotomies is that the posterior column of the pelvis remains intact, which maintains pelvic stability and allows earlier mobility following surgery^{60,79}. Additionally, the osteotomies are performed close to the joint, which minimizes disruption to the pelvic geometry, and allows for larger rotation acetabular corrections⁸⁰⁻⁸².

Repositioning of the acetabulum is the most critical aspect of the procedure. In most cases of classic acetabular dysplasia, the acetabulum is adducted and flexed to increase lateral and anterior coverage. The optimal position of the acetabulum has been refined over time. With long-term patient follow-up, the consequences of malpositioning the acetabulum have become apparent. For example, overcorrection of the acetabulum has been identified as a risk factor for developing impingement after PAO⁸³⁻⁸⁵. Parameters have been outlined to assist with positioning and encompass a few considerations^{60,72,86,87}. Correction of the center-edge angle (CEA), a measure of lateral femoral coverage, to 25-35° is one of the main factors in positioning the acetabulum.

Additional features that may prevent overcorrection and the development of impingement include positioning the acetabulum such that the sourcil (sclerotic, weight-bearing surface of the acetabulum) is not down-sloping, and ensuring that the center of the hip is not medialized to the point of iatrogenic protrusio⁶⁰.

Mid- to long-term follow-up of patients treated with PAO has demonstrated positive results in patients with minimal damage, and good joint congruency⁸⁸⁻⁹¹. Patients typically report pain relief and have higher outcome scores after recovery⁹². Recently, it has even been suggested that some patients can tolerate increased activity levels after PAO^{93,94}. However, degeneration does still occur in many patients. A study with 20 year follow-up reported that 40% of PAO patients had gone on to require total hip arthroplasty⁹⁰. Differences in biomechanics may provide insights into why some dysplastic hips continue to deteriorate despite being treated with PAO. Yet, clinical evaluations do not attempt to evaluate biomechanics. To date, computational modeling studies have attempted to clarify the mechanical effects of PAO with simulations. Models estimated increased contact area and reduced cartilage contact stress with PAO⁹⁵⁻⁹⁸. The clinical value of these studies are questionable, however, as simplifying assumptions were made for the geometric representation of cartilage.

PAO is technically complex and has a substantial learning curve⁹⁹⁻¹⁰². Complications are often related to surgeon inexperience, with complication rates varying from 11 to 45%, depending on the institution^{89,99-102}. Major complications include intra-articular extension of osteotomies and malpositioning of the acetabulum such that continued instability or impingement results^{101,102}. Refinements to the surgical technique, the recognition of the condition of hip impingement, and improvements in preoperative

imaging and surgical planning have decreased complications. However, integration of advanced surgical planning has yet to be a standard of care in patients treated with PAO. Furthermore, the mechanical efficacy of the PAO procedure for improving joint articulation and contact has yet to be reported.

1.3 Evaluation of Hip Joint Morphology

Abnormal hip morphology is what defines structural deformities of the hip. In the case of acetabular dysplasia, radiographic measures are most commonly used to stage the deformity. However, beyond an initial assessment to obtain a diagnosis, more advanced imaging can provide a 3D characterization of the deformity that may reveal subtle differences in acetabular dysplasia across patients.

1.3.1 Radiographic Measures

Radiographs generally confirm the suspicion of acetabular dysplasia. Initial imaging typically consists of a standing anteroposterior (AP) pelvis radiograph, lateral view, and a false profile view. The AP view is used to assess lateral coverage, slope of the acetabulum, and acetabular version. It is particularly important to obtain the AP radiograph with the pelvis in a position of neutral flexion and rotation, since measurements are sensitive to both^{103,104}. The lateral view assists in evaluating femoral head morphology, and the false profile view assesses anterior femoral coverage and joint congruency. The most common radiographic signs are described in more detail below.

The lateral center-edge angle (CEA) is a measure of lateral femoral coverage^{104,105}. It is obtained by drawing an axis through the center of the femoral head

and perpendicular to a medial-lateral line drawn between the ischial tuberosities. The angle at the center of the femoral head defined by the femoral axis line and a line that extends from the center of the femoral head to the lateral edge of the acetabular sourcil (weight-bearing surface of the acetabulum) is the lateral CEA^{106,107}. A lateral CEA less than 20° is indicative of dysplasia, though mild cases between 20-25° may be treated surgically if symptomatic¹⁰⁸.

Acetabular index/inclination (AI), or Tönnis angle, is a measure of the orientation of the sourcil originating from the most medial point of the sourcil¹⁰⁹. The AI is the angle measured between a horizontal line and a line extending from the most medial point of the sourcil to the most lateral point of the sourcil. An AI greater than 10° is considered an up-sloping sourcil and is indicative of dysplasia^{104,106,109}.

The version of the acetabulum can be estimated with an AP pelvis radiograph based on the presence of the crossover or figure-eight sign. The acetabulum is considered anteverted if the line of the anterior aspect of the rim does not cross the line of the posterior aspect of the rim before reaching the lateral edge of the sourcil. Conversely, in a retroverted acetabulum, the lines do cross. The presence of a crossover sign can be indicative of anterior overcoverage of the acetabulum, and/or posterior undercoverage of the acetabulum^{104,110}. The crossover sign is particularly sensitive to the positioning of the patient during radiography; misrepresentations can be introduced by excessive tilt or rotation of the pelvis¹⁰³.

The lateral view radiograph is used to assess femoral head and neck shape. Many patients with dysplasia exhibit insufficient femoral head-neck offset, which is a finding of impingement^{60,74}. Additionally, the sphericity of the femoral head is assessed using the

lateral view as dysplasia can be associated with a flattened femoral head^{60,104,111}. Finally, the false profile is important for evaluating anterior coverage of the femoral head and joint congruency^{91,104}. The anterior CEA, or angle of Lequesne, is similar to the lateral CEA, and measures anterior femoral coverage. The anterior CEA is measured from the center of the femoral head. The angle is defined between the vertical line that passes through the femoral head and a line that extends to the anterior edge of the acetabulum; values less than 25° occur with dysplasia^{104,106}. Joint congruency can also be qualitatively assessed on the false profile and AP view to ensure acetabular reorientation will not disrupt congruency^{91,104}.

While radiographs do provide useful metrics in describing acetabular morphology, there are limitations due to their two-dimensional (2D) nature. The complex surface of the acetabulum and the relationship between the femur and acetabulum should be fully analyzed in three dimensions (3D). Radiographic measures also have limited reliability due to inconsistent quality of films, differences in patient positioning, and irreproducible measurements^{112,113}.

1.3.2 Three-dimensional Characterization

Beyond the major difference in femoral coverage that defines acetabular dysplasia, other more subtle features including congruency and cartilage thickness have been described^{91,104,114}. While previously limited to 2D descriptions, volumetric imaging with computed tomography (CT) and magnetic resonance imaging (MRI) has made it possible to quantitatively characterize morphology in 3D. Considering that the diagnosis of acetabular dysplasia is based on reduced femoral coverage and that surgical treatment

is designed to increase femoral coverage, quantifying 3D coverage is clinically relevant. Klaue et al. were the first to demonstrate the potential of generating surfaces from CT, calculate femoral coverage in dysplastic hips, and simulate surgical reorientations to determine changes in coverage with varying degrees of acetabular reorientation^{115,116}. Using a projection technique, they quantified percent femoral head coverage in normal and dysplastic hips. Hips affected with dysplasia demonstrated reduced coverage, primarily in the anterolateral and posterolateral regions¹¹⁵. Dandachli et al. used a similar method but also ensured that pelvic tilt was adjusted to neutral; the main limitation with their method was that the femoral head was assumed spherical. Similar to prior estimates, dysplastic hips had significantly reduced coverage compared to normal (51% cover compared to 73% in normal hips)¹¹⁷. However, Stubbs et al. determined that 3D femoral coverage had no correlation with standard 2D radiographic measures¹¹⁴. The only study that has calculated 3D femoral coverage of dysplastic hips before and after PAO demonstrated a significant increase in coverage by an average of 49%, which restored overall percent coverage to a normal range. Mechlenburg et al. noted, however, that the posterolateral femoral head remained less covered than normal⁷⁸. Additionally, reduced posterolateral coverage after PAO has been corroborated with a study that measured CEA throughout coronal slices of a CT scan⁸¹. Subtle differences in coverage such as diminished posterolateral coverage cannot be appreciated with radiographs alone. Therefore, 3D assessments of coverage could aid in surgical planning of PAO to restore normal coverage overall.

The link between increased coverage and increased area in which to support load is intuitive. However, it is unlikely that the relationship between coverage and cartilage

contact is one-to-one. Altered congruency and differences in cartilage thickness could result in regions of focal loading, thereby reducing load-bearing area. The only study to report on quantitative differences in congruency between dysplastic and normal hips determined that dysplastic hips were significantly less congruent in unloaded regions¹. It has also been reported that dysplastic hips have significantly thicker cartilage compared to normal hips, and that the gradient increase in cartilage thickness towards the superolateral region was significantly greater in dysplastic hips⁹. These differences in congruency and cartilage thickness in dysplastic hips are important to consider in surgical planning. Reorientation of the acetabulum into a position that disrupts congruency or positions thinned cartilage into a loadbearing position could have serious mechanical consequences.

Differences in morphology may be important and useful predictors of the development of hip OA. A relationship between reduced femoral coverage defined by lateral CEA and hip OA has been described⁶⁸. With refined 3D measures of femoral coverage, in conjunction with a description of congruency and cartilage thickness, a more complete understanding of factors that contribute to the progression of OA may be elucidated. 3D metrics could also be useful in surgical planning; acetabular reorientations based on optimization routines that consider femoral coverage in all regions of the femoral head, congruency, and cartilage thickness of potential load-bearing surfaces could improve outcomes of PAO.

1.4 Hip Joint Mechanics

Altered kinematics, kinetics, and stresses to cartilage and labrum are believed to be the primary initiator of hip OA^{40,118-122}. Therefore, it is of primary importance to study these hip biomechanics in healthy and pathologic hips to better understand disease progression and evaluate surgical treatments that seek to restore normal mechanics. To this end, the work herein focuses on changes in intra-articular mechanics in hips with acetabular dysplasia after PAO. However, it is important to mention that differences in whole-joint mechanics likely contribute to the progression of damage in complex pathomechanical diseases of the hip such as acetabular dysplasia. Previous studies have reported altered joint angles and moments in patients with dysplasia⁶²⁻⁶⁴. Specifically for walking, patients with dysplasia were found to have significantly increased pelvic drop and rotation, reduced peak hip extension angle, and a lower walking velocity than the matched normal controls⁶²⁻⁶⁴.

These altered gait patterns likely result from a combination of factors including differences in surrounding soft tissue and musculature, decreased joint stability, and pain avoidance strategies. While some progress has been made in identifying differences in whole-joint mechanics, more research is needed to establish relationships between structural deformities and kinematics. Additional research in this regard will assist in refining the current methods for determining intra-articular mechanics.

1.4.1 Direct Measurement of Intra-articular Contact Mechanics

Intra-articular mechanics can be studied by invasive direct measurement techniques or with computational modeling. Briefly, directly measuring joint mechanics

can be accomplished in vitro by positioning pressure-sensitive film or electronic pressure sensors between the articulating surfaces¹²³⁻¹²⁸. The joint is positioned and loaded with fixtures to best replicate physiologic loading, and contact pressure is measured. Measurements are limited to levels that can be quantified by the pressure films, and by the force capacity and spatial resolution of electronic pressure sensors. Furthermore, the extensive dissection required to place sensors in the joint along with the addition of a foreign body into the joint space disrupts anatomic physiology and loading. To achieve in vivo loading conditions, a few studies have implanted instrumented hip prostheses that measure equivalent joint reaction forces^{2,129-132}. Although physiologic in respect to loading and soft tissue support, the idealized spherical geometry and metallic material of the implant are not representative of the native hip. Given the inherent limitations and invasive nature of direct measurement, computational modeling is an excellent alternative to estimate intra-articular mechanics.

1.4.2 Computational Modeling Techniques

Computational modeling can estimate cartilage contact stresses, strains, and areas in vivo. There are many computational models that approximate solutions to systems of equations that do not have exact solutions including finite element analysis (FEA), discrete element analysis (DEA), and multiscale modeling. Use of these techniques varies depending on the application. FEA uses basis functions with compact support to discretize a continuum into finite elements. FEA can predict stress and strain at all points throughout the continuum, providing detailed information from simulations within the continuum. In contrast, DEA represents deformable structures with discrete elements

such as springs and dashpots and estimates stress and strain at the contact surface¹³³⁻¹³⁸. DEA is computationally efficient, making it more accessible to large population studies and clinical applications¹³⁹⁻¹⁴². Multiscale modeling couples across scales, modeling stress and strain from the macroscale to microscale. Intra-articular mechanics can be studied at multiple levels, varying from macroscale whole joint cartilage mechanics down to the microscale chondrocyte level¹⁴³⁻¹⁴⁶. Although additional information can be obtained from multiscale modeling, the added complexity of interfacing between different tissue levels further complicates the modeling process, which limits the practicality of multiscale modeling as a tool with direct clinical relevance. As this dissertation is motivated by the need to extend computational modeling closer to clinical applications, the two methods that are explored henceforth are FEA and DEA.

1.4.3 Finite Element Analysis (FEA) in the Hip

Finite element analysis (FEA) is a well-accepted and well-described method for predicting mechanics throughout a continuum. The FE method is a weighted residual method that uses compactly supported basis functions to solve a set of governing partial differential equations¹⁴⁷. Our lab has an extensive history with the development, validation, and application of subject-specific FEA in the normal and pathologic hip^{1,23,125,127,147-150}. The following section elaborates on the aspects most relevant to evaluate changes in cartilage and labral mechanics in dysplastic hips from PAO.

Anderson et al. introduced the validated subject-specific FE model of the hip that serves as the basis for the FE study presented in Chapter 3. First published in 2005, few research groups have rivaled the caliber of Anderson's validated model to the present

day¹²⁵. FE studies of the hip typically make simplifying geometrical assumptions, most commonly by modeling the hip as a sphere^{98,151,152}, assuming constant cartilage thickness, or a combination of idealized geometry with cartilage thickness that varies along a single gradient direction. Models presented within these studies have not been experimentally validated, and produce unrealistic predictions of intra-articular mechanics, estimating unicentric contact patterns with predictions of contact stress that are often an order of magnitude lower than those measured in vitro^{123,124,126}. Spherical models of the hip continue to be published, despite their gross underestimation of cartilage contact stress and overestimation of contact area in unrealistic, concentric patterns^{148,153}. Challenges with acquiring volumetric images, generating subject-specific surface reconstructions, and discretizing surfaces into meshes that accurately capture complex and irregular geometries likely explain the limited number of studies that have modeled the hip using subject-specific geometry.

Since the initial validation of the FE modeling protocol by Anderson et al., a more extensive validation was completed and additional studies have defined cartilage mechanics in healthy hips, hips with acetabular retroversion, and hips with acetabular dysplasia^{1,23,127,149,150}. Cartilage contact stress and contact area in FE models of five cadaver hips with normal morphology predicted mechanics in good agreement with experimental measures using pressure film¹²⁷. Further, a parameter analysis indicated that contact stress is relatively insensitive to the constitutive model chosen for cartilage, and that specimen-specific material coefficients with regional variations did not have a large effect on contact mechanics¹²⁷. The minimal effects of cartilage representation on contact patterns support the use of the simplest hyperelastic model, a neo-Hookean

constitutive material, which reduces the computational complexity. Contact patterns quantified in the validation study also supported findings by Harris et al. when applied to living subjects with normal anatomy: specifically, that more variation in contact patterns exists between individuals than between simulated loading activities^{127,149}.

Subject-specific FE modeling studies that compared mechanics in patients with retroverted and dysplastic hips to those of healthy controls described minimal and inconsistent differences in cartilage contact mechanics between populations^{1,150}. However, in hips with acetabular dysplasia, the labrum carried a significantly larger amount of load compared to healthy hips. In hips with normal morphology, the labrum was estimated to support less than 3% of the total load transferred across the joint^{1,23}. In contrast, the labrum in dysplastic hips was loaded 2.8 to 4.0 times more than that of healthy hips¹. The additional load to the labrum of the dysplastic hip likely compensates for reduced bony support, which may explain why cartilage contact stress was not significantly larger in dysplastic hips compared to healthy hips. Russell et al. had conflicting results, and reported significantly elevated peak pressures in dysplastic hips¹⁵⁴. However, this model did not include the labrum, which would reconcile the discrepancy between the work done by Russell to that by Henak. Without labral support, it is possible that the shallow acetabulum is focally loaded along the lateral rim, creating a small localized region of elevated contact stress, as suggested by the simulations of Russell and colleagues¹⁵⁴.

The high incidence of OA in hips with dysplasia and the presence of damage patterns consistent with chronic overload of the lateral acetabulum have motivated the development of surgical treatments for acetabular dysplasia. Hip preserving surgeries

such as PAO are commonly performed to restore more normal coverage, and correspondingly, improve mechanics^{72,79,86}. Positive mid- to long-term outcomes in clinical studies have been cited to demonstrate the effectiveness of PAO for treating dysplasia based on radiographic measures and outcome scores⁸⁸⁻⁹⁰. However, while the underlying theory for PAO is based on improving mechanics, few studies have assessed changes in mechanics after PAO^{95,155}. Following PAO, the reorientation of the acetabulum may disrupt the natural congruency of the joint, which could have undesirable consequences. Furthermore, hip contact mechanics are unique to the individual and complex, and consequently may not behave similar to intuitive theories primarily based on joint coverage. Our validated FE modeling protocol that includes patient-specific bone, cartilage, and labrum offers a unique opportunity to elucidate hip contact mechanics following PAO.

1.4.4 Discrete Element Analysis (DEA) in the Hip

Discrete element analysis (DEA) was developed to determine human articular joint contact pressure following the concept of the Rigid Body Spring Model Theory that was derived by Kawai for civil engineering applications^{134,136}. It was termed DEA from its use of discrete spring elements to simulate rigid bodies in contact under static load¹⁵⁶. First introduced to orthopaedics as a 2D study to compare cartilage contact area and stress in normal and pathologic hips, DEA was quickly applied to other diarthrodial joints^{134,156-160}. A handful of DEA studies on the hip have been published^{95,97,161}. However, all hip DEA studies predicted concentric and symmetric contact distributions and introduced simplifying assumptions for cartilage geometry. Therefore, predictions of

prior DEA models of the hip were limited in their ability to extract physiologically realistic data. Nevertheless, it is possible that DEA models of the hip could predict accurate results if the actual geometry of bone and cartilage was included. This motivated the development of a subject-specific DEA model of the hip for the work herein. To introduce this modeling technique, the general theory and formulation of the DEA method is reviewed.

For orthopaedic applications, bones are modeled as rigid bodies, and articular cartilage is represented by an array of compressive springs^{134,135,140,161}. The rigid bodies representing bone are considered to be at equilibrium under the application of a joint reaction force. A solution is determined such that the sum of the spring reaction forces created from displacement of the rigid bone segments balances the applied joint reaction force. A linear spring model is typically used and will be discussed further; however, nonlinear representations have been described and may be found in the literature^{133,135,138}. Spring stiffness is derived from a linearized elasticity model, which assumes infinitesimal strains and a linear relationship between stress and strain. Starting with the equation for Hooke's law:

$$\sigma_{ij} = C_{ijkl}\epsilon_{kl} \quad (1.1)$$

Here, σ_{ij} is the Cauchy stress tensor, C_{ijkl} is the stiffness tensor, and ϵ_{kl} is the strain tensor. In this case, the stiffness tensor represents the spring stiffness, which is a scalar, κ . We also assume spring deformation is along the longitudinal direction of the spring, which simplifies the equation above to a first order equation:

$$\sigma_i = \kappa \epsilon_i \quad (1.2)$$

Next, κ can be expressed in terms of Young's modulus, E , and Poisson's ratio, ν , as follows:

$$\sigma_i = \frac{E(1-\nu)}{(1-2\nu)(1+\nu)} \epsilon_i \quad (1.3)$$

Stress and strain tensors are redefined based on definitions, $\sigma_i = \frac{f_i}{A}$ and $\epsilon_i = \frac{\Delta u_i}{h}$, where stress is the force over area for each spring element and strain is the displacement divided by initial spring length. Substituting into Eq. (1.3) we get the following:

$$\frac{f_i}{A} = \frac{E(1-\nu)}{(1-2\nu)(1+\nu)} \frac{\Delta u_i}{h} \quad (1.4)$$

Rearranging into the familiar format of Hooke's law, $F = k\Delta u$, where F is the force, k is the stiffness, and Δu is the displacement:

$$f_i = \frac{AE(1-\nu)}{h(1-2\nu)(1+\nu)} \Delta u_i \quad (1.5)$$

With further rearrangement of Eq. (1.5), the spring stiffness, k , can be defined as:

$$k = \frac{AE(1-\nu)}{h(1-2\nu)(1+\nu)} \quad (1.6)$$

The spring stiffness depends on the area of each element face associated with a spring, the spring length which corresponds to cartilage thickness, Young's modulus, and Poisson's ratio.

The DEA solver based on the theory and equations outlined above was created at the University of Utah Musculoskeletal Research Lab by Steve Maas and was specifically designed to complement the validated finite element model of the hip developed by Anderson et al¹²⁵. Therefore, the inputs required and model set up are similar to the finite element models described in Section 1.4.3. Briefly, the femur and pelvis are represented by triangulated rigid surfaces with cartilage thicknesses defined at each node. Bones are oriented according to loading conditions from in-vivo studies, which also define the magnitude and direction of the joint reaction force applied to the femur². A compressive spring is generated at the center of each triangular face on the femur and spring stiffness is determined from Eq. (1.6) using material properties from the literature¹⁶¹⁻¹⁶⁴. Newton's method is used to determine the solution by iteratively displacing the femur until the residual of the joint reaction force and sum of all spring forces is less than the user defined tolerance. Contact stresses are calculated from the spring force and triangular element area where each spring was attached.

Prior DEA studies of the hip are limited in their predictive abilities due to the geometrical assumptions made in their models. Yoshida et al. used a general 3D pelvic model and prescribed constant cartilage thickness to estimate hip mechanics during activities of daily life¹⁶¹. A study by Tsumura et al. simulated pelvic osteotomies in

dysplastic hips and predicted cartilage contact stress and area for every 5 degrees of acetabular rotation⁹⁷. Cartilage thickness was assumed to be equivalent to joint space thickness, or the distance between femur and acetabulum. Armiger et al. modeled dysplastic hips before and after PAO with DEA, assuming constant cartilage thickness⁹⁵. All of these studies predicted concentric and symmetric contact distributions as a result of simplifications to the representation of cartilage thickness. With model inputs that do not resemble the native hip, conclusions from prior DEA hip studies should be interpreted with caution.

The University of Utah DEA implementation for calculating intra-articular mechanics of the hip is based off of previously described DEA studies of the hip but enhances the geometrical representation of cartilage^{95,97,155,161,163}. Our DEA method distinguishes itself by including subject-specific bone and cartilage as model inputs, which introduces the dependence of spring stiffness on varying cartilage thickness values. Seemingly minor details, these changes have a dramatic influence on estimates of cartilage contact stress and area. Contact stress patterns change from unicentric, symmetric distributions of low magnitudes with constant cartilage thickness to bicentric patterns with higher magnitudes that concur with experimental studies when subject-specific cartilage thickness is included^{148,153}. Previously unable to predict accurate intra-articular mechanics in the hip due to modeling assumptions, DEA had limited applications. However, the University of Utah enhanced subject-specific DEA model of the hip offers opportunities for clinical and population-based studies.

1.5 Imaging the Hip Joint

Imaging is one of the primary diagnostic methods for assessing hip pain. Two-dimensional radiographs provide an initial evaluation and are typically relied on for preliminary diagnosis. However, once an underlying bony pathology has been identified, advanced imaging is often performed to comprehensively assess the joint. CT and MRI are commonly prescribed to evaluate bony abnormalities with greater detail in 3D, and as a means to detect articular and labral damage.

The hip joint is inherently challenging to image, which may explain why imaging studies of the hip are not as prevalent. The spherical shape of the femoral head and acetabulum make it susceptible to staircase artifact and partial volume averaging. Furthermore, articular cartilage in the hip is thin, requiring high-resolution scans to capture articular geometry. Additionally, the hip joint is tight, making it difficult to delineate opposing cartilage layers without traction and/or introduction of secondary fluid into the joint space. Finally, because of its deep position in the body, it is difficult to obtain sufficient signal-to-noise-ratio with MRI when imaging a joint obscured by soft tissue. Despite imaging challenges, CT and MRI are routinely used in the diagnosis, treatment management, and follow-up care of patients with hip pain.

1.5.1 Computed Tomography (CT) Imaging

CT images are produced by rotating an x-ray source around the body. X-rays pass through the body at different angles and a detector array collects the transmission projection data^{165,166}. Computer software then synthesizes the data to produce

tomographic images. Images can be reformatted into any plane, resulting in a stack of x-ray images through the plane that best appreciates the pathology.

CT is often utilized for preoperative planning for acetabular dysplasia. Clinicians may request CTs as standard of care to fully appreciate the extent of bony pathology for surgical planning. In contrast to 2D radiographs, CT images provide a more comprehensive, 3D assessment which may reveal subtle pathologies not visualized with radiographs^{106,114,167}. Additionally, 3D surface reconstructions can be generated from CT, enabling surgeons to interact with 3D models to assist with preoperative planning¹⁶⁷. While CT scans offer high-resolution imaging of bone, they cannot directly image the soft tissue structures of the hip joint. Assessing cartilage integrity is essential for hip preserving surgeries as preexisting cartilage damage has been associated with poor outcomes^{168,169}.

CT arthrography (CTA) is utilized to visualize bone and indirectly image hyaline cartilage, and labrum in the hip simultaneously. Using fluoroscopic guidance, a radiologist injects radio-opaque contrast material intra-articularly. The contrast material attenuates at a high intensity, similar to that of cortical bone for concentrations used for hip CTA^{170,171}. Articular cartilage and labrum are outlined by contrast and underlying subchondral bone (Fig. 1.4). Using CTA, cartilage degeneration and lesions as well as labral injuries can be imaged by visualizing penetration of contrast into soft tissue structures¹⁷²⁻¹⁷⁵ (Fig. 1.4).

Qualitative clinical evaluation using CT and CTA provides clinicians with useful information in determining treatment strategies. However, CT also enables quantitative analyses for research applications. Surface reconstructions serve as inputs into FE and

DEA models for prediction of intra-articular mechanics^{95,125,176}. 3D surfaces also enable the determination of kinematics with submillimeter accuracy¹⁷⁷. Additionally, 3D measures are more accurate than corresponding 2D radiographic measures used for clinical assessment^{110,114} and plots of cartilage thickness can be generated^{8,9,167,175}.

Although CT offers benefits for clinical and research applications, it is not without risk to the subject— infection, allergic reaction to administered contrast, and injury to neurovascular structures^{178,179}. However, the primary concern with CT for evaluating hip disorders is the associated exposure to ionizing radiation. MRI is often utilized to alleviate radiation concerns, especially considering that the patient population with hip dysplasia is young and may be at higher risk for long-term complications from increased radiation exposure.

1.5.2 Magnetic Resonance Imaging (MRI)

Magnetic resonance imaging (MRI) utilizes the properties of nuclear magnetic resonance to create high spatial resolution images with excellent soft tissue contrast. Generally, most imaging is based on the nucleus of the hydrogen atom, which is abundant in biological tissues. To obtain medical images, a patient is placed in the magnetic field, which aligns the protons parallel to the applied field. To generate a signal, the magnetization must be tipped away from equilibrium. Radiofrequency (RF) pulses disturb the protons so that the net magnetization vector flips out of alignment with the external magnetic field. The direction of the magnetization vector produces components transverse and longitudinal to the applied field. The precession of the transverse magnetization induces a current in a receiver coil, which becomes the MR signal.

After RF pulses, the net magnetization vector realigns with the axis of the applied field. The longitudinal magnetization recovers as spinning nuclei release energy back to the surrounding lattice through the process of T1 recovery. The time it takes for longitudinal recovery to the lowest energy state is called T1, or spin-lattice relaxation time. Concurrently, the transverse magnetization decreases and dephases due to interactions between adjacent spinning nuclei and their magnetic fields, termed T2 relaxation. T2 relaxation is inherent to the tissue, and depends on spin-spin interactions. Spin dephasing also occurs due to inhomogeneities in the magnetic field. The combination of spin-spin interactions and inhomogeneities in the magnetic field dephase transverse magnetization, resulting in T2* decay. T1, T2, and T2* values are tissue-specific and therefore, largely define tissue appearance. Tissue contrast is created from differences in T1, T2, and proton density, which are determined from inherent properties of the tissue¹⁸⁰. However, scanning parameters such as repetition time (TR) and echo time (TE) can be altered to emphasize specific types of contrast. TR is the time between RF pulses and TE is the time between an RF pulse and the peak of the detected signal^{181,182}. In general, T1-weighted images (short TR and TE) can depict anatomy best and T2-weighted images (long TR and TE) identify disease better because T2-weighted images highlight regions of higher water content, which typically is indicative of pathologic processes^{180,182,183}. Proton density weighted (PD) images (long TR and short TE) display differences in contrast predominantly due to differences in proton density between tissue types. PD sequences can usually visualize both anatomy and the disease process. Finally, signal localization is used to define positional data of the MR imaging system. Gradients of the strength of the magnetic field are applied in the imaging

plane¹⁸⁴. Both the phase-encoding and frequency-encoding gradients cause shifts in phase and frequency, respectively, which allows the exact location and amplitude of the signal to be computed.

There are many sequences used in MR imaging defined by additional parameters; however, the two fundamental types of pulse sequences are spin-echo (SE) and gradient echo (GRE). In SE sequences, a 90° RF pulse is applied, followed by a 180° pulse at one half the TE time to rephase the nuclei and induce an echo¹⁸⁵. To reduce scan time, fast spin-echo (FSE) sequences apply multiple 180° rephasing pulses¹⁸⁶. Each rephasing pulse creates an echo, which considered together are referred to as an echo train with a length equivalent to the number of RF rephasing pulses. FSE sequences are much faster than SE, and acquisition time is inversely related to the echo train length. GRE sequences differ from SE in that gradients, instead of RF pulses, are applied to dephase (negative gradients) and rephase (positive gradients) transverse magnetization¹⁸⁷. Additionally, variable flip angles are used with GRE. Because gradients do not refocus magnetic field inhomogeneities, GRE sequences are sensitive to inhomogeneity of the field, which can result in signal loss or susceptibility artifacts¹⁸⁸. Acquisition times are shorter for GRE compared to SE, and GRE sequences can involve the creation of a steady state¹⁸⁸. To create a steady state, a low angle RF pulse and a TR shorter than the T1 and T2 of the tissues are used. As a result, the net magnetization is not diminished between successive TRs, and the signal remains in a steady state. Therefore, transverse magnetization remains available for sampling¹⁸⁹. Spoiled or incoherent GRE sequences produce the same effect as T1 or PD-weighting with a spoiler RF gradient to eradicate the remaining transverse magnetization after each echo¹⁹⁰. Conversely, partially refocused or

coherent GRE sequences produce T2 weighting by applying a gradient to rephase the T2* magnetization while it is being dephased^{191,192}.

This section discusses the sequences most commonly used in imaging the hip: 2-D FSE, 3D spoiled gradient echo (SPGR), and 3D DESS. FSE sequences are widely used to image the hip clinically. The most common clinical MRI protocol uses a combination of T1-, T2-, and PD-weighted FSE acquisitions at a few locations throughout the joint and in different planes. These protocols provide 2D images at discrete locations in the joint, which is often described as a comprehensive assessment. In reality, images are limited to 2D snapshots in different planes and positions of the joint. This can give a general impression of joint health but could miss focal lesions and does not allow for comprehensive analyses using surface reconstruction for visualization or quantitative methods. Nonetheless, for the purpose of diagnosis, FSE sequences may be sufficient to obtain an overall impression of joint health. Specifically, the ability of MR imaging to identify chondral and labral pathologies has received a great deal of attention. Numerous studies have reported on the diagnostic accuracy and reliability of identifying labral tears; however, no census has been reached on the best technique. Historically, two-dimensional FSE sequences with intra-articular injection were popularized in detecting articular and labral damage, reporting the best accuracy^{174,193-198}. More recently, 3D acquisitions have been introduced to image the hip, providing volumetric images with equivalent or improved ability in detecting intra-articular damage^{9,194,195,198-202}.

In recent years, 3D MR imaging of the hip has become more common. However, generally speaking, studies to date have solely focused on the assessment of articular

damage and rely on low scan resolutions^{199-201,203}. Only a handful of studies have exploited the potential of 3D MR acquisitions; for example, to generate fringe plots of cartilage thickness^{9,173} and display site-specific integrity of cartilage using biochemical imaging²⁰⁰. 3D spoiled GRE (3D SPGR) is considered a standard MR technique for quantitative morphologic assessments of cartilage in the knee and presents the advantages of high spatial resolution and high signal intensity of articular cartilage²⁰⁴⁻²⁰⁷. Therefore, it is no surprise that of the few studies that have used 3D MRI to image the hip, SPGR has been the most common 3D sequence employed. In SPGR, a spoiler RF gradient is used to eradicate any remaining transverse magnetization after each echo, thereby producing the same effect as T1 or proton-density weighting¹⁹⁰. Very few studies have imaged the hip in 3D with MRI as it is challenging to obtain high-resolution images with sufficient signal and contrast. 3D SPGR sequences have been used to compare morphology and articular damage between healthy hips and hips affected with acetabular dysplasia^{9,173,208,209}. Although images captured morphology and identified intra-articular damage reasonably well, SPGR may not be the ideal sequence for the hip because of disadvantages including lack of contrast between cartilage and fluid, longer imaging times, and high sensitivity to susceptibility artifacts²¹⁰.

3D dual echo steady-state (DESS) is a well-established sequence for morphologic assessment of knee cartilage that could be applicable to imaging the hip²¹¹⁻²¹⁴. DESS is more time efficient and has higher signal-to-noise ratio and cartilage-to-fluid contrast than SPGR^{215,216}. DESS is a 3D coherent GRE sequence that acquires two or more gradient echoes separated with a RF pulse and combines both echoes to produce images²¹⁷. DESS images have a larger T2* weighting, which creates high signal in

cartilage and synovial fluid. Extensive evaluation of DESS in knee OA trials has demonstrated good accuracy and precision in diagnostic and quantitative cartilage assessments^{209,211}. Considering the benefits that DESS offers, it is a promising sequence to study the hip: high-resolution scans, enhanced contrast between cartilage and fluid, and efficient scan times. The most recent MR studies of the hip have used DESS for morphologic assessments and identification of chondral and labral injuries¹⁹⁸⁻²⁰⁰. However, no study has used DESS to generate surface reconstructions of the bone and soft tissue structures of the hip. Finally, the accuracy of DESS to image hip cartilage has not been evaluated.

1.6 Overall Motivation and Summary of Chapters

The over-arching goal of this dissertation is to improve the clinical diagnosis and treatment of acetabular dysplasia and evaluate the mechanical efficacy of the PAO procedure. Because dysplasia is believed to be a pathomechanical disease of the hip, clinical care should be based on mechanical analyses. The body of this dissertation seeks to develop the foundations for a biomechanical assessment of acetabular dysplasia. Specifically, this dissertation enhances the understanding of the widely accepted surgical treatment of PAO for dysplasia, introduces a clinically accessible computational model to estimate intra-articular hip contact mechanics, and improves advanced imaging for the hip joint that is necessary to generate accurate patient-specific models.

The focus of Chapters 2 and 3 is to evaluate morphology and biomechanics in acetabular dysplasia before and after surgical treatment of PAO. As described in Section 1.2.2, the rationale of PAO is that reorientation of the acetabulum improves coverage of

the femoral head, increases joint stability, and decreases joint contact stress. Although intuitive, the ability of PAO to normalize hip contact mechanics has yet to be demonstrated quantitatively in a cohort of patients treated for dysplasia. Also, to date, follow-up studies of PAO patients have only described subjective patient-reported outcomes (e.g. questionnaires) and changes in 2D radiographic measures⁸⁸⁻⁹⁰. Changes in the complex, 3D morphology have not been adequately described, and no study has quantified changes in intra-articular mechanics following PAO with patient-specific detail.

Chapter 2 reports measures of 2D and 3D morphology before and after PAO in patients with acetabular dysplasia. Chapter 3 details changes in cartilage and labrum contact mechanics before and after PAO, and relates biomechanical findings to articular congruency. Chapter 3 provides the first assessment of pre- and postoperative hip contact mechanics using patient-specific anatomy. As discussed previously, only models that employed idealized geometry for cartilage and bone have been used to study mechanics before and after PAO. Together, Chapters 2 and 3 provide a quantitative dataset that addresses clinically important questions related to the treatment of dysplastic hips. These data also provide baseline data required to develop optimization software and associated methods that could be useful for preoperative surgical planning.

Personalized surgical plans are becoming more common as the healthcare industry has access to improved technology. With its steep learning curve, surgeons who perform the PAO procedure could benefit from incorporating patient-specific surgical plans to guide the resection and reorientation of the acetabulum. Ideally, personalized plans would ensure the acetabulum is rotated into a position that minimizes contact

stresses. Computational methods such as FEA and DEA could be used for this purpose. Introduced in Section 1.4.4, DEA predicts hip contact mechanics by modeling cartilage as an array of deformable springs. Chapter 4 describes the first implementation of a subject-specific DEA model of the hip. As detailed in Chapter 4, DEA models of the hip can be analyzed in seconds, compared to several minutes or hours required by FEA. With excellent computational efficiency, DEA could become a valuable clinical tool. Potential applications may include a preoperative estimation of contact areas and cartilage stress distributions on a per-patient basis to determine disease severity, and potentially, the need for surgery. DEA could also be used to predict the optimal relocation of the acetabulum during PAO.

Discussed in Section 1.5, imaging is necessary for clinical diagnosis as well as for generating computational models. Specifically, volumetric image data are required to create accurate surface reconstructions and computational models that emulate subject-specific anatomy. For clinical diagnosis, 3D imaging of the hip is essential to visualize deformities throughout the hip. Surface reconstructions can then be used to appreciate the complex geometry of the pelvis and femur as well as the relationship between the two²¹⁸⁻²²¹. The success of the PAO procedure relies on a 3D preoperative assessment of the size and location of bony hip deformities as well as cartilage integrity/continuity (i.e. health, thickness)^{168,222}. In particular, the clinician must not rotate the acetabulum during PAO such that damaged areas of cartilage undergo continued loading in the postoperative configuration. Surprisingly, preoperative planning of PAO currently relies on 2D radiographs, which do not visualize cartilage and cannot describe the complex, 3D nature of hip anatomy.

Section 1.5.1 outlined CT, and described how our lab has utilized CT for the purpose of 3D modeling of the hip^{1,23,125,127,139,147-150,176,177,223,224}. Using CT, high-resolution images can be obtained of the entire pelvis and proximal femur in short scan times, typically 12 seconds^{225,226}. Coupled with intra-articular injection of radio-opaque contrast agents and traction, CT scans of the hip can clearly delineate cortical and trabecular bone, and femoral and acetabular cartilage^{8,119,135,163,202}. However, the major limitation of CT is the associated radiation exposure, which can exceed 10 mSv (1 Rad)²²⁶.

The number of patients diagnosed and treated for developmental hip disorders will continue to increase in the coming years, especially as we become more aware of conditions similar to dysplasia, such as femoroacetabular impingement and acetabular retroversion. Most patients with hip pathoanatomy are young, healthy adults (i.e. 18-40 y/o). Furthermore, nearly 75% of patients have bilateral hip pathologies, requiring follow-up care in the form of additional scans⁴⁹. Noninvasive techniques to image both hips over time are therefore advantageous. Accordingly, imaging methods that do not require radiation would be ideal for patients with hip dysplasia. Ideally, the chosen modality would image bone and cartilage in a single sequence, be of high resolution, obtain volumetric data, and be time-efficient. Introduced in Section 1.5.2, the use of certain MRI sequences could allow for volumetric imaging of hip bone and cartilage to provide clinicians with enhanced visualization of deformities and damage without the risk of ionizing radiation.

As described in Section 1.5.2, DESS MRI could be an excellent sequence to image the hip for diagnostic purposes as well as for 3D modeling. For example, imaging with

DESS could streamline the process to generate 3D reconstructions of bone and cartilage. Specifically, with DESS, bone, cartilage, and intra-articular contrast are represented by different voxel intensities; in CTA, bone and intra-articular contrast have very similar intensities (Fig 1.4). With similar x-ray attenuations, it can be tedious and time-consuming to manually segment bone from contrast using CTA in order to create 3D surface reconstructions. With separate voxel intensities, it may be feasible to automatically segment the DESS MR images, ultimately reducing the time needed to create 3D surfaces.

Chapter 5 reports on the implementation of the DESS MRI protocol to obtain high-resolution 3D acquisitions of the hip; the use of traction and intra-articular fluid to visualize opposing layers of cartilage are also described. Additionally, Chapter 5 demonstrates that DESS is potentially more accurate than CTA to measure acetabular cartilage thickness. With the accuracy of DESS for imaging hip cartilage thickness established, Chapter 5 provides a protocol that could be deployed for the purpose of staging OA on a per-patient basis, or longitudinally assess the efficacy of various treatments (conservative, medication, surgery, etc.) in terms of retarding the progression of OA.

Finally, Chapter 6 summarizes the conclusions of this dissertation as a body of work, and interprets key findings of each chapter as interrelated topics to improve clinical management of acetabular dysplasia. Additionally, Chapter 6 discusses future directions that may build upon the work herein.

1.7 References

1. Bergmann G, Deuretzbacher G, Heller M, et al. 2001. Hip contact forces and gait patterns from routine activities. *Journal of biomechanics* 34: 859-871.
2. Hashimoto N, Ando M, Yayama T, et al. 2005. Dynamic analysis of the resultant force acting on the hip joint during level walking. *Artificial organs* 29: 387-392.
3. Schwachmeyer V, Damm P, Bender A, et al. 2013. In vivo hip joint loading during post-operative physiotherapeutic exercises. *PloS one* 8: e77807.
4. Salaffi F, Carotti M, Stancati A, et al. 2005. Health-related quality of life in older adults with symptomatic hip and knee osteoarthritis: a comparison with matched healthy controls. *Aging clinical and experimental research* 17: 255-263.
5. Nho SJ, Kymes SM, Callaghan JJ, et al. 2013. The burden of hip osteoarthritis in the United States: epidemiologic and economic considerations. *The Journal of the American Academy of Orthopaedic Surgeons* 21 Suppl 1: S1-6.
6. Aronson J. 1986. Osteoarthritis of the young adult hip: etiology and treatment. *Instructional course lectures* 35: 119-128.
7. Allen BC, Peters CL, Brown NA, et al. 2010. Acetabular cartilage thickness: accuracy of three-dimensional reconstructions from multidetector CT arthrograms in a cadaver study. *Radiology* 255: 544-552.
8. Nishii T, Sugano N, Sato Y, et al. 2004. Three-dimensional distribution of acetabular cartilage thickness in patients with hip dysplasia: a fully automated computational analysis of MR imaging. *Osteoarthritis and cartilage / OARS, Osteoarthritis Research Society* 12: 650-657.
9. Shepherd DE, Seedhom BB. 1999. Thickness of human articular cartilage in joints of the lower limb. *Annals of the rheumatic diseases* 58: 27-34.
10. Buckwalter JA, Mankin HJ, Grodzinsky AJ. 2005. Articular cartilage and osteoarthritis. *Instructional course lectures* 54: 465-480.
11. Mow VC, Huiskes R. 2005. *Basic orthopaedic biomechanics & mechano-biology*: Lippincott Williams & Wilkins; p.
12. Cohen NP, Foster RJ, Mow VC. 1998. Composition and dynamics of articular cartilage: structure, function, and maintaining healthy state. *The Journal of orthopaedic and sports physical therapy* 28: 203-215.

13. Poole AR, Kojima T, Yasuda T, et al. 2001. Composition and structure of articular cartilage: a template for tissue repair. *Clinical orthopaedics and related research*: S26-33.
14. Sophia Fox AJ, Bedi A, Rodeo SA. 2009. The basic science of articular cartilage: structure, composition, and function. *Sports health* 1: 461-468.
15. Ateshian GA, Lai WM, Zhu WB, et al. 1994. An asymptotic solution for the contact of two biphasic cartilage layers. *Journal of biomechanics* 27: 1347-1360.
16. O'Hara BP, Urban JP, Maroudas A. 1990. Influence of cyclic loading on the nutrition of articular cartilage. *Annals of the rheumatic diseases* 49: 536-539.
17. Newman AP. 1998. Articular cartilage repair. *The American journal of sports medicine* 26: 309-324.
18. Keene GS, Villar RN. 1994. Arthroscopic anatomy of the hip: an in vivo study. *Arthroscopy : the journal of arthroscopic & related surgery : official publication of the Arthroscopy Association of North America and the International Arthroscopy Association* 10: 392-399.
19. Seldes RM, Tan V, Hunt J, et al. 2001. Anatomy, histologic features, and vascularity of the adult acetabular labrum. *Clinical orthopaedics and related research*: 232-240.
20. Won YY, Chung IH, Chung NS, et al. 2003. Morphological study on the acetabular labrum. *Yonsei medical journal* 44: 855-862.
21. Safran MR. 2010. The acetabular labrum: anatomic and functional characteristics and rationale for surgical intervention. *The Journal of the American Academy of Orthopaedic Surgeons* 18: 338-345.
22. Henak CR, Abraham CL, Anderson AE, et al. 2014. Patient-specific analysis of cartilage and labrum mechanics in human hips with acetabular dysplasia. *Osteoarthritis and cartilage / OARS, Osteoarthritis Research Society* 22: 210-217.
23. Henak CR, Ellis BJ, Harris MD, et al. 2011. Role of the acetabular labrum in load support across the hip joint. *Journal of biomechanics* 44: 2201-2206.
24. Konrath GA, Hamel AJ, Olson SA, et al. 1998. The role of the acetabular labrum and the transverse acetabular ligament in load transmission in the hip. *The Journal of bone and joint surgery American volume* 80: 1781-1788.
25. Tan V, Seldes RM, Katz MA, et al. 2001. Contribution of acetabular labrum to articulating surface area and femoral head coverage in adult hip joints: an anatomic study in cadavera. *American journal of orthopedics* 30: 809-812.

26. Petersen W, Petersen F, Tillmann B. 2003. Structure and vascularization of the acetabular labrum with regard to the pathogenesis and healing of labral lesions. *Archives of orthopaedic and trauma surgery* 123: 283-288.
27. Lawrence RC, Helmick CG, Arnett FC, et al. 1998. Estimates of the prevalence of arthritis and selected musculoskeletal disorders in the United States. *Arthritis and rheumatism* 41: 778-799.
28. Zhang Y, Xu L, Nevitt MC, et al. 2001. Comparison of the prevalence of knee osteoarthritis between the elderly Chinese population in Beijing and whites in the United States: The Beijing Osteoarthritis Study. *Arthritis and rheumatism* 44: 2065-2071.
29. Gupta KB, Duryea J, Weissman BN. 2004. Radiographic evaluation of osteoarthritis. *Radiologic clinics of North America* 42: 11-41, v.
30. Murphy L, Helmick CG. 2012. The impact of osteoarthritis in the United States: a population-health perspective. *The American journal of nursing* 112: S13-19.
31. Lane NE. 2007. Clinical practice. Osteoarthritis of the hip. *The New England journal of medicine* 357: 1413-1421.
32. Lieveense AM, Bierma-Zeinstra SM, Verhagen AP, et al. 2003. Influence of sporting activities on the development of osteoarthritis of the hip: a systematic review. *Arthritis and rheumatism* 49: 228-236.
33. Lieveense AM, Reijman M, Pols HA, et al. 2003. Obesity and hip osteoarthritis. *The American journal of medicine* 115: 329; author reply 329-330.
34. Ganz R, Leunig M, Leunig-Ganz K, et al. 2008. The etiology of osteoarthritis of the hip: an integrated mechanical concept. *Clinical orthopaedics and related research* 466: 264-272.
35. Jacobsen S, Sonne-Holm S. 2005. Hip dysplasia: a significant risk factor for the development of hip osteoarthritis. A cross-sectional survey. *Rheumatology* 44: 211-218.
36. Hochberg MC. 2012. Osteoarthritis year 2012 in review: clinical. *Osteoarthritis and cartilage / OARS, Osteoarthritis Research Society* 20: 1465-1469.
37. Mankin HJ. 1974. The reaction of articular cartilage to injury and osteoarthritis (second of two parts). *The New England journal of medicine* 291: 1335-1340.
38. Adataia A, Rainsford KD, Kean WF. 2012. Osteoarthritis of the knee and hip. Part I: aetiology and pathogenesis as a basis for pharmacotherapy. *The Journal of pharmacy and pharmacology* 64: 617-625.

39. Mankin HJ. 1974. The reaction of articular cartilage to injury and osteoarthritis (first of two parts). *The New England journal of medicine* 291: 1285-1292.
40. Setton LA, Elliott DM, Mow VC. 1999. Altered mechanics of cartilage with osteoarthritis: human osteoarthritis and an experimental model of joint degeneration. *Osteoarthritis and cartilage / OARS, Osteoarthritis Research Society* 7: 2-14.
41. Bennell KL, Egerton T, Martin J, et al. 2014. Effect of physical therapy on pain and function in patients with hip osteoarthritis: a randomized clinical trial. *JAMA : the journal of the American Medical Association* 311: 1987-1997.
42. Fransen M, McConnell S, Hernandez-Molina G, et al. 2014. Exercise for osteoarthritis of the hip. *The Cochrane database of systematic reviews* 4: CD007912.
43. Warsi A, LaValley MP, Wang PS, et al. 2003. Arthritis self-management education programs: a meta-analysis of the effect on pain and disability. *Arthritis and rheumatism* 48: 2207-2213.
44. Zhang W, Doherty M, Arden N, et al. 2005. EULAR evidence based recommendations for the management of hip osteoarthritis: report of a task force of the EULAR Standing Committee for International Clinical Studies Including Therapeutics (ESCSIT). *Annals of the rheumatic diseases* 64: 669-681.
45. Adatia A, Rainsford KD, Kean WF. 2012. Osteoarthritis of the knee and hip. Part II: therapy with ibuprofen and a review of clinical trials. *The Journal of pharmacy and pharmacology* 64: 626-636.
46. Verkleij SP, Luijsterburg PA, Bohnen AM, et al. 2011. NSAIDs vs acetaminophen in knee and hip osteoarthritis: a systematic review regarding heterogeneity influencing the outcomes. *Osteoarthritis and cartilage / OARS, Osteoarthritis Research Society* 19: 921-929.
47. Zamani O, Bottcher E, Rieger JD, et al. 2014. Comparison of safety, efficacy and tolerability of Dexibuprofen and Ibuprofen in the treatment of osteoarthritis of the hip or knee. *Wiener klinische Wochenschrift* 126: 368-375.
48. Levine ME, Nace J, Kapadia BH, et al. 2013. Treatment of primary hip osteoarthritis for the primary care physician and the indications for total hip arthroplasty. *Journal of long-term effects of medical implants* 23: 323-330.
49. Clohisy JC, Dobson MA, Robison JF, et al. 2011. Radiographic structural abnormalities associated with premature, natural hip-joint failure. *The Journal of bone and joint surgery American volume* 93 Suppl 2: 3-9.

50. Weinstein SL. 1987. Natural history of congenital hip dislocation (CDH) and hip dysplasia. *Clinical orthopaedics and related research*: 62-76.
51. Dezateux C, Rosendahl K. 2007. Developmental dysplasia of the hip. *Lancet* 369: 1541-1552.
52. Guille JT, Pizzutillo PD, MacEwen GD. 2000. Development dysplasia of the hip from birth to six months. *The Journal of the American Academy of Orthopaedic Surgeons* 8: 232-242.
53. Bittersohl B, Hosalkar HS, Wenger DR. 2012. Surgical treatment of hip dysplasia in children and adolescents. *The Orthopedic clinics of North America* 43: 301-315.
54. Lee CB, Mata-Fink A, Millis MB, et al. 2013. Demographic differences in adolescent-diagnosed and adult-diagnosed acetabular dysplasia compared with infantile developmental dysplasia of the hip. *Journal of pediatric orthopedics* 33: 107-111.
55. Engesaeter IO, Laborie LB, Lehmann TG, et al. 2013. Prevalence of radiographic findings associated with hip dysplasia in a population-based cohort of 2081 19-year-old Norwegians. *The bone & joint journal* 95-B: 279-285.
56. Jacobsen S, Sonne-Holm S, Soballe K, et al. 2005. Hip dysplasia and osteoarthritis: a survey of 4151 subjects from the Osteoarthritis Substudy of the Copenhagen City Heart Study. *Acta orthopaedica* 76: 149-158.
57. de Hundt M, Vlemmix F, Bais JM, et al. 2012. Risk factors for developmental dysplasia of the hip: a meta-analysis. *European journal of obstetrics, gynecology, and reproductive biology* 165: 8-17.
58. Loder RT, Skopelja EN. 2011. The epidemiology and demographics of hip dysplasia. *ISRN orthopedics* 2011: 238607.
59. Feldman GJ, Peters CL, Erickson JA, et al. 2012. Variable expression and incomplete penetrance of developmental dysplasia of the hip: clinical challenge in a 71-member multigeneration family. *The Journal of arthroplasty* 27: 527-532.
60. Tibor LM, Sink EL. 2012. Periacetabular osteotomy for hip preservation. *The Orthopedic clinics of North America* 43: 343-357.
61. MacDonald S, Garbuz D, Ganz R. 1997. Clinical evaluation of the symptomatic young adult hip. *Seminars in Arthroplasty*, 3-9.
62. Jacobsen JS, Nielsen DB, Sorensen H, et al. 2013. Changes in walking and running in patients with hip dysplasia. *Acta orthopaedica* 84: 265-270.

63. Pedersen EN, Simonsen EB, Alkjaer T, et al. 2004. Walking pattern in adults with congenital hip dysplasia: 14 women examined by inverse dynamics. *Acta orthopaedica Scandinavica* 75: 2-9.
64. Romano CL, Frigo C, Randelli G, et al. 1996. Analysis of the gait of adults who had residua of congenital dysplasia of the hip. *The Journal of bone and joint surgery American volume* 78: 1468-1479.
65. Hardcastle P, Nade S. 1985. The significance of the Trendelenburg test. *The Journal of bone and joint surgery British volume* 67: 741-746.
66. Nunley RM, Prather H, Hunt D, et al. 2011. Clinical presentation of symptomatic acetabular dysplasia in skeletally mature patients. *The Journal of bone and joint surgery American volume* 93 Suppl 2: 17-21.
67. Garbuz DS, Masri BA, Haddad F, et al. 2004. Clinical and radiographic assessment of the young adult with symptomatic hip dysplasia. *Clinical orthopaedics and related research*: 18-22.
68. Cooperman D. 2013. What is the evidence to support acetabular dysplasia as a cause of osteoarthritis? *Journal of pediatric orthopedics* 33 Suppl 1: S2-7.
69. Cooperman DR, Wallensten R, Stulberg SD. 1983. Acetabular dysplasia in the adult. *Clinical orthopaedics and related research*: 79-85.
70. Hartofilakidis G, Karachalios T, Stamos KG. 2000. Epidemiology, demographics, and natural history of congenital hip disease in adults. *Orthopedics* 23: 823-827.
71. Hunt D, Prather H, Harris Hayes M, et al. 2012. Clinical outcomes analysis of conservative and surgical treatment of patients with clinical indications of prearthritic, intra-articular hip disorders. *PM & R : the journal of injury, function, and rehabilitation* 4: 479-487.
72. Leunig M, Siebenrock KA, Ganz R. 2001. Rationale of periacetabular osteotomy and background work. *Instructional course lectures* 50: 229-238.
73. Trousdale RT. 2004. Acetabular osteotomy: indications and results. *Clinical orthopaedics and related research*: 182-187.
74. Domb BG, Lareau JM, Baydoun H, et al. 2014. Is intraarticular pathology common in patients with hip dysplasia undergoing periacetabular osteotomy? *Clinical orthopaedics and related research* 472: 674-680.
75. Kim KI, Cho YJ, Ramteke AA, et al. 2011. Peri-acetabular rotational osteotomy with concomitant hip arthroscopy for treatment of hip dysplasia. *The Journal of bone and joint surgery British volume* 93: 732-737.

76. Redmond JM, Gupta A, Stake CE, et al. 2014. The prevalence of hip labral and chondral lesions identified by method of detection during periacetabular osteotomy: arthroscopy versus arthrotomy. *Arthroscopy : the journal of arthroscopic & related surgery : official publication of the Arthroscopy Association of North America and the International Arthroscopy Association* 30: 382-388.
77. Imai H, Kamada T, Takeba J, et al. 2014. Anterior coverage after eccentric rotational acetabular osteotomy for the treatment of developmental dysplasia of the hip. *Journal of orthopaedic science : official journal of the Japanese Orthopaedic Association*.
78. Mechlenburg I, Nyengaard JR, Romer L, et al. 2004. Changes in load-bearing area after Ganz periacetabular osteotomy evaluated by multislice CT scanning and stereology. *Acta orthopaedica Scandinavica* 75: 147-153.
79. Ganz R, Klaue K, Vinh TS, et al. 1988. A new periacetabular osteotomy for the treatment of hip dysplasias. Technique and preliminary results. *Clinical orthopaedics and related research*: 26-36.
80. Clohisy JC, Schutz AL, St John L, et al. 2009. Periacetabular osteotomy: a systematic literature review. *Clinical orthopaedics and related research* 467: 2041-2052.
81. Haddad FS, Garbuz DS, Duncan CP, et al. 2000. CT evaluation of periacetabular osteotomies. *The Journal of bone and joint surgery British volume* 82: 526-531.
82. Trousdale RT, Cabanela ME, Berry DJ, et al. 2002. Magnetic resonance imaging pelvimetry before and after a periacetabular osteotomy. *The Journal of bone and joint surgery American volume* 84-A: 552-556.
83. Albers CE, Steppacher SD, Ganz R, et al. 2013. Impingement adversely affects 10-year survivorship after periacetabular osteotomy for DDH. *Clinical orthopaedics and related research* 471: 1602-1614.
84. Ziebarth K, Balakumar J, Domayer S, et al. 2011. Bernese periacetabular osteotomy in males: is there an increased risk of femoroacetabular impingement (FAI) after Bernese periacetabular osteotomy? *Clinical orthopaedics and related research* 469: 447-453.
85. Myers SR, Eijer H, Ganz R. 1999. Anterior femoroacetabular impingement after periacetabular osteotomy. *Clinical orthopaedics and related research*: 93-99.
86. Leunig M, Ganz R. 2014. The evolution and concepts of joint-preserving surgery of the hip. *The bone & joint journal* 96-B: 5-18.

87. Siebenrock KA, Leunig M, Ganz R. 2001. Periacetabular osteotomy: the Bernese experience. *Instructional course lectures* 50: 239-245.
88. Hartig-Andreasen C, Troelsen A, Thillemann TM, et al. 2012. What factors predict failure 4 to 12 years after periacetabular osteotomy? *Clinical orthopaedics and related research* 470: 2978-2987.
89. Matheney T, Kim YJ, Zurakowski D, et al. 2009. Intermediate to long-term results following the Bernese periacetabular osteotomy and predictors of clinical outcome. *The Journal of bone and joint surgery American volume* 91: 2113-2123.
90. Steppacher SD, Tannast M, Ganz R, et al. 2008. Mean 20-year followup of Bernese periacetabular osteotomy. *Clinical orthopaedics and related research* 466: 1633-1644.
91. Yasunaga Y, Yamasaki T, Ochi M. 2012. Patient selection criteria for periacetabular osteotomy or rotational acetabular osteotomy. *Clinical orthopaedics and related research* 470: 3342-3354.
92. Pogliacomi F, Stark A, Wallensten R. 2005. Periacetabular osteotomy. Good pain relief in symptomatic hip dysplasia, 32 patients followed for 4 years. *Acta orthopaedica* 76: 67-74.
93. Bogunovic L, Hunt D, Prather H, et al. 2014. Activity Tolerance After Periacetabular Osteotomy. *The American journal of sports medicine*.
94. Novais EN, Heyworth B, Murray K, et al. 2013. Physical activity level improves after periacetabular osteotomy for the treatment of symptomatic hip dysplasia. *Clinical orthopaedics and related research* 471: 981-988.
95. Armiger RS, Armand M, Tallroth K, et al. 2009. Three-dimensional mechanical evaluation of joint contact pressure in 12 periacetabular osteotomy patients with 10-year follow-up. *Acta orthopaedica* 80: 155-161.
96. Hipp JA, Sugano N, Millis MB, et al. 1999. Planning acetabular redirection osteotomies based on joint contact pressures. *Clinical orthopaedics and related research*: 134-143.
97. Tsumura H, Kaku N, Ikeda S, et al. 2005. A computer simulation of rotational acetabular osteotomy for dysplastic hip joint: does the optimal transposition of the acetabular fragment exist? *Journal of orthopaedic science : official journal of the Japanese Orthopaedic Association* 10: 145-151.
98. Zhao X, Chosa E, Totoribe K, et al. 2010. Effect of periacetabular osteotomy for acetabular dysplasia clarified by three-dimensional finite element analysis.

- Journal of orthopaedic science : official journal of the Japanese Orthopaedic Association 15: 632-640.
99. Clohisy JC, Barrett SE, Gordon JE, et al. 2005. Periacetabular osteotomy for the treatment of severe acetabular dysplasia. *The Journal of bone and joint surgery American volume* 87: 254-259.
 100. Crockarell J, Jr., Trousdale RT, Cabanela ME, et al. 1999. Early experience and results with the periacetabular osteotomy. The Mayo Clinic experience. *Clinical orthopaedics and related research*: 45-53.
 101. Hussell JG, Rodriguez JA, Ganz R. 1999. Technical complications of the Bernese periacetabular osteotomy. *Clinical orthopaedics and related research*: 81-92.
 102. Peters CL, Erickson JA, Hines JL. 2006. Early results of the Bernese periacetabular osteotomy: the learning curve at an academic medical center. *The Journal of bone and joint surgery American volume* 88: 1920-1926.
 103. Tannast M, Zheng G, Anderegg C, et al. 2005. Tilt and rotation correction of acetabular version on pelvic radiographs. *Clinical orthopaedics and related research* 438: 182-190.
 104. Clohisy JC, Carlisle JC, Beaulé PE, et al. 2008. A systematic approach to the plain radiographic evaluation of the young adult hip. *The Journal of bone and joint surgery American volume* 90 Suppl 4: 47-66.
 105. Wiberg G. 1953. Shelf operation in congenital dysplasia of the acetabulum and in subluxation and dislocation of the hip. *The Journal of bone and joint surgery American volume* 35-A: 65-80.
 106. Delaunay S, Dussault RG, Kaplan PA, et al. 1997. Radiographic measurements of dysplastic adult hips. *Skeletal radiology* 26: 75-81.
 107. Anderson LA, Gililand J, Pelt C, et al. 2011. Center edge angle measurement for hip preservation surgery: technique and caveats. *Orthopedics* 34: 86.
 108. Wiberg GGF, Helen D. 1939. *Studies on Dysplastic Acetabula and Congenital Subluxation of the Hip Joint, with special reference to the complication of Osteo-Arthritis.* (Translated from the Swedish by Helen Frey.); p.
 109. Tönnis D. 1976. Normal values of the hip joint for the evaluation of X-rays in children and adults. *Clinical orthopaedics and related research* 119: 39-47.
 110. Hansen BJ, Harris MD, Anderson LA, et al. 2012. Correlation between radiographic measures of acetabular morphology with 3D femoral head coverage in patients with acetabular retroversion. *Acta orthopaedica* 83: 233-239.

111. Okano K, Yamaguchi K, Ninomiya Y, et al. 2013. Femoral head deformity and severity of acetabular dysplasia of the hip. *The bone & joint journal* 95-B: 1192-1196.
112. Carlisle JC, Zebala LP, Shia DS, et al. 2011. Reliability of various observers in determining common radiographic parameters of adult hip structural anatomy. *The Iowa orthopaedic journal* 31: 52-58.
113. Clohisy JC, Carlisle JC, Trousdale R, et al. 2009. Radiographic evaluation of the hip has limited reliability. *Clinical orthopaedics and related research* 467: 666-675.
114. Stubbs AJ, Anz AW, Frino J, et al. 2011. Classic measures of hip dysplasia do not correlate with three-dimensional computer tomographic measures and indices. *Hip international : the journal of clinical and experimental research on hip pathology and therapy* 21: 549-558.
115. Klaue K, Wallin A, Ganz R. 1988. CT evaluation of coverage and congruency of the hip prior to osteotomy. *Clinical orthopaedics and related research*: 15-25.
116. Klaue K, Bresina S, Guéat P, et al. 1997. Morphological 3-dimensional assessment, pre-operative simulation and rationale of intra-operative navigation in orthopaedic surgery: Practical application for re-orienting osteotomies of the hip joint. *Injury* 28: 12-30.
117. Dandachli W, Kannan V, Richards R, et al. 2008. Analysis of cover of the femoral head in normal and dysplastic hips: new CT-based technique. *The Journal of bone and joint surgery British volume* 90: 1428-1434.
118. Buckwalter JA. 1995. Osteoarthritis and articular cartilage use, disuse, and abuse: experimental studies. *The Journal of rheumatology Supplement* 43: 13-15.
119. Hadley NA, Brown TD, Weinstein SL. 1990. The effects of contact pressure elevations and aseptic necrosis on the long-term outcome of congenital hip dislocation. *Journal of orthopaedic research : official publication of the Orthopaedic Research Society* 8: 504-513.
120. Loening AM, James IE, Levenston ME, et al. 2000. Injurious mechanical compression of bovine articular cartilage induces chondrocyte apoptosis. *Archives of biochemistry and biophysics* 381: 205-212.
121. Maxian TA, Brown TD, Weinstein SL. 1995. Chronic stress tolerance levels for human articular cartilage: two nonuniform contact models applied to long-term follow-up of CDH. *Journal of biomechanics* 28: 159-166.

122. Radin EL, Burr DB, Caterson B, et al. 1991. Mechanical determinants of osteoarthritis. *Seminars in arthritis and rheumatism* 21: 12-21.
123. Adams D, Swanson SA. 1985. Direct measurement of local pressures in the cadaveric human hip joint during simulated level walking. *Annals of the rheumatic diseases* 44: 658-666.
124. Afoke NY, Byers PD, Hutton WC. 1987. Contact pressures in the human hip joint. *The Journal of bone and joint surgery British volume* 69: 536-541.
125. Anderson AE, Peters CL, Tuttle BD, et al. 2005. Subject-specific finite element model of the pelvis: development, validation and sensitivity studies. *Journal of biomechanical engineering* 127: 364-373.
126. Brown TD, Shaw DT. 1983. In vitro contact stress distributions in the natural human hip. *Journal of biomechanics* 16: 373-384.
127. Henak CR, Kapron AL, Anderson AE, et al. 2014. Specimen-specific predictions of contact stress under physiological loading in the human hip: validation and sensitivity studies. *Biomechanics and modeling in mechanobiology* 13: 387-400.
128. von Eisenhart R, Adam C, Steinlechner M, et al. 1999. Quantitative determination of joint incongruity and pressure distribution during simulated gait and cartilage thickness in the human hip joint. *Journal of orthopaedic research : official publication of the Orthopaedic Research Society* 17: 532-539.
129. Carlson CE, Mann RW, Harris WH. 1974. A radio telemetry device for monitoring cartilage surface pressures in the human hip. *IEEE transactions on bio-medical engineering* 21: 257-264.
130. Carlson CE, Mann RW, Harris WH. 1974. A look at the prosthesis-cartilage interface: design of a hip prosthesis containing pressure transducers. *Journal of biomedical materials research* 8: 261-269.
131. Hodge WA, Fijan RS, Carlson KL, et al. 1986. Contact pressures in the human hip joint measured in vivo. *Proceedings of the National Academy of Sciences of the United States of America* 83: 2879-2883.
132. Rushfeldt PD, Mann RW, Harris WH. 1981. Improved techniques for measuring in vitro the geometry and pressure distribution in the human acetabulum. II Instrumented endoprosthesis measurement of articular surface pressure distribution. *Journal of biomechanics* 14: 315-323.
133. Akbar M, Farahmand F, Jafari A, et al. 2012. A detailed and validated three dimensional dynamic model of the patellofemoral joint. *Journal of biomechanical engineering* 134: 041005.

134. An KN, Himeno S, Tsumura H, et al. 1990. Pressure distribution on articular surfaces: application to joint stability evaluation. *Journal of biomechanics* 23: 1013-1020.
135. Chao EY, Volokh KY, Yoshida H, et al. 2010. Discrete element analysis in musculoskeletal biomechanics. *Molecular & cellular biomechanics : MCB* 7: 175-192.
136. Kawai TT, N. 1981. A Discrete Method of Limit Analysis with Simplified Elements. *ASCE Int Conf Comp Civil Engng.*
137. Li G, Sakamoto M, Chao EY. 1997. A comparison of different methods in predicting static pressure distribution in articulating joints. *Journal of biomechanics* 30: 635-638.
138. Volokh KY, Chao EY, Armand M. 2007. On foundations of discrete element analysis of contact in diarthrodial joints. *Molecular & cellular biomechanics : MCB* 4: 67-73.
139. Abraham CL, Maas SA, Weiss JA, et al. 2013. A new discrete element analysis method for predicting hip joint contact stresses. *Journal of biomechanics* 46: 1121-1127.
140. Anderson DD, Iyer KS, Segal NA, et al. 2010. Implementation of discrete element analysis for subject-specific, population-wide investigations of habitual contact stress exposure. *Journal of applied biomechanics* 26: 215-223.
141. Segal NA, Anderson DD, Iyer KS, et al. 2009. Baseline articular contact stress levels predict incident symptomatic knee osteoarthritis development in the MOST cohort. *Journal of orthopaedic research : official publication of the Orthopaedic Research Society* 27: 1562-1568.
142. Segal NA, Kern AM, Anderson DD, et al. 2012. Elevated tibiofemoral articular contact stress predicts risk for bone marrow lesions and cartilage damage at 30 months. *Osteoarthritis and cartilage / OARS, Osteoarthritis Research Society* 20: 1120-1126.
143. Guilak F, Mow VC. 2000. The mechanical environment of the chondrocyte: a biphasic finite element model of cell-matrix interactions in articular cartilage. *Journal of biomechanics* 33: 1663-1673.
144. Halloran JP, Sibole S, van Donkelaar CC, et al. 2012. Multiscale mechanics of articular cartilage: potentials and challenges of coupling musculoskeletal, joint, and microscale computational models. *Annals of biomedical engineering* 40: 2456-2474.

145. Kim E, Guilak F, Haider MA. 2008. The dynamic mechanical environment of the chondrocyte: a biphasic finite element model of cell-matrix interactions under cyclic compressive loading. *Journal of biomechanical engineering* 130: 061009.
146. Stops A, Wilcox R, Jin Z. 2012. Computational modelling of the natural hip: a review of finite element and multibody simulations. *Computer methods in biomechanics and biomedical engineering* 15: 963-979.
147. Anderson AE, Ellis BJ, Maas SA, et al. 2010. Effects of idealized joint geometry on finite element predictions of cartilage contact stresses in the hip. *Journal of biomechanics* 43: 1351-1357.
148. Harris MD, Anderson AE, Henak CR, et al. 2012. Finite element prediction of cartilage contact stresses in normal human hips. *Journal of orthopaedic research : official publication of the Orthopaedic Research Society* 30: 1133-1139.
149. Henak CR, Anderson AE, Weiss JA. 2013. Subject-specific analysis of joint contact mechanics: application to the study of osteoarthritis and surgical planning. *Journal of biomechanical engineering* 135: 021003.
150. Henak CR, Carruth ED, Anderson AE, et al. 2013. Finite element predictions of cartilage contact mechanics in hips with retroverted acetabula. *Osteoarthritis and cartilage / OARS, Osteoarthritis Research Society* 21: 1522-1529.
151. Chegini S, Beck M, Ferguson SJ. 2009. The effects of impingement and dysplasia on stress distributions in the hip joint during sitting and walking: a finite element analysis. *Journal of orthopaedic research : official publication of the Orthopaedic Research Society* 27: 195-201.
152. Pawaskar SS, Ingham E, Fisher J, et al. 2011. Fluid load support and contact mechanics of hemiarthroplasty in the natural hip joint. *Medical engineering & physics* 33: 96-105.
153. Gu DY, Hu F, Wei JH, et al. 2011. Contributions of non-spherical hip joint cartilage surface to hip joint contact stress. *Conference proceedings : Annual International Conference of the IEEE Engineering in Medicine and Biology Society IEEE Engineering in Medicine and Biology Society Conference 2011*: 8166-8169.
154. Russell ME, Shivanna KH, Grosland NM, et al. 2006. Cartilage contact pressure elevations in dysplastic hips: a chronic overload model. *Journal of orthopaedic surgery and research* 1: 6.
155. Armand M, Lepisto J, Tallroth K, et al. 2005. Outcome of periacetabular osteotomy: joint contact pressure calculation using standing AP radiographs, 12 patients followed for average 2 years. *Acta orthopaedica* 76: 303-313.

156. Schuind F, Cooney WP, Linscheid RL, et al. 1995. Force and pressure transmission through the normal wrist. A theoretical two-dimensional study in the posteroanterior plane. *Journal of biomechanics* 28: 587-601.
157. Horii E, Garcia-Elias M, Bishop AT, et al. 1990. Effect on force transmission across the carpus in procedures used to treat Kienbock's disease. *The Journal of hand surgery* 15: 393-400.
158. Hsu RW, Himeno S, Coventry MB, et al. 1990. Normal axial alignment of the lower extremity and load-bearing distribution at the knee. *Clinical orthopaedics and related research*: 215-227.
159. Iwasaki N, Genda E, Minami A, et al. 1998. Force transmission through the wrist joint in Kienbock's disease: a two-dimensional theoretical study. *The Journal of hand surgery* 23: 415-424.
160. Shiba N. 1991. [Biomechanics of the Chiari pelvic osteotomy]. *Nihon Seikeigeka Gakkai Zasshi* 65: 337-348.
161. Yoshida H, Faust A, Wilckens J, et al. 2006. Three-dimensional dynamic hip contact area and pressure distribution during activities of daily living. *Journal of biomechanics* 39: 1996-2004.
162. Blankevoort L, Kuiper JH, Huiskes R, et al. 1991. Articular contact in a three-dimensional model of the knee. *Journal of biomechanics* 24: 1019-1031.
163. Genda E, Iwasaki N, Li G, et al. 2001. Normal hip joint contact pressure distribution in single-leg standing--effect of gender and anatomic parameters. *Journal of biomechanics* 34: 895-905.
164. Kempson G. 1980. The mechanical properties of articular cartilage, Sokoloff L ed. New York: Academic Press; p.
165. Peters CL, Erickson JA, Anderson L, et al. 2009. Hip-preserving surgery: understanding complex pathomorphology. *The Journal of bone and joint surgery American volume* 91 Suppl 6: 42-58.
166. Cunningham T, Jessel R, Zurakowski D, et al. 2006. Delayed gadolinium-enhanced magnetic resonance imaging of cartilage to predict early failure of Bernese periacetabular osteotomy for hip dysplasia. *The Journal of bone and joint surgery American volume* 88: 1540-1548.
167. Kim S, Jessel R, Zurakowski D, et al. 2012. Anterior delayed gadolinium-enhanced MRI of cartilage values predict joint failure after periacetabular osteotomy. *Clinical Orthopaedics and Related Research* 470: 3332-3341.

168. Chai JW, Choi JA, Choi JY, et al. 2014. Visualization of joint and bone using dual-energy CT arthrography with contrast subtraction: in vitro feasibility study using porcine joints. *Skeletal radiology* 43: 673-678.
169. Simoni P, Leyder PP, Albert A, et al. 2014. Optimization of computed tomography (CT) arthrography of hip for the visualization of cartilage: an in vitro study. *Skeletal radiology* 43: 169-178.
170. Ha YC, Choi JA, Lee YK, et al. 2013. The diagnostic value of direct CT arthrography using MDCT in the evaluation of acetabular labral tear: with arthroscopic correlation. *Skeletal radiology* 42: 681-688.
171. Nishii T, Tanaka H, Nakanishi K, et al. 2005. Fat-suppressed 3D spoiled gradient-echo MRI and MDCT arthrography of articular cartilage in patients with hip dysplasia. *AJR American journal of roentgenology* 185: 379-385.
172. Perdikakis E, Karachalios T, Katonis P, et al. 2011. Comparison of MR-arthrography and MDCT-arthrography for detection of labral and articular cartilage hip pathology. *Skeletal radiology* 40: 1441-1447.
173. Tamura S, Nishii T, Shiomi T, et al. 2012. Three-dimensional patterns of early acetabular cartilage damage in hip dysplasia; a high-resolution CT arthrography study. *Osteoarthritis and cartilage / OARS, Osteoarthritis Research Society* 20: 646-652.
174. Anderson AE, Ellis BJ, Maas SA, et al. 2008. Validation of finite element predictions of cartilage contact pressure in the human hip joint. *Journal of biomechanical engineering* 130: 051008.
175. Kapron AL, Aoki SK, Peters CL, et al. 2014. Accuracy and Feasibility of Dual Fluoroscopy and Model-Based Tracking to Quantify In Vivo Hip Kinematics During Clinical Exams. *Journal of applied biomechanics*.
176. Leopold SS, Battista V, Oliverio JA. 2001. Safety and efficacy of intraarticular hip injection using anatomic landmarks. *Clinical orthopaedics and related research*: 192-197.
177. Newberg AH, Munn CS, Robbins AH. 1985. Complications of arthrography. *Radiology* 155: 605-606.
178. Damadian R. 1971. Tumor detection by nuclear magnetic resonance. *Science* 171: 1151-1153.
179. Brown MA, Semelka RC. 1999. MR imaging abbreviations, definitions, and descriptions: a review. *Radiology* 213: 647-662.

180. Westbrook C, Kaut C. 1998. MRI in practice. 2nd ed. Oxford, England: Blackwell Science.
181. Westbrook C. 2002. MRI at a glance. Oxford, England: Blackwell Science.
182. Kumar A, Welti D, Ernst R. 1975. NMR Fourier Zeugmatography. *Journal of Magnetic Resonance* 18: 69-83.
183. Hahn EL. 1950. Spin Echoes. *Physical Review* 80: 580-594.
184. Meiboom S, Gill D. 1958. Modified spin-echo method for measuring nuclear relaxation times. *Review of Scientific Instruments* 29: 688-691.
185. Frahm J, Haase A, Matthaei D. 1986. Rapid three-dimensional MR imaging using the FLASH technique. *Journal of computer assisted tomography* 10: 363-368.
186. Wendt RE, 3rd, Wilcott MR, 3rd, Nitz W, et al. 1988. MR imaging of susceptibility-induced magnetic field inhomogeneities. *Radiology* 168: 837-841.
187. Bitar Y, Holzgrabe U. 2007. Impurity profiling of atropine sulfate by microemulsion electrokinetic chromatography. *Journal of pharmaceutical and biomedical analysis* 44: 623-633.
188. Crawley AP, Wood ML, Henkelman RM. 1988. Elimination of transverse coherences in FLASH MRI. *Magnetic resonance in medicine : official journal of the Society of Magnetic Resonance in Medicine / Society of Magnetic Resonance in Medicine* 8: 248-260.
189. Evans AJ, Hedlund LW, Herfkens RJ, et al. 1987. Evaluation of steady and pulsatile flow with dynamic MRI using limited flip angles and gradient refocused echoes. *Magnetic resonance imaging* 5: 475-482.
190. Hawkes RC, Patz S. 1987. Rapid Fourier imaging using steady-state free precession. *Magnetic resonance in medicine : official journal of the Society of Magnetic Resonance in Medicine / Society of Magnetic Resonance in Medicine* 4: 9-23.
191. Banks DB, Boden RA, Mehan R, et al. 2012. Magnetic resonance arthrography for labral tears and chondral wear in femoroacetabular impingement. *Hip international : the journal of clinical and experimental research on hip pathology and therapy* 22: 387-390.
192. Knuesel PR, Pfirrmann CW, Noetzli HP, et al. 2004. MR arthrography of the hip: diagnostic performance of a dedicated water-excitation 3D double-echo steady-state sequence to detect cartilage lesions. *AJR American journal of roentgenology* 183: 1729-1735.

193. Park SY, Park JS, Jin W, et al. 2013. Diagnosis of acetabular labral tears: comparison of three-dimensional intermediate-weighted fast spin-echo MR arthrography with two-dimensional MR arthrography at 3.0 T. *Acta radiologica* 54: 75-82.
194. Reurink G, Jansen SP, Bisselink JM, et al. 2012. Reliability and validity of diagnosing acetabular labral lesions with magnetic resonance arthrography. *The Journal of bone and joint surgery American volume* 94: 1643-1648.
195. Schmid MR, Notzli HP, Zanetti M, et al. 2003. Cartilage lesions in the hip: diagnostic effectiveness of MR arthrography. *Radiology* 226: 382-386.
196. Sutter R, Zubler V, Hoffmann A, et al. 2014. Hip MRI: how useful is intraarticular contrast material for evaluating surgically proven lesions of the labrum and articular cartilage? *AJR American journal of roentgenology* 202: 160-169.
197. Bittersohl B, Miese FR, Hosalkar HS, et al. 2012. T2* mapping of hip joint cartilage in various histological grades of degeneration. *Osteoarthritis and cartilage / OARS, Osteoarthritis Research Society* 20: 653-660.
198. Ellermann J, Ziegler C, Nissi MJ, et al. 2014. Acetabular cartilage assessment in patients with femoroacetabular impingement by using T2* mapping with arthroscopic verification. *Radiology* 271: 512-523.
199. Lattanzi R, Petchprapa C, Glaser C, et al. 2012. A new method to analyze dGEMRIC measurements in femoroacetabular impingement: preliminary validation against arthroscopic findings. *Osteoarthritis and cartilage / OARS, Osteoarthritis Research Society* 20: 1127-1133.
200. Wyler A, Bousson V, Bergot C, et al. 2009. Comparison of MR-arthrography and CT-arthrography in hyaline cartilage-thickness measurement in radiographically normal cadaver hips with anatomy as gold standard. *Osteoarthritis and cartilage / OARS, Osteoarthritis Research Society* 17: 19-25.
201. Apprich S, Mamisch TC, Welsch GH, et al. 2012. Evaluation of articular cartilage in patients with femoroacetabular impingement (FAI) using T2* mapping at different time points at 3.0 Tesla MRI: a feasibility study. *Skeletal radiology* 41: 987-995.
202. Andreisek G, White LM, Sussman MS, et al. 2009. Quantitative MR imaging evaluation of the cartilage thickness and subchondral bone area in patients with ACL-reconstructions 7 years after surgery. *Osteoarthritis and cartilage / OARS, Osteoarthritis Research Society* 17: 871-878.

203. Crema MD, Guermazi A, Li L, et al. 2010. The association of prevalent medial meniscal pathology with cartilage loss in the medial tibiofemoral compartment over a 2-year period. *Osteoarthritis and cartilage / OARS, Osteoarthritis Research Society* 18: 336-343.
204. Eckstein F, Buck RJ, Burstein D, et al. 2008. Precision of 3.0 Tesla quantitative magnetic resonance imaging of cartilage morphology in a multicentre clinical trial. *Annals of the rheumatic diseases* 67: 1683-1688.
205. Eckstein F, Guermazi A, Roemer FW. 2009. Quantitative MR imaging of cartilage and trabecular bone in osteoarthritis. *Radiologic clinics of North America* 47: 655-673.
206. Nakanishi K, Tanaka H, Nishii T, et al. 1999. MR evaluation of the articular cartilage of the femoral head during traction. Correlation with resected femoral head. *Acta radiologica* 40: 60-63.
207. Wirth W, Nevitt M, Hellio Le Graverand MP, et al. 2010. Sensitivity to change of cartilage morphometry using coronal FLASH, sagittal DESS, and coronal MPR DESS protocols--comparative data from the Osteoarthritis Initiative (OAI). *Osteoarthritis and cartilage / OARS, Osteoarthritis Research Society* 18: 547-554.
208. Roemer FW, Crema MD, Trattnig S, et al. 2011. Advances in imaging of osteoarthritis and cartilage. *Radiology* 260: 332-354.
209. Eckstein F, Hudelmaier M, Wirth W, et al. 2006. Double echo steady state magnetic resonance imaging of knee articular cartilage at 3 Tesla: a pilot study for the Osteoarthritis Initiative. *Annals of the rheumatic diseases* 65: 433-441.
210. Hardy PA, Recht MP, Piraino D, et al. 1996. Optimization of a dual echo in the steady state (DESS) free-precession sequence for imaging cartilage. *Journal of magnetic resonance imaging : JMRI* 6: 329-335.
211. Moriya S, Miki Y, Yokobayashi T, et al. 2009. Three-dimensional double-echo steady-state (3D-DESS) magnetic resonance imaging of the knee: contrast optimization by adjusting flip angle. *Acta radiologica* 50: 507-511.
212. Ruehm S, Zanetti M, Romero J, et al. 1998. MRI of patellar articular cartilage: evaluation of an optimized gradient echo sequence (3D-DESS). *Journal of magnetic resonance imaging : JMRI* 8: 1246-1251.
213. Peterfy CG, Schneider E, Nevitt M. 2008. The osteoarthritis initiative: report on the design rationale for the magnetic resonance imaging protocol for the knee. *Osteoarthritis and cartilage / OARS, Osteoarthritis Research Society* 16: 1433-1441.

214. Mosher TJ, Pruett SW. 1999. Magnetic resonance imaging of superficial cartilage lesions: role of contrast in lesion detection. *Journal of magnetic resonance imaging : JMRI* 10: 178-182.
215. Gold GE, Chen CA, Koo S, et al. 2009. Recent advances in MRI of articular cartilage. *AJR American journal of roentgenology* 193: 628-638.
216. Audenaert EA, Mahieu P, Pattyn C. 2010. Three-Dimensional Assessment of Cam Engagement in Femoroacetabular Impingement. *Arthroscopy*.
217. Beaulé PE, Zaragoza E, Motamedi K, et al. 2005. Three-dimensional computed tomography of the hip in the assessment of femoroacetabular impingement. *J Orthop Res* 23: 1286-1292.
218. Dandachli W, Islam SU, Liu M, et al. 2009. Three-dimensional CT analysis to determine acetabular retroversion and the implications for the management of femoro-acetabular impingement. *J Bone Joint Surg Br* 91: 1031-1036.
219. Butler-Manuel PA, Guy RL, Reynolds DA. 1991. Three-dimensional CT imaging in hip dysplasia. *J Bone Joint Surg Br* 73: 686-687.
220. Beltran LS, Rosenberg ZS, Mayo JD, et al. 2013. Imaging evaluation of developmental hip dysplasia in the young adult. *AJR American journal of roentgenology* 200: 1077-1088.
221. Armiger RS, Armand M, Tallroth K, et al. 2009. Three-dimensional mechanical evaluation of joint contact pressure in 12 periacetabular osteotomy patients with 10-year follow-up. *Acta Orthop* 80: 155-161.
222. Ito H, Matsuno T, Hirayama T, et al. 2009. Three-dimensional computed tomography analysis of non-osteoarthritic adult acetabular dysplasia. *Skeletal radiology* 38: 131-139.
223. Chin MS, Betz BW, Halanski MA. 2011. Comparison of hip reduction using magnetic resonance imaging or computed tomography in hip dysplasia. *Journal of pediatric orthopedics* 31: 525-529.
224. Huppertz A, Radmer S, Asbach P, et al. 2011. Computed tomography for preoperative planning in minimal-invasive total hip arthroplasty: radiation exposure and cost analysis. *European journal of radiology* 78: 406-413.

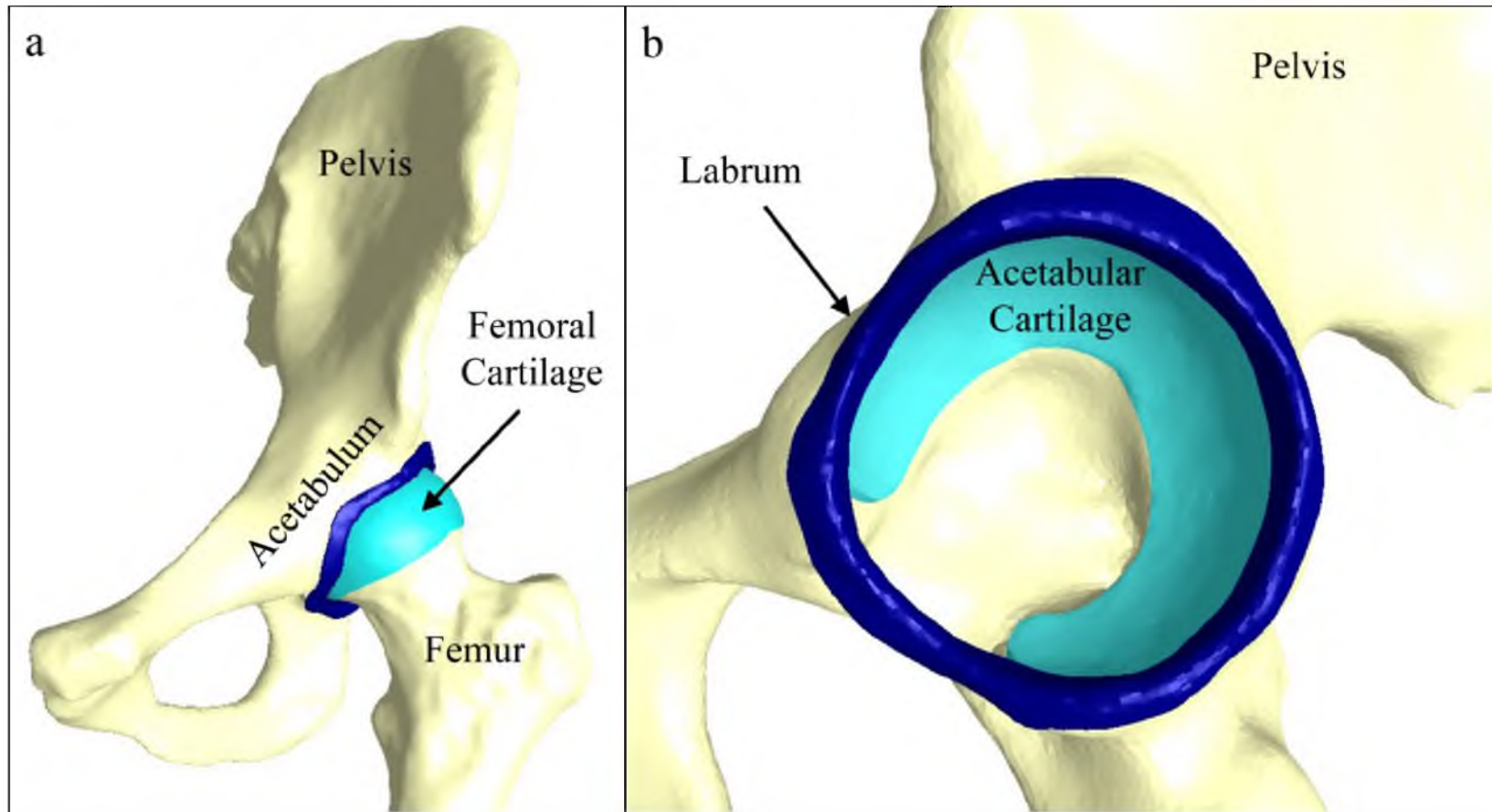


Figure 1.1. Surface reconstructions of a normal left hip joint. (a) Anterior view of the hemipelvis, labrum, and proximal femur with femoral cartilage. (b) Sagittal view of the hemipelvis with acetabular cartilage on the lunate surface and the acetabular labrum.

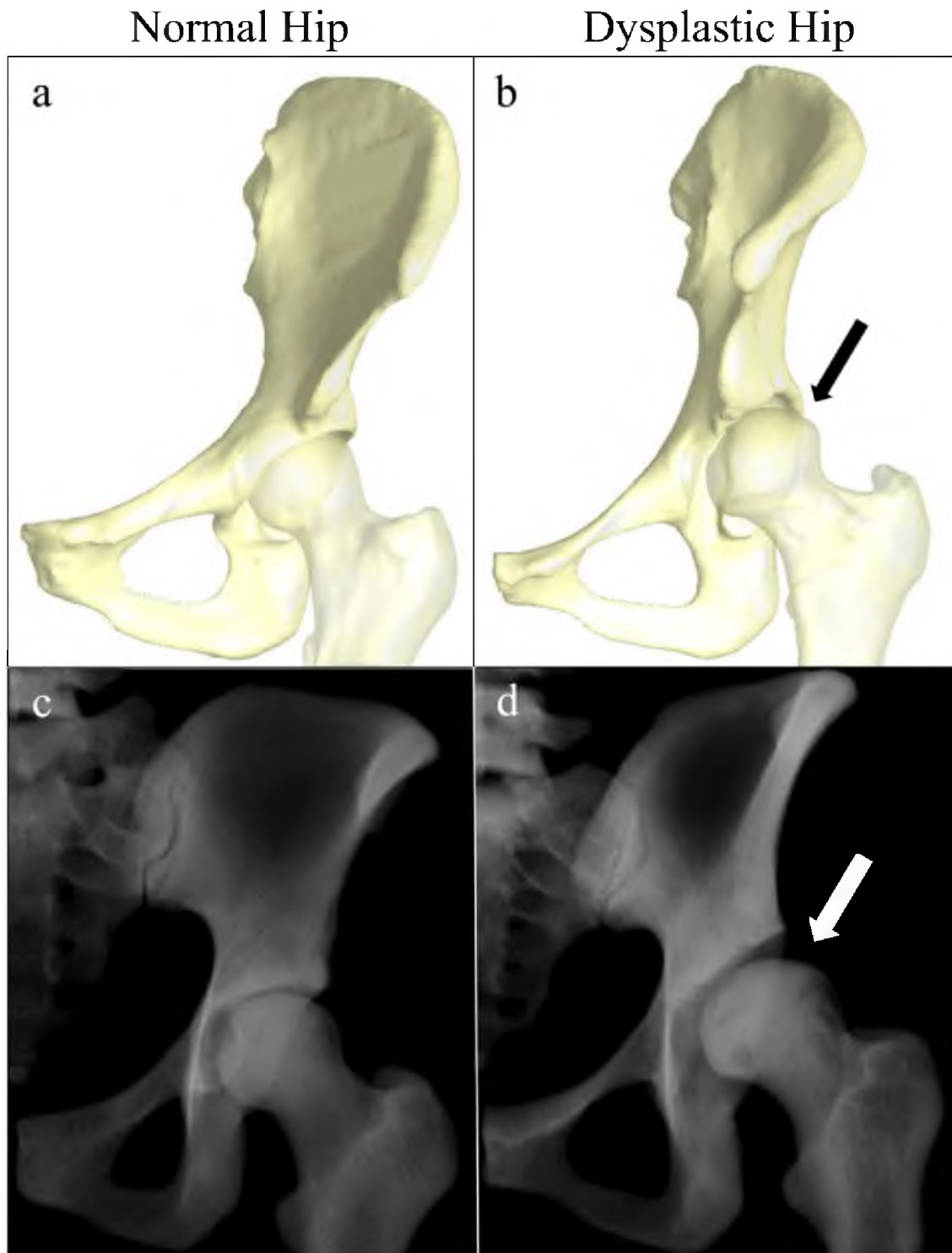


Figure 1.2. Differences in coverage between normal and dysplastic hips. Shallow acetabulum and reduced anterior and lateral femoral coverage in the dysplastic hip is indicated by the arrows in the (b) surface reconstruction and (d) digitally reconstructed radiograph. (a) Surface reconstruction and (c) radiograph of hip with normal anatomy exhibits a more spherical acetabulum with increased coverage.

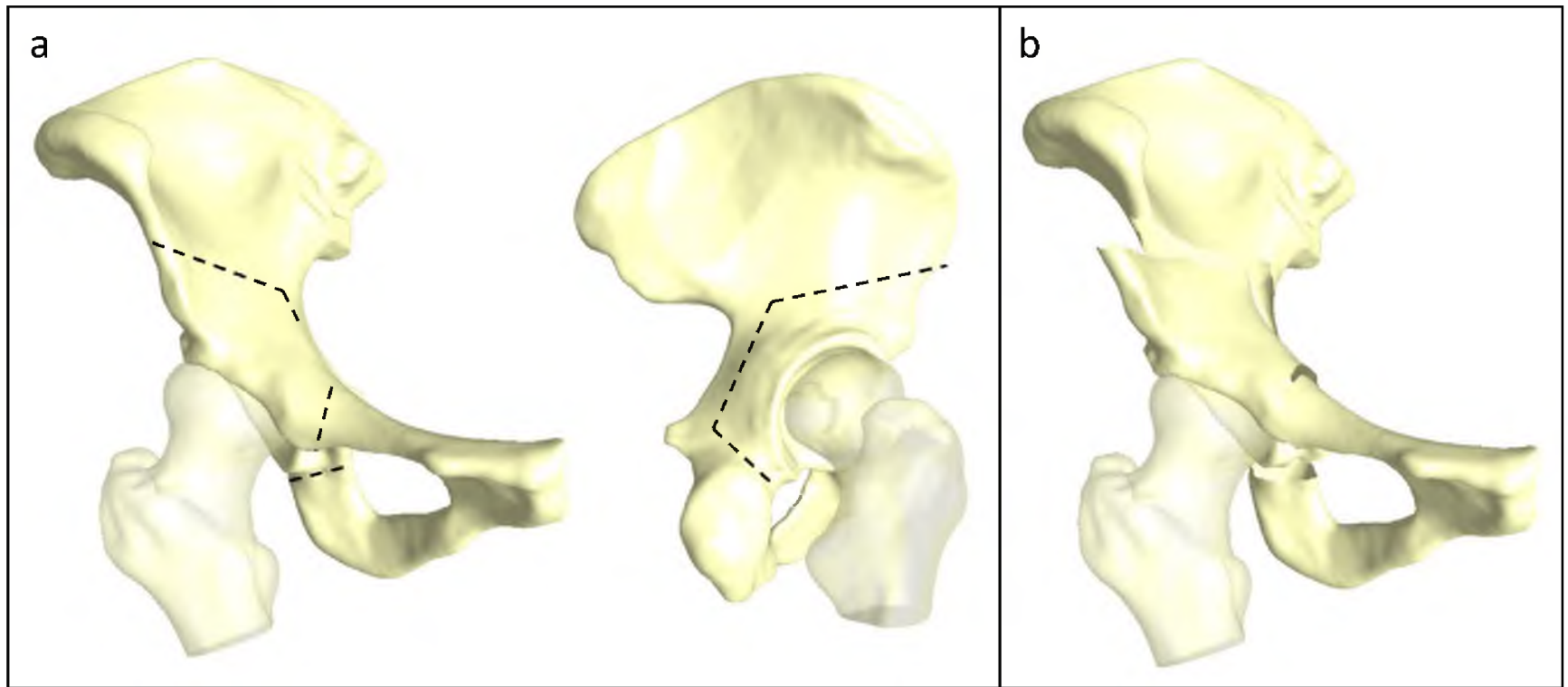


Figure 1.3. Schematic of periacetabular osteotomy (PAO) for treatment of acetabular dysplasia. (a) Preoperatively, there is diminished anterior and lateral coverage of the femoral head. In PAO, the acetabulum is transected from the pelvis, allowing free rotation of the acetabulum. Osteotomy sites are indicated by the dashed lines. (b) Postoperatively, the acetabulum has been rotated anteriorly and laterally to increase femoral coverage. The acetabulum is secured in its new orientation with cortical screws (not pictured).

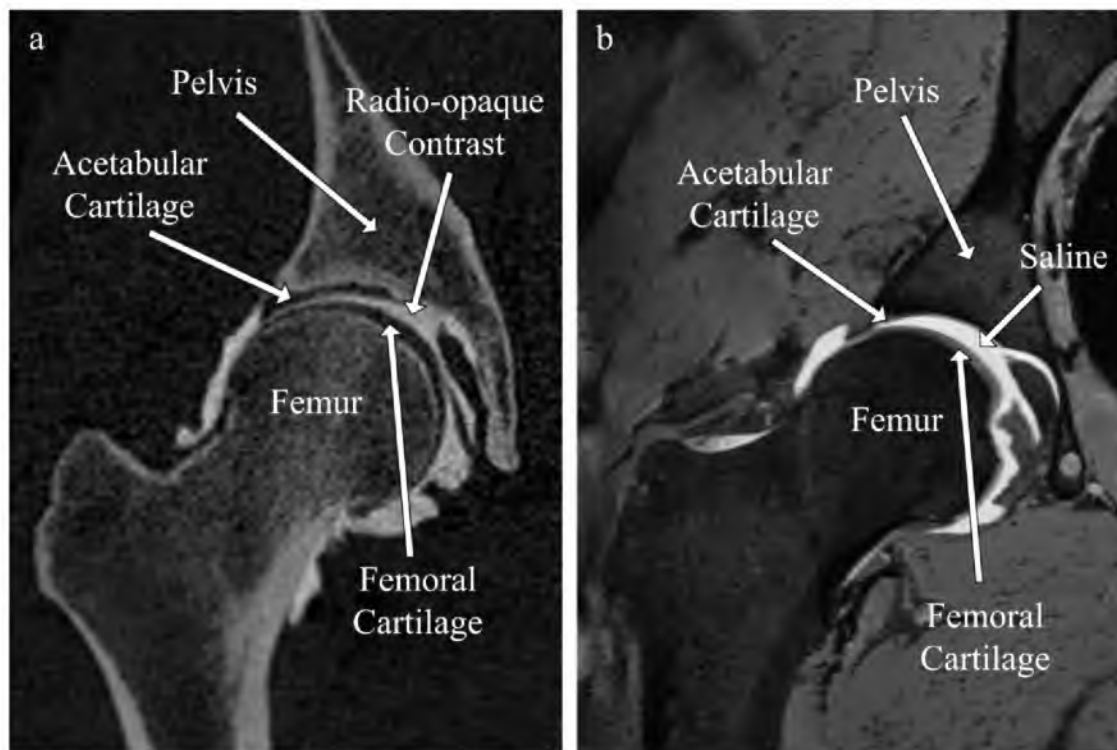


Figure 1.4. Midcoronal images of the hip joint. Traction was applied inferiorly to the femur to distract the joint. (a) Normal hip computed tomography arthrogram (CTA) of healthy control. (b) Normal hip 3D dual echo steady state (DESS) magnetic resonance arthrogram (MRA) of cadaver.

CHAPTER 2

CHANGES IN FEMORAL COVERAGE AND CARTILAGE THICKNESS AFTER PERIACETABULAR OSTEOTOMY

2.1 Abstract

Periacetabular osteotomy (PAO) seeks to improve femoral head coverage and prevent thinning of cartilage in dysplastic hips, but studies have not used patient-specific anatomy to measure changes in joint coverage and cartilage thickness following PAO. The objectives of this study were to quantify three-dimensional (3D) femoral coverage and cartilage thickness in hips with dysplasia before and after PAO.

Computed tomography arthrography (CTA) was performed on five patients with dysplasia before and after PAO. Radiographic measurements of the lateral center edge angle (LCEA), acetabular index (AI), and cross-over sign (CoS) were obtained. 3D surfaces of bone and cartilage were reconstructed from CTA images. The femur was divided into total, medial, lateral, anterior, and posterior regions, and four quadrants. Coverage as well as acetabular and femoral cartilage thickness were quantified on a total and regional basis.

The LCEA significantly increased, AI significantly decreased ($P < 0.001$, 0.002 , respectively), and CoS eliminated following PAO. Coverage did not change significantly overall ($P = 0.505$) or by quadrant (all $P > 0.215$). However, coverage significantly

increased laterally and significantly decreased medially ($P = 0.046, 0.046$, respectively). There were no significant differences in anterior or posterior coverage ($P = 0.594, 0.654$, respectively). Average acetabular and femoral cartilage thickness did not change overall ($P = 0.237, 0.094$, respectively) or by region/quadrant (all $P > 0.112$).

After surgery, radiographic measurements improved, but PAO did not improve coverage overall. Thus, PAO may only improve coverage locally. Though longer-term follow-up studies are necessary, our results suggest PAO may halt further thinning of cartilage.

2.2 Introduction

Acetabular dysplasia is a well-established risk factor for the development of early hip osteoarthritis (OA)^{1,2}. In dysplastic hips, the acetabulum is shallow and does not adequately cover the femoral head. Decreased femoral coverage is believed to cause overloading to cartilage and subsequent deterioration and thinning. Periacetabular osteotomy (PAO) is recommended to restore femoral coverage and prevent or delay OA. In PAO, the acetabulum is transected from the pelvis and reoriented to a position of optimal coverage, confirmed during surgery by measurement of two-dimensional (2D) fluoroscopy images^{3,4}.

Pre- and post-PAO evaluation of dysplastic hips is typically limited to 2D radiographic measures. On anteroposterior (AP) radiographs, the lateral center-edge angle (LCEA) quantifies lateral coverage of the femoral head, the acetabular index (AI) indicates the slope of the sourcil (i.e. weight-bearing region of the acetabulum), and the crossover sign (CoS) assesses the orientation of the acetabulum⁵. While radiographic

measures can identify gross differences in acetabular morphology and coverage, these 2D images cannot describe the complex three-dimensional (3D) anatomy of the hip⁶. Subtle, localized differences in femoral coverage may not be clearly visible on radiographs⁷. Further, though cartilage thickness is an important factor in monitoring outcomes following PAO, the thickness of cartilage can only be inferred as the joint space width on radiographs^{8,9}. Only substantial thinning indicative of advanced OA can be identified with radiographs.

A 3D method capable of accurately quantifying femoral coverage and cartilage thickness before and after PAO could elucidate the effects this surgery has on hip morphology, including its ability to prevent thinning of cartilage. Previous published work has assessed changes in coverage after PAO using computed tomography (CT) images, yet did not utilize the volumetric potential of CT as they did not generate 3D surface reconstructions¹⁰. Instead, Mechlenburg et al. estimated the changes in load-bearing area of the femoral head after PAO using stereologic methods. They found that the projected load-bearing surface increased by an average of 49% postoperatively, which improved coverage to within normal limits¹⁰. While this study did report femoral coverage, the accuracy of their method is limited. Specifically, they only estimated coverage using measurements of 2D images from the CT data, rather than direct analysis of the 3D surfaces. To our knowledge, femoral coverage has not been determined from 3D surfaces before and after PAO.

Therefore, the purpose of this study was to evaluate 3D femoral coverage in dysplastic hips before and after PAO. Additionally, to identify changes in cartilage thickness that may indicate cartilage deterioration, femoral and acetabular cartilage

thickness was analyzed pre- and postoperatively from 3D surfaces generated from computed tomography arthrography (CTA).

2.3 Methods

2.3.1 Subject Selection and Image Acquisition

Five patients with symptomatic acetabular dysplasia were imaged before and after surgical treatment with PAO by a single experienced orthopaedic surgeon (University of Utah IRB# 10983, 43600). All procedures were followed in accordance with the Helsinki Declaration. Preoperatively, patients were diagnosed with acetabular dysplasia based on a LCEA less than 25 degrees and acetabular indices greater than 10 degrees (1 male and 4 female, BMI $21.1 \pm 3.6 \text{ kg}\cdot\text{m}^{-2}$, age 29.8 ± 5.8 years). Follow-up time averaged 19.3 ± 7.2 months, yielding a postoperative age of 31.5 ± 6.3 years. Minimal changes in body mass index were observed (BMI $21.4 \pm 2.9 \text{ kg}\cdot\text{m}^{-2}$).

A validated CT arthrography (CTA) protocol was utilized to capture morphology pre- and postoperatively^{11,12}. A musculoskeletal radiologist prepared a solution of 20 ml of 1% lidocaine (Hospira, Lake Forest, IL, USA), 10 ml of 61% iopamidol (Isovue 300 mg iodine/ml, Bracco Diagnostics, Monroe Township, NJ, USA) and 0.1 ml of 1:1000 epinephrine 1 mg/ml (Hospira, Lake Forest, IL, USA) in a 30 ml lure lock syringe. Approximately 15-25 mL of contrast was injected under fluoroscopic guidance using a lateral oblique approach¹². Traction was applied with a hare-traction splint during CT to distract the joint and delineate between acetabular and femoral cartilage. Images of the pelvis and bilateral femurs were acquired using a 128-section single-source CT machine (SOMATOM Definition™; Siemens Healthcare, Munich, Bavaria, Germany) with the

following settings: 120 kVp, 100-400 mAs, 512 x 512 matrix, 1.0 pitch, 300-400 mm FOV, 1.0 mm section thickness.

Radiographic measures of acetabular morphology are sensitive to patient positioning^{13,14}. Therefore, to obtain standardized radiographic measurements, digitally reconstructed radiographs (DRR) were generated from CTA images pre- and postoperatively to measure lateral femoral coverage, acetabular slope, and acetabular version^{15,16} (Fig. 2.1). CTA image data of the pelvis, sacrum, and bilateral femurs were isolated using segmentation masks and a Boolean operation built into Amira software (v5.4, Visage Imaging, San Diego, CA). A DRR was generated to simulate an anteroposterior (AP) pelvis view. The pelvis was positioned in a neutral position such that the obturator index (ratio of the largest horizontal distance of the obturator foramina) was between 0.8 and 1.2 and the distance from the pubic symphysis to the tip of the coccyx was between 1 and 3 cm⁵. Lateral center-edge angle, acetabular index, and the presence of a crossover sign were measured by one observer as described by Clohisy et al.⁵

2.3.2 Three-dimensional Analysis of Femoral Head Coverage

Bone and cartilage surfaces were segmented semi-automatically in Amira using validated threshold settings^{17,18}. Those images covering the acetabulum and femoral head were up-sampled to three times the original resolution in all planes to minimize stair-case artifact^{15,19}. On the affected hip, cortical bone, and cartilage were segmented for the hemipelvis and proximal femur. Additionally, cortical bone was segmented for the sacrum, and contralateral hemipelvis and femur for alignment and generation of DRRs.

Reconstructed surfaces were triangulated and segmentation artifacts were removed by controlled smoothing using Amira. The pelvis and femur were positioned in the neutral kinematic position of walking at midstance²⁰. An alignment procedure established the neutral position and corrected for the effects of traction as follows. First, the surfaces of the affected hip were rotated about the center of the contralateral acetabulum to correct for obliquity and rotation. Next, the affected femoral head was translated to correspond with the relative positioning between the contralateral pelvis and femur. Finally, the affected pelvis and femur were rotated about the center of the femoral head to achieve the kinematic position of walking at midstance²⁰.

Femoral coverage was quantified by projecting the rim of the bony acetabulum onto the nearest points on the surface of the femoral head. Specifically, a cubic spline was fit to the rim of the cortical bone of the acetabulum. Next, the femoral head was isolated using first principal curvature as calculated in the FEBio software suite²¹. The femoral head was then divided into anatomic regions¹⁵. Three points were used to define the anatomical regions: (1) the center of the sphere fitted to the femoral head, (2) the center of the narrowest cross-section of the femoral neck, and (3) the circumferential center of the femoral shaft just proximal to the lesser trochanter¹⁵. The three points then defined a plane that divided the femoral head anteriorly and posteriorly. A second plane was created perpendicular to the first plane and passed through points (1) and (2) to establish boundaries for the medial and lateral regions. The two bisecting planes then described the following quadrants: anterolateral (AL), anteromedial (AM), posterolateral (PL), and posteromedial (PM). Coverage was then calculated as a percent of the following regions: total, medial (AM + PM), lateral (AL + PL), anterior (AM + AL),

posterior (PM + PL), and by quadrant, where percent was calculated by the following equation:

$$\text{Percent Coverage} = 100\% \times [\text{covered area (mm}^2\text{)} / \text{total area of region (mm}^2\text{)}] \quad (2.1)$$

2.3.3 Three-dimensional Plots of Cartilage Thickness

Acetabular and femoral cartilage thickness was calculated using a validated algorithm¹⁸. First, triangulated faces representing the articular regions of the acetabular cortex and femoral head cortex were selected using first principal curvature in the FEBio software suite²¹. Next, the distance between the outer cartilage surface and cartilage-cortical bone boundary was determined by projecting the vector normal. Cartilage thickness at each surface node was represented as 3D color fringe plot. Average cartilage thickness was calculated when considering the entire surface of acetabular and femoral cartilage, and also by region. Acetabular cartilage was divided in anterior, posterior, and superior regions, whereas the femoral head was divided into the quadrants of AL, AM, PL, and PM as described above.

2.3.4 Statistical Analysis

Paired t-tests were used to identify pre- to postoperative changes in continuous radiographic measures (i.e. LCEA and AI), percent femoral coverage, and cartilage thickness. P-values were adjusted following Finner's procedure when multiple comparisons were performed, such as the four femoral quadrants (i.e. AL, AM, PL, PM), three acetabular regions (i.e. anterior, superior, medial), or two femoral regions (i.e.

medial/lateral or anterior/superior). All statistical analyses were performed in Stata (v 13.0, StataCorp LP, College Station, TX), and plots were generated using SigmaPlot (v 11.0; Systat Software, San Jose, CA). Significance was set at $P \leq 0.05$.

2.4 Results

Qualitative inspection of the 3D surfaces demonstrated that PAO reoriented the acetabulum to increase lateral coverage and corrected acetabular version when retroversion was present (Fig. 2.2). Visualization of the 3D surfaces also demonstrated that posterolateral coverage increased for all patients (Fig. 2.2).

After the PAO procedure, radiographic measures changed significantly. Specifically, the LCEA was significantly increased, AI significantly decreased (Table 2.1) ($P < 0.001$, 0.002 , respectively). Compared to the normal reference ranges for LCEA and AI, all measurements were corrected to normal except the AI in patient #3 (Table 2.1). Finally, for the three patients who presented with acetabular retroversion preoperatively, the CoS was eliminated postoperatively.

2.4.1 Femoral Head Coverage

Overall, percent coverage did not significantly change postoperatively ($P = 0.505$) or by quadrant (all $P > 0.215$). However, by region, coverage significantly increased laterally and significantly decreased medially postoperatively ($P = 0.046$, 0.046 , respectively). There were no significant differences in anterior or posterior coverage ($P = 0.594$, 0.654 , respectively).

2.4.2 Cartilage Thickness

Average acetabular cartilage thickness was 1.40 ± 0.20 mm and 1.55 ± 0.27 mm in the pre- and postoperative states, respectively. Average femoral cartilage thickness was 1.30 ± 0.18 mm and 1.56 ± 0.25 mm in the pre- and postoperative states. Inspection of the 3D fringe plots indicated that acetabular cartilage thickness was thickest in the superolateral region and thinnest in the posteroinferior region in both pre- and postoperative states (Fig. 2.4a,b). Femoral cartilage thickness was thickest around the fovea of the femoral head and generally tapered in thickness towards the femoral neck in both pre- and postoperative states (Fig. 2.4c,d). Average acetabular and femoral cartilage thickness did not change after PAO overall ($P = 0.237, 0.094$, respectively) or by region/quadrant (all $P > 0.112$) (Fig. 2.5a).

2.5 Discussion

To our knowledge, this study is the first to quantify changes in femoral coverage and cartilage thickness calculated using 3D surface reconstructions of bone and cartilage before and after PAO. Our results suggest that despite returning radiographic measurements to the range of normal, PAO does not significantly increase total femoral coverage. Nevertheless, PAO did shift coverage from primarily medial before surgery to balance coverage in the medial and lateral regions after PAO. Also, we did not observe clear signs of cartilage thinning after PAO. Specifically, no significant changes in acetabular or femoral cartilage thickness were observed.

Contrary to common belief^{3,22}, overall femoral coverage did not significantly change after PAO. Considering that PAO does not alter the size or shape of the

acetabulum, it is intuitive that total coverage remains relatively constant. In dysplasia, the acetabulum is under-developed and shallow. While reorienting the acetabulum can redistribute coverage to balance coverage across all regions of the femoral head, the shape of the acetabulum does not change. Thus, the acetabulum may remain shallow postoperatively, thereby explaining why overall coverage of the femoral head did not improve. By regional and quadrant analysis, the only significant differences observed were an increase in lateral coverage and a corresponding decrease in medial coverage. The shift towards increased lateral coverage was observed regardless of acetabular version. However, variability in acetabular version with 3 retroverted and 2 anteverted hips likely impeded our ability to discern statistically significant differences in anterior or posterior coverage as well as changes within individual quadrants after PAO. Nevertheless, visual inspection of 3D surfaces representing the pre- and postoperative states suggest that correction of the acetabulum in PAO may be unique to the patient and depend on the primary region of deficient coverage. In the case of patients who present with acetabular dysplasia and retroversion, coverage was most deficient in the posterolateral region. In contrast, when a CoS was not present, coverage was most deficient anterolaterally.

Our results differ when compared to those of a previous study that used stereologic methods to estimate femoral coverage from CT images. Mechlenburg et al. found an average 49% increase in femoral coverage in dysplastic hips after PAO¹⁰. The conflicting results are likely explained by differences in methodology used to compute coverage. In the prior study, coverage was estimated based on 2D measurements acquired in the sagittal plane. Femoral coverage was calculated by vertical line

projection of the most prominent points of the anterior and posterior acetabulum onto the femoral head. Furthermore, the entire femoral head was selected by Mechlenburg, whereas we only selected the region thought to articulate in the socket (using principal curvature). It is therefore conceivable that use of single vertical line projections would overestimate femoral head coverage. As we considered the entire anatomy of the acetabulum and femoral head to calculate coverage, we believe our method is more accurate and precise than that reported by Mechlenburg. Specifically, Mechlenburg's method required the user to select prominent points, which may be a subjective process, and may not encompass the important details of the acetabulum. Conversely, our method automatically projected a cubic spline representing the entire acetabular rim automatically onto the 3D surface of the femoral head using closest point projection. Finally, the goal of PAO is to increase femoral head coverage about the articulating surface of the femur. Thus, by first isolating the articulating surface of the femoral head, we believe our method to calculate coverage is of greater clinical relevance than that reported previously.

While our study did not incorporate an analysis of coverage in normal hips to serve as a comparison, our coverage results can be qualitatively compared to a prior study that analyzed changes in coverage between normal and retroverted hips²³. Specifically, in the study by Hansen et al., coverage was calculated in the same manner as that performed in our study. Total coverage of dysplastic hips after PAO averaged 51% and remained reduced when compared with previously described coverage of 58% in normal hips²³. Surprisingly, coverage in the AL region was ~17% in normal hips, which is less than our average coverage pre- and postoperatively for dysplastic hips. The most obvious

discrepancy in coverage between normal and dysplastic hips is in reduced coverage in the posterolateral region. Coverage was ~65% in the PL region of normal hips, while coverage averaged 31% preoperatively and increased to 45% postoperatively in dysplastic hips. These findings suggest that reduced posterior coverage due to the shallow acetabulum observed in dysplasia may be as clinically important as reduced anterior coverage.

Changes in radiographic measures served as a clinical metric in which to compare 3D changes in coverage achieved by PAO. Thus, in our study, radiographic parameters for acetabular dysplasia were measured before and after PAO. Given the small sample size, it was not possible to perform linear regression to quantitatively compare radiographic measurements to 3D coverage. However, comparisons between radiographic measurements and 3D coverage can be made qualitatively. Measurements of LCEA and AI indicated that all hips were corrected within normal limits except for AI in patient #3 (Table 2.1). Additionally, the CoS was eliminated in all patients, restoring acetabular anteversion (Fig. 2.2). Despite radiographic parameters of acetabular coverage, slope, and version being corrected after PAO, 3D femoral coverage analysis demonstrated that total coverage remains unchanged. In this regard, one could postulate that radiographs do not provide valuable metrics in which to evaluate femoral head coverage as quantified in 3D. Indeed, previous work has demonstrated that radiographic measures do not correlate with 3D measures of morphology⁶. Therefore, the limitations in assessing 3D coverage based off of 2D radiographic measures must be appreciated within the context of diagnosis and treatment of acetabular dysplasia.

Changes in cartilage thickness after PAO could serve as an indicator of the progression of OA. We did not detect significant differences in acetabular or femoral cartilage thickness following PAO. However, we did observe a trend to indicate possible increases in femoral cartilage thickness. One prior study monitored changes in cartilage thickness in dysplastic hips preoperatively, and at 1 year and 2.5 year follow-up using magnetic resonance imaging²⁴. In agreement with our results, they reported no changes in average thickness of acetabular and femoral cartilage at 2.5 years follow-up. However, at 1 year follow-up, a significant increase in acetabular cartilage of 0.12 mm was observed. The authors speculated that an inflammatory process may have caused cartilage swelling in response to surgery. It is possible that the trend we detected toward increased femoral cartilage thickness is indicative of the same. While our findings and the work by Mechlenburg substantiate the use of PAO as an intervention to delay the progression of OA, it is necessary to interpret our results with caution as the follow-up time to obtain postoperative CTA images was short. Also, considering the limits of spatial resolution of the imaging used, and the associated accuracy of the measurement technique¹¹, changes in cartilage thickness on the submillimeter scale could be due to image noise and variation in the segmentation technique used to create 3D models.

There are limitations that warrant discussion. The small sample size made it difficult to detect significant changes, especially in regional and quadrant analysis where there was likely more variability at the local level in the shape of the acetabulum and femur. Additionally, with a small sample size, it was not feasible to perform linear regression to quantify relationships between radiographic measures and 3D femoral coverage. In addition to a diagnosis of dysplasia, three of the five patients exhibited a

CoS, indicative of acetabular retroversion. Therefore, an additional limitation to this study is that the patient population was inhomogeneous. With a more homogenous population, it is possible we would have observed more significant differences in total and regional coverage. Another limitation is that CTA requires the use of ionizing radiation; the benefit to risk ratio of using CTA must be carefully considered. Also, femoral coverage was calculated for the hip for only one simulated activity of daily living: walking at midstance. We chose walking at midstance because it represents a neutral kinematic position. Consideration of other simulated activities could reveal changes in femoral coverage that were not detected herein. Finally, assessment of cartilage thickness is limited by the accuracy of the imaging protocol. By using a CTA protocol that has been previously validated, we have confidence that our measurements of cartilage thickness are accurate to within ~ 0.5 mm of the true thickness with 95% confidence¹¹. Nevertheless, subtle changes in cartilage thickness could have gone undetected.

In summary, we found that PAO does not increase overall coverage of the femoral coverage, which is contrary to prior research and conventional clinical thought. Rather, we found that PAO serves to balance medial and lateral coverage, by altering coverage on a regional basis. Use of 3D models to represent femoral head coverage could be useful to guide surgical resection of the acetabulum on a per-patient basis. In particular, patients who present with dysplasia and acetabular retroversion may require a PAO that affords improvements in coverage in the posterior and lateral regions, whereas hips with dysplasia that are anteverted may have better outcomes when the acetabulum is rotated laterally and anteriorly. Though we did not observe changes in cartilage thickness,

additional research, with longer follow-up times, is required to quantify the ability of PAO to halt progressive thinning of cartilage. Nevertheless, the methods described herein provide an accurate and precise method to evaluate, in 3D, femoral head coverage and cartilage thickness.

2.6 Acknowledgements

Financial support from NIH #R01 AR053344, #R01 GM083925, #R01 EB016701, and #R21 AR3466184 is gratefully acknowledged. Additional funding was received from the LS Peery Discovery Program in Musculoskeletal Restoration.

2.7 References

1. Ganz R, Leunig M, Leunig-Ganz K, et al. 2008. The etiology of osteoarthritis of the hip: an integrated mechanical concept. *Clinical orthopaedics and related research* 466: 264-272.
2. Jacobsen S, Sonne-Holm S. 2005. Hip dysplasia: a significant risk factor for the development of hip osteoarthritis. A cross-sectional survey. *Rheumatology* 44: 211-218.
3. Ganz R, Klaue K, Vinh TS, et al. 1988. A new periacetabular osteotomy for the treatment of hip dysplasias. Technique and preliminary results. *Clinical orthopaedics and related research*: 26-36.
4. Tibor LM, Sink EL. 2012. Periacetabular osteotomy for hip preservation. *The Orthopedic clinics of North America* 43: 343-357.
5. Clohisy JC, Carlisle JC, Beaulé PE, et al. 2008. A systematic approach to the plain radiographic evaluation of the young adult hip. *The Journal of bone and joint surgery American volume* 90 Suppl 4: 47-66.
6. Stubbs AJ, Anz AW, Frino J, et al. 2011. Classic measures of hip dysplasia do not correlate with three-dimensional computer tomographic measures and indices. *Hip international : the journal of clinical and experimental research on hip pathology and therapy* 21: 549-558.
7. Janzen DL, Aippersbach SE, Munk PL, et al. 1998. Three-dimensional CT measurement of adult acetabular dysplasia: technique, preliminary results in normal subjects, and potential applications. *Skeletal radiology* 27: 352-358.
8. Hartig-Andreasen C, Troelsen A, Thillemann TM, et al. 2012. What factors predict failure 4 to 12 years after periacetabular osteotomy? *Clinical orthopaedics and related research* 470: 2978-2987.
9. Troelsen A, Elmengaard B, Soballe K. 2009. Medium-term outcome of periacetabular osteotomy and predictors of conversion to total hip replacement. *The Journal of bone and joint surgery American volume* 91: 2169-2179.
10. Mechlenburg I, Nyengaard JR, Romer L, et al. 2004. Changes in load-bearing area after Ganz periacetabular osteotomy evaluated by multislice CT scanning and stereology. *Acta orthopaedica Scandinavica* 75: 147-153.
11. Allen BC, Peters CL, Brown NA, et al. 2010. Acetabular cartilage thickness: accuracy of three-dimensional reconstructions from multidetector CT arthrograms in a cadaver study. *Radiology* 255: 544-552.

12. Henak CR, Abraham CL, Peters CL, et al. Computed tomography arthrography with traction in the human hip for three-dimensional reconstruction of cartilage and the acetabular labrum. *Clinical radiology*.
13. Carlisle JC, Zebala LP, Shia DS, et al. 2011. Reliability of various observers in determining common radiographic parameters of adult hip structural anatomy. *The Iowa orthopaedic journal* 31: 52-58.
14. Clohisy JC, Carlisle JC, Trousdale R, et al. 2009. Radiographic evaluation of the hip has limited reliability. *Clinical orthopaedics and related research* 467: 666-675.
15. Harris MD, Reese SP, Peters CL, et al. 2013. Three-dimensional quantification of femoral head shape in controls and patients with cam-type femoroacetabular impingement. *Annals of biomedical engineering* 41: 1162-1171.
16. Metz C. 2005. Digitally reconstructed radiographs. Utrecht: Utrecht University: 79.
17. Anderson AE, Ellis BJ, Peters CL, et al. 2008. Cartilage thickness: factors influencing multidetector CT measurements in a phantom study. *Radiology* 246: 133-141.
18. Anderson AE, Peters CL, Tuttle BD, et al. 2005. Subject-specific finite element model of the pelvis: development, validation and sensitivity studies. *Journal of biomechanical engineering* 127: 364-373.
19. Harris MD, Anderson AE, Henak CR, et al. 2012. Finite element prediction of cartilage contact stresses in normal human hips. *Journal of orthopaedic research : official publication of the Orthopaedic Research Society* 30: 1133-1139.
20. Bergmann G, Deuretzbacher G, Heller M, et al. 2001. Hip contact forces and gait patterns from routine activities. *Journal of biomechanics* 34: 859-871.
21. Maas SA, Ellis BJ, Ateshian GA, et al. 2012. FEBio: finite elements for biomechanics. *Journal of biomechanical engineering* 134: 011005.
22. Leunig M, Siebenrock KA, Ganz R. 2001. Rationale of periacetabular osteotomy and background work. *Instructional course lectures* 50: 229-238.
23. Hansen BJ, Harris MD, Anderson LA, et al. 2012. Correlation between radiographic measures of acetabular morphology with 3D femoral head coverage in patients with acetabular retroversion. *Acta orthopaedica* 83: 233-239.

24. Mechlenburg I, Nyengaard JR, Gelineck J, et al. 2010. Cartilage thickness in the hip measured by MRI and stereology before and after periacetabular osteotomy. *Clinical orthopaedics and related research* 468: 1884-1890.

Table 2.1

Radiographic Measures and Femoral Coverage by Quadrant Pre- and Postoperatively

PT	PREOPERATIVE								POSTOPERATIVE							
	Radiographic Measures			Percent Coverage					Radiographic Measures			Percent Coverage				
	LCEA	AI	Crossover	Overall	AL	AM	PL	PM	LCEA	AI	Crossover	Overall	AL	AM	PL	PM
1	13.5	23.2	yes	48.7	28.1	63.1	26.8	78.7	28.8	9.0	no	49.9	34.9	45.6	42.2	76.7
2	17.0	14.6	yes	53.3	44.3	94.3	13.2	62.1	36.8	4.6	no	59.9	37.1	60.0	51.0	90.6
3	6.0	40.0	no	48.7	21.6	32.1	52.7	85.1	26.0	17.0	no	51.3	35.0	36.6	52.5	78.3
4	9.0	21.3	no	45.6	13.0	40.2	36.9	91.7	28.5	6.5	no	50.2	34.2	36.7	52.4	77.7
5	12.8	19.6	yes	51.4	25.5	71.9	22.9	83.4	30.8	6.7	no	44.8	25.1	56.0	26.9	69.7
AVG	11.7	23.7		49.6	26.5	60.3	30.5	80.2	30.2	8.8		51.2	33.3	47.0	45.0	78.6
STDEV	4.3	9.6		2.9	11.5	25.0	15.0	11.1	4.1	4.9		5.5	4.7	10.8	11.0	7.5

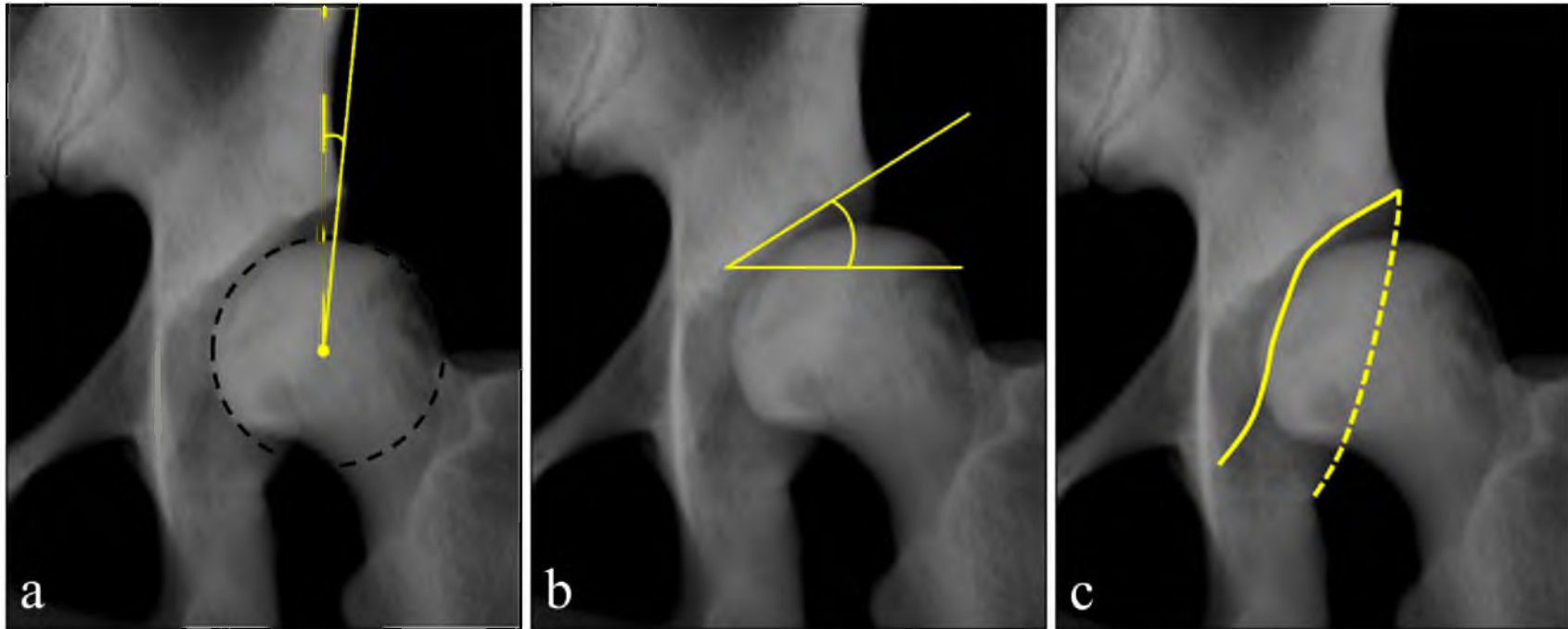


Figure 2.1. Radiographic measures of the anteroposterior pelvis view commonly used in the diagnosis of acetabular dysplasia. a) Lateral center-edge angle: the angle formed by a vertical line and a line connecting the center of the femoral head with the lateral edge of the acetabulum. b) Acetabular index: the angle formed by a horizontal line and the line connecting the medial point of the acetabulum with the lateral point of the acetabulum. c) Crossover sign: positive when the anterior (solid line) and posterior (dashed line) walls of the acetabulum cross (not positive herein).

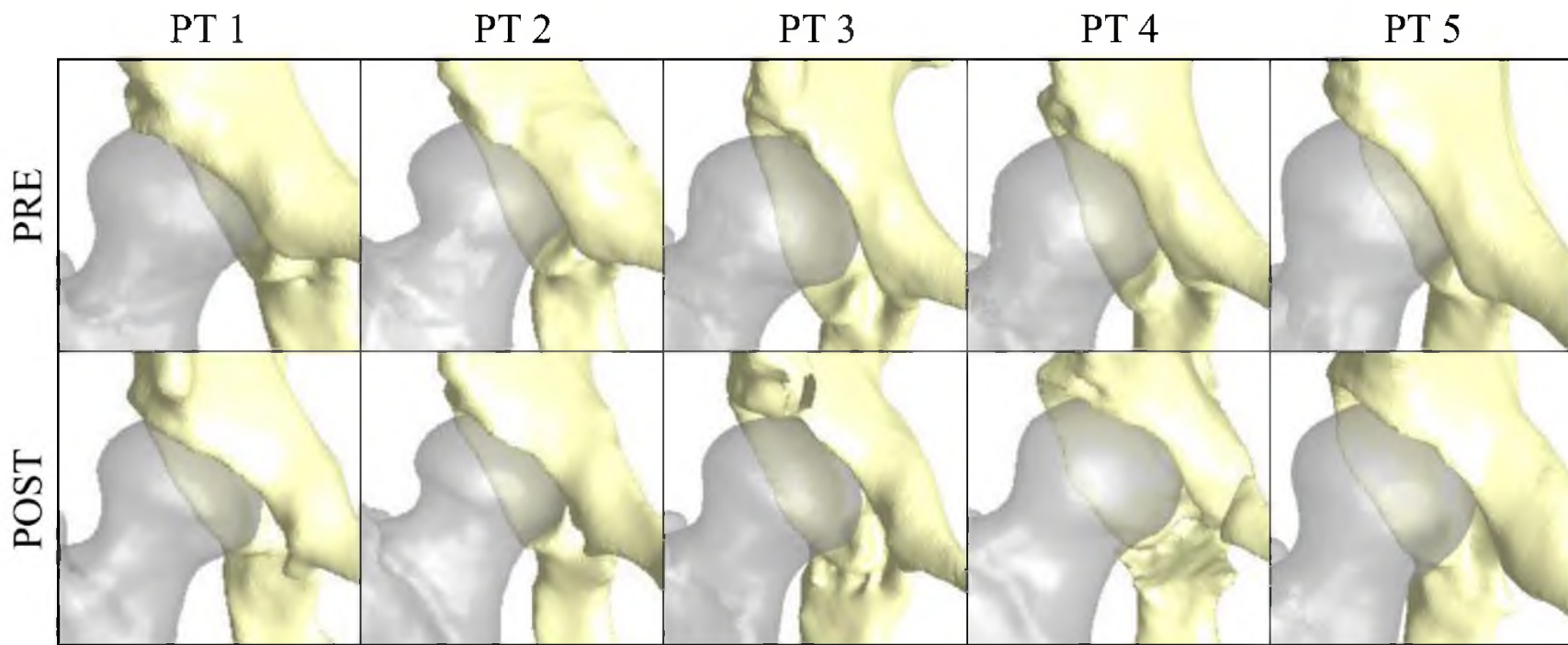


Figure 2.2. Pre- and postoperative 3D surface reconstructions of the femur and pelvis for each patient. Differences in pathologies between patients is evident by the presence of a crossover sign preoperatively in patient # 1, 2, and 5. Patient # 3 and 4 demonstrated less anterior coverage preoperatively. Postoperatively, coverage was more balanced between anterior/posterior and medial/lateral for all patients.

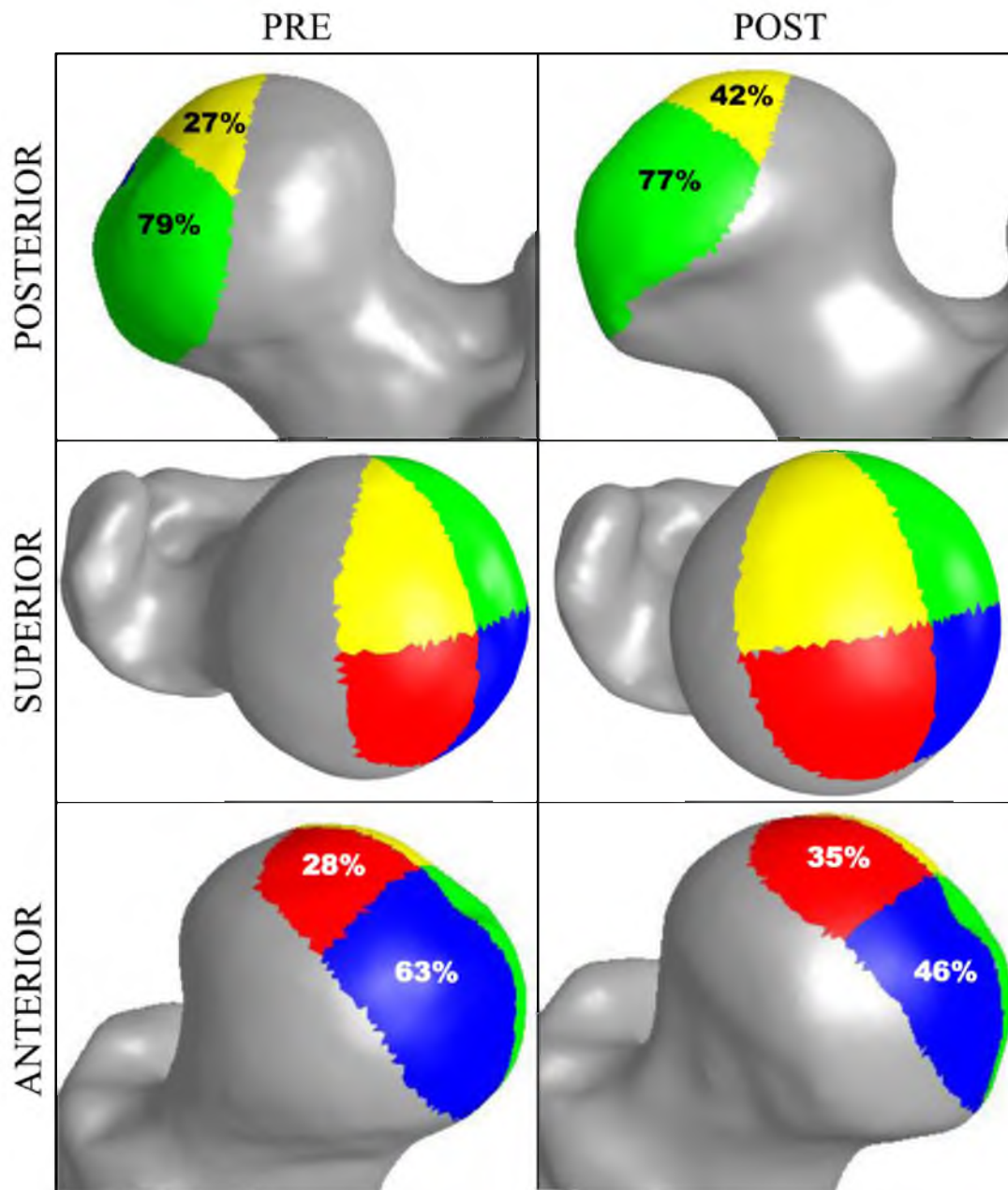


Figure 2.3. Femoral coverage by quadrant displayed on the femur for patient # 1 pre- and postoperatively. Lateral coverage increased and medial coverage decreased postoperatively. Values for coverage is indicated by percent of the regional area covered. For patient # 1, PL (yellow) increased from 27% to 42%, PM (green) decreased from 79% to 77%, AL (red) increased from 28% to 35%, and AM (blue) decreased from 63% to 46%.

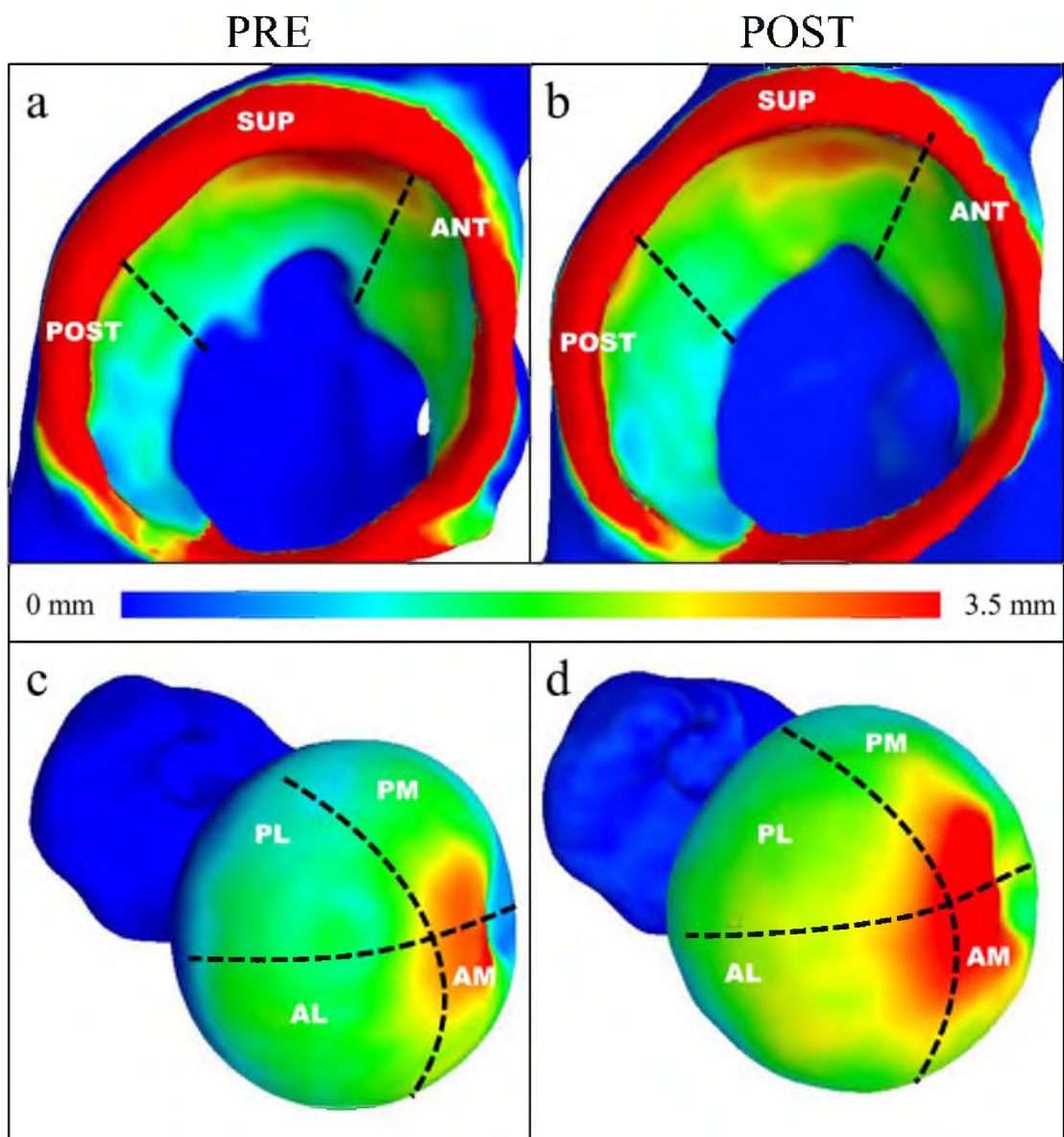


Figure 2.4. Plots of (a, b) acetabular and (c, d) femoral cartilage thickness pre- and postoperatively for patient # 5. General trends in cartilage thickness were consistent pre- and postoperatively. (a, b) Acetabular cartilage was thickest in the superolateral acetabulum and thinnest posteroinferiorly. (c, d) Femoral cartilage was thickest near the fovea and gradually tapered to thin cartilage at the femoral neck. Femoral cartilage was significantly thicker after PAO in all regions (d). Regions of the acetabulum and femoral head analyzed are labelled and indicated by the dashed lines.

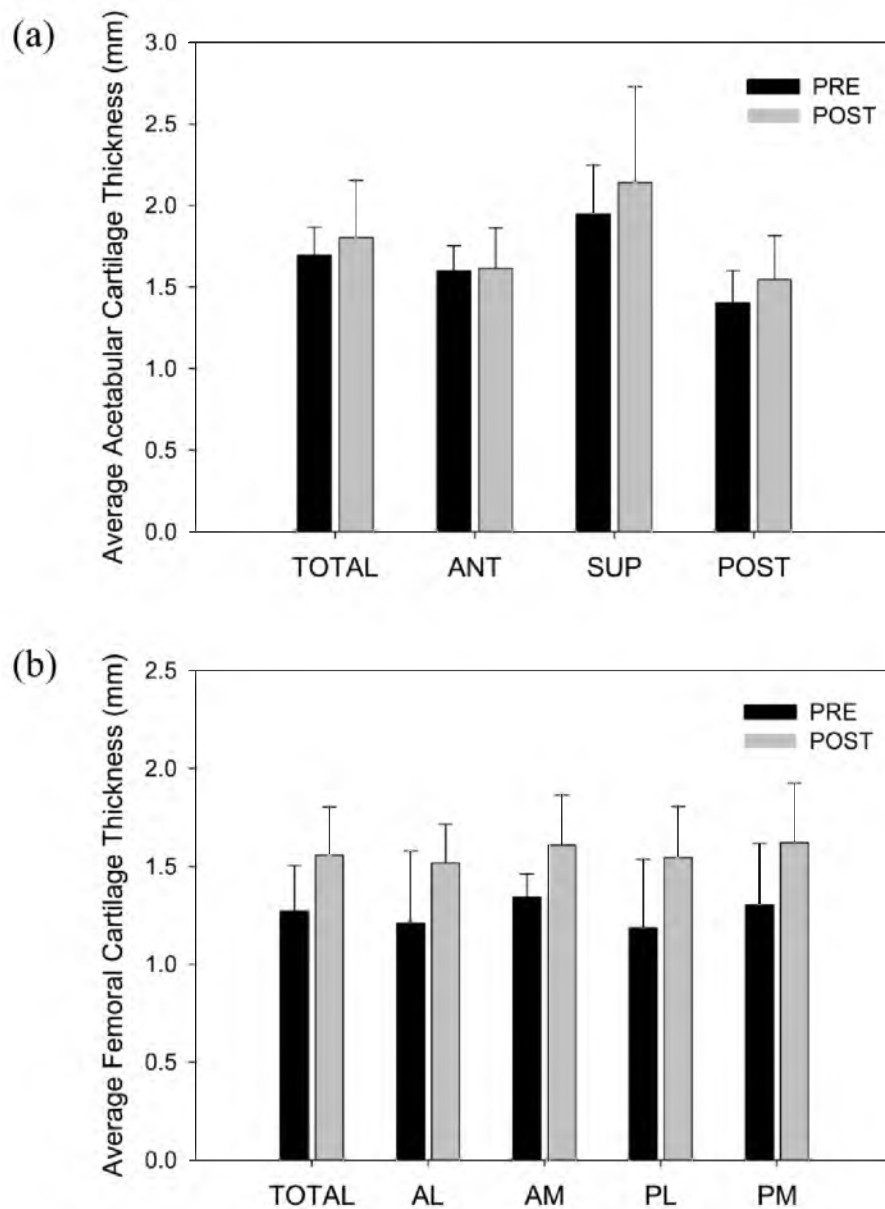


Figure 2.5. Average (a) acetabular and (b) femoral cartilage thickness overall and by region pre- and postoperatively. There were no significant differences in average (a) acetabular or (b) femoral cartilage thickness overall or by region/quadrant.

CHAPTER 3

PATIENT-SPECIFIC CHONDROLABRAL MECHANICS IN ACETABULAR DYSPLASIA FOLLOWING PERIACETABULAR OSTEOTOMY

3.1 Abstract

Periacetabular osteotomy (PAO) seeks to improve hip joint contact mechanics by increasing femoral head coverage. However, studies have not confirmed, using patient-specific anatomy, that PAO reduces contact stress and redistributes load to the cartilage and labrum.

The objective of this study was to evaluate cartilage and labrum mechanics and articular congruency in dysplastic hips before and after PAO using patient-specific finite element (FE) models. Five patients with dysplasia were modeled pre- and postoperatively following a validated FE protocol. Contact stress and area on the labrum and acetabular cartilage as well as labrum load support were compared. Congruency was assessed for walking at midstance (WM) and ascending stairs at heel-strike (AH).

Percent contact increased postoperatively overall, medially, and superiorly ($P=0.008$, <0.001 , <0.001). Peak acetabular contact stress decreased significantly overall, laterally, anteriorly, and superiorly ($P<0.001$, <0.001 , <0.001 , 0.012). Correspondingly, average contact stress decreased overall and in the lateral, anterior, and

posterior regions ($P < 0.001$, 0.001, 0.037). Only average contact stress on the superior labrum and peak labrum stress overall decreased ($P = 0.017$, 0.0218). No changes in load supported by the labrum or contact area labrum contact area were observed. Peak and average congruency improved ($P = 0.011$, 0.003 for WM; $P = 0.021$, < 0.001 , for AH).

PAO can increase contact area and decrease contact stress on the acetabular cartilage, and improve congruency. The procedure also shifted primary loading from areas known to have damage to locations that may provide more effective force transfer. Despite these positive changes, the labrum may continue to experience abnormal loading following PAO.

3.2 Introduction

Approximately one in four people will develop hip osteoarthritis (OA)²²⁷. Reports estimate that as many as 50 percent of cases of hip OA are believed to be the result of acetabular dysplasia^{35,49}. In dysplastic hips, the acetabulum is shallow and under-developed, resulting in an unstable joint with inadequate coverage of the femoral head^{66,228}. It was initially hypothesized that reduced femoral coverage in dysplastic hips caused chronic overload of the articular cartilage^{72,154}. Indeed, many patients with dysplasia have cartilage lesions to support this finding^{76,229}. However, more recent work suggests that the labrum experiences overload in pre-osteoarthritic hips with dysplasia, which may cause an outward-to-in progression of hip osteoarthritis^{1,23}. Therefore, both the labrum and cartilage appear to play an important mechanical role in the modulation of OA in hips with dysplasia.

Periacetabular osteotomy (PAO) has been a mainstay treatment for dysplasia. In PAO, the acetabulum is transected from the pelvis and reoriented into a position that increases anterolateral coverage^{60,72,79}. It is believed that by normalizing radiographic measures during surgery such as the center-edge angle (CEA), joint coverage is restored, and degeneration is prevented or delayed. Mid- to long-term clinical follow-up studies have demonstrated positive outcomes after PAO^{88,89,230}. However, the procedure is technically demanding¹⁰², and as many as 40% of dysplasia patients treated with PAO eventually require total hip arthroplasty for end-stage OA⁹⁰.

Ultimately, the goal of PAO is to restore hip contact mechanics by normalizing anatomical relationships between the pelvis and femur. A quantitative understanding of cartilage and labrum (i.e. chondrolabral mechanics) before and after the PAO procedure could thus provide valuable data to refine surgical procedures to increase the number of positive outcomes. Hip chondrolabral mechanics cannot be measured in-vivo, but they can be estimated using computational techniques, such as the finite element (FE) method^{1,23,98,127,148,150,154,176}. Likely due to the inherent difficulties of imaging and generating accurate geometrical surface reconstructions, most models to date have made simplifying assumptions to the cartilage representation and do not model the labrum^{98,127,148,150,154,176}. Unfortunately, when bone is assumed to be perfectly spherical and/or cartilage is assigned constant thickness, computational models predict unrealistic, concentric contact distributions with contact stress magnitudes that are not physiological^{148,153}. In addition, as the labrum has been shown to undergo loading in dysplastic hips, inclusion of this tissue structure appears to be essential to elucidate the pathomechanics of hip dysplasia^{1,23}.

Patient-specific FE models that accurately incorporate geometry of bone and cartilage can predict mechanics in good agreement with stress data obtained *in vitro*^{127,176}. Prior work that has modeled contact mechanics in the dysplastic hip with patient-specific bone and cartilage is limited to preoperative models, and showed mixed conclusions^{1,154}. Russell et al. found significantly elevated cartilage stresses in the dysplastic hips compared to healthy hips¹⁵⁴, whereas Henak et al. did not find increased contact stresses in dysplastic hips¹. However, Henak et al. did find that the labrum in dysplastic hips experienced significantly larger load support; they concluded the labrum may compensate for reduced acetabular coverage and protect acetabular cartilage from stress overload¹. This conclusion could not be reached by Russell et al. as the labrum was not included¹⁵⁴.

Prior studies suggest that hip mechanics may be dictated by factors other than the coverage of the joint. In dysplastic hips, the shape of the acetabulum and femoral head may be abnormal²³¹⁻²³³, influencing the degree of congruency between the two articulating surfaces¹. With this in mind, it is possible that after reorienting the acetabulum in PAO, congruency of the joint may be reduced, causing focal loading to cartilage. However, this remains to be known as patient-specific anatomy for the cartilage, bone, and labrum has not been used when developing and analyzing computer models to predict hip mechanics in dysplastic hips treated with PAO.

Overall, it is unclear if PAO improves hip contact mechanics as theorized. A quantitative understanding of how the PAO procedure decreases mechanical load to both the labrum and cartilage, overall and regionally, could yield data valuable to refine surgery and improve clinical outcomes. The objectives of this study were to compare

chondrolabral contact mechanics and joint congruency in dysplastic hips pre- and postoperative PAO during activities of daily living using a validated patient-specific FE modeling protocol^{150,176}.

3.3 Methods

Five patients with symptomatic acetabular dysplasia (1 male and 4 female, BMI $21.1 \pm 3.6 \text{ kg}\cdot\text{m}^{-2}$, age 29.8 ± 5.8 years) underwent surgical treatment with PAO by a single experienced orthopaedic surgeon (author CLP). Each patient was imaged using radiographs and CT arthrography before and after surgery, at minimum 1 year follow-up (19.3 ± 7.2 months, yielding a postoperative age of 31.5 ± 6.3 years). All research procedures were performed in accordance with the Helsinki Declaration with informed consent and institutional board approval (University of Utah IRB 10983, 43600). Preoperatively, patients had a CEA less than 25 degrees (11.7 ± 4.3 degrees) and acetabular indices greater than 10 degrees (23.7 ± 9.6 degrees). The lateral CEA was increased and acetabular indices were decreased to normative levels with a CEA 30.2 ± 4.1 degrees and acetabular index 8.8 ± 4.9 degrees. Body mass index (BMI) was nearly identical following surgery (BMI $21.4 \pm 2.9 \text{ kg}\cdot\text{m}^{-2}$).

Patient-specific FE models representing pre- and postoperative cartilage, labrum, and bone anatomy were generated using image data obtained from a validated CT arthrography (CTA) protocol^{1,23,127,149,150,176}. Briefly, patient-specific surface reconstructions (Fig. 3.1) were created from cartilage, labrum, cortical bone, and trabecular bone segmentations. Cartilage, labrum, and bone mesh densities and constitutive models followed published validation and sensitivity studies (Fig.

3.1)^{23,127,176}. A range of anatomical positions and loads were applied to each FE model to analyze activities of walking at toe-off (WTO, 205% BW), midstance during walking (WM 203% BW), the transition of heel-strike and midstance for stair descent (DHM 230% BW), and heel-strike during stair ascent (AH, 252% BW) using Bergmann's data². During loading, the pubis and sacroiliac joint of the hemipelvis were held rigid, but the remaining bone was modeled as a deformable body¹⁷⁶. All FE models were analyzed with NIKE3D²³⁴.

Peak and average contact stress and contact area were recorded on the surface of the acetabular cartilage and labrum²³. Average contact stress was calculated for those nodes where contact stress was greater than 0 MPa. For each activity, fringe plots were generated to map the average acetabular cartilage contact stress across all patients onto a representative mesh. To select the representative mesh, the articulating surface of acetabular cartilage from each patient mesh was fit to a sphere. The mesh that had a radius closest to the average radius was designated the representative patient mesh. Contact area was calculated at all faces with a positive value for contact stress and presented as a percentage of the total surface area of the cartilage. The load supported by the labrum was reported as a percentage of the total load on the cartilage and labrum. Congruency of the articular surfaces was calculated following established methods^{1,235}. Congruency was defined as a root-mean-square (RMS) curvature value such that smaller values indicate a more congruent surface. Congruency was determined for cartilage at points in contact in the final position of WM and AH. WM and AH models were chosen because these activities correspond to the most neutral and extreme kinematic angles analyzed herein, respectively^{1,2}. The point of peak congruency (i.e. most congruent

point and smallest RMS value) and average congruency were reported. Contact stress, contact area, and congruency were evaluated in the lateral and medial regions, and in the anterior, superior, and posterior regions (Fig. 3.2). Pre- and postprocessing was performed using PreView and PostView, respectively (<http://mrl.sci.utah.edu/software.php>).

All differences between pre- and postoperative states were assessed statistically using a mixed-effects linear regression. Changes in peak and average contact stress, and percent contact area were analyzed for all activities as a function of region. Load carried by the labrum was analyzed by activity. Differences in peak and average congruency were evaluated by region and over the total articulating surface for WM and AH. Finner's procedure was used for multiple comparisons²³⁶. All statistical analyses were performed in Stata (v 13.0, StataCorp LP, College Station, TX), with plots generated using SigmaPlot (v 11.0; Systat Software, San Jose, CA). Significance was set at $P \leq 0.05$.

3.4 Results

Contact patterns for all patients were bicentric pre- and postoperatively (Fig. 3.3). Contact stresses appeared more focal in the preoperative state for all of the patients (Fig. 3.3). When mapped to the representative patient mesh, the anterolateral rim exhibited concentrated regions of elevated contact stress (Fig. 3.4). Contact was also focused laterally preoperatively (Fig. 3.4). Postoperatively, contact shifted medially and demonstrated loading primarily in the superomedial acetabulum for all activities (Fig

3.4). Additionally, the load appeared better distributed postoperatively, with additional regions of acetabular cartilage in contact.

Peak acetabular cartilage contact stress significantly decreased from 20.03 ± 5.26 MPa pre- to 13.31 ± 3.75 MPa postoperatively across all activities and all patients ($P < 0.001$). Average contact stress significantly decreased from 4.28 ± 3.14 MPa pre- to 3.66 ± 2.38 MPa postoperatively across all activities and all patients ($P < 0.001$). With the analysis portioned into the lateral and medial regions, a significant decrease in peak and average contact stress in the lateral region was observed postoperatively (Fig. 3.5a,b) ($P < 0.001$, $P < 0.001$, respectively). Conversely, average contact stress significantly increased medially for all patients ($P = 0.003$); peak contact stress trended towards a significant increase medially (Fig. 3.5a,b) ($P = 0.071$). With the analysis partitioned into three regions of anterior, superior, and posterior (Fig. 3.2b), average contact stress significantly decreased postoperatively in the anterior and posterior regions (Fig. 3.5b) ($P = 0.001$, 0.037 , respectively). Peak contact stress was significantly smaller postoperatively in the anterior and superior regions; a trend towards a significant decrease was observed posteriorly (Fig. 3.5a) ($P = < 0.001$, 0.012 , 0.057 for anterior, posterior, superior, respectively).

The percent of acetabular cartilage in contact significantly increased postoperatively across all activities and all patients (Fig. 3.5c) ($P = 0.008$). Specifically, percent contact significantly increased medially and superiorly across all activities and all patients (Fig. 3.5c) ($P < 0.001$, $P < 0.001$, respectively).

When considering all subjects and activities, average contact stress was reduced postoperatively on the superior labrum for all patients and activities (Fig. 3.6a) ($P =$

0.017). Peak contact stress on the labrum was significantly reduced considering the total surface ($P = 0.0218$), however, there were no significant changes by region. Despite the change in contact stress, contact area on the labrum did not change for all activities on a regional basis (Fig. 3.6b). Additionally, there were no significant changes in load supported by the labrum in all activities (Fig. 3.6c).

Postoperatively, femoral and acetabular cartilage were more congruent (i.e. smaller RMS values) in almost all regions for both WM and AH (Fig. 3.7). Peak congruency improved in WM postoperatively across the total articulating surface, medially, and superiorly (Fig. 3.7a) ($P = 0.011, <0.001, 0.003$, respectively). Average congruency also improved in WM across the total articulating surface, laterally, and anteriorly (Fig. 3.7b) ($P = 0.003, <0.001, 0.005$, respectively). In AH, average and peak congruency significantly decreased over the total surface and laterally (Fig. 3.7c,d) ($P <0.001, <0.001$, respectively for average congruency; $P = 0.021, 0.003$, respectively for peak congruency). Additionally, congruency improved superiorly for AH (Fig. 3.7d) ($P = <0.001$).

3.5 Discussion

PAO has become the accepted treatment for acetabular dysplasia. The rationale for the procedure is that surgery improves coverage and hip contact mechanics. The focus of this study was to compare chondrolabral mechanics and congruency of articulating surfaces after PAO with patient-specific geometry for bone, cartilage, and labrum. This study is the first, to our knowledge, to model chondrolabral mechanics in dysplastic hips pre- and postoperative PAO using patient-specific anatomy. Our findings

suggest that PAO may be efficacious at preventing OA; peak and average acetabular cartilage contact stress was reduced, contact area was increased, and articular congruency was significantly improved. However, we found only minor changes in labral mechanics following surgery. The role of continued loading to the labrum as a modulator of OA in dysplastic hips treated with PAO requires additional investigation.

Chronic exposure to static compression damages cartilage structure *ex-vivo*, where greater loads are increasingly harmful²³⁷. In addition, it has been suggested that hip dysplasia results in a chronic stress overload of cartilage¹⁵⁴. Therefore, the rationale for PAO is that by reorienting dysplastic acetabuli to increase anterolateral coverage, contact stress will be reduced, thereby preventing or delaying progression to end-stage hip OA. Inspection of FE contact patterns pre- and postoperatively predicted in our study qualitatively support the use of PAO: we observed an increase in contact area and shift from more focal loading anterolaterally to regions of larger contact medially and superiorly (Figs. 3.3,3.4). Quantitatively, our results also support the theory that PAO prevents OA by demonstrating increased medial and superior contact area, which contributed to the overall increase in the total percent contact area observed postoperatively (Fig. 3.5c). PAO is also believed to decrease load to the lateral acetabulum and medialize contact^{72,95}. Our results support that contact increases medially, but we showed that lateral contact remains unaltered (Fig. 3.5c). This suggests that although the lateral acetabular cartilage is still loaded, the load is better distributed as evidenced by a significant decrease in peak and average contact stress laterally as well as more diffuse contact patterns overall (Figs. 3.3, 3.4, 3.5a,b).

Increased contact area theoretically prompts lower contact stresses. Considering all patients and activities, we indeed found that maximum and average acetabular cartilage contact stress were significantly reduced postoperatively. The most pronounced reductions in cartilage contact stress were in the lateral and anterior regions. This may be a key factor in explaining the good clinical success of PAO; focal cartilage lesions, subchondral cysts, and cartilage delaminations are typically described in the anterolateral compartment of the acetabulum in dysplastic hips^{76,229}. After PAO, contact stress was decreased in the anterolateral acetabular cartilage, and therefore could theoretically halt the progression of OA in this region. Beyond reducing contact stress laterally and anteriorly, PAO also increased loading medially as exhibited by increased average contact stress and contact area (Fig. 3.5b). By redistributing load across the acetabular cartilage as a whole, PAO improves articular mechanics.

While significant changes in acetabular cartilage mechanics were observed after PAO, labral mechanics were not as appreciably altered. The only previously reported consistent difference in labral mechanics between normal and dysplastic hips for all activities was an increase in contact area on the superior labrum¹. This could indicate that the most harmful differences in labral mechanics are specific to the superior region in dysplastic hips. Our results demonstrate a slight decrease in contact area of the superior labrum, with a corresponding significant decrease in average contact stress. These differences suggest that load is better distributed in the superior labrum postoperatively, in spite of the lack of change in total load supported by the labrum. The percent load supported by the labrum in dysplastic hips has been reported to be 2.8 to 4.0 times larger than in normal hips¹. Despite the increase in medial joint contact after PAO, the labrum

remained in contact and supports load. This may be a result of excessively prominent hypertrophied labra in dysplastic hips; the labrum overhangs from the acetabular rim, making contact and loading inevitable pre- and postoperatively (Fig. 3.8). Upon further inspection, we qualitatively observed that the labrum undergoes less displacement after PAO (Fig. 3.8). Therefore, while mechanics of the labrum are not normalized, they appear to be improved, with the most substantial of changes occurring in the superior labrum.

Rotation of the acetabulum disrupts the native congruency between articular surfaces, which may have undesired effects on chondrolabral mechanics following PAO. Prior quantitative evaluation of articular congruency concluded that the unloaded medial region was significantly less congruent in dysplastic hips compared to healthy hips¹. Our study was the first to show that congruency improved following surgery; all regions demonstrated a trend towards enhanced peak and average congruency (Fig. 3.7). Improvements in joint congruency likely modulated decreases in contact stress and increases in contact area. Additional research is necessary to quantify the relative role congruency has on reducing contact stress following surgery.

Positive changes in contact stress, contact area, and articular congruency may be sensitive to the degree of correction achieved by acetabular reorientation. Iatrogenic pincer type femoroacetabular impingement following PAO is a well-known phenomenon, but the appropriate degree of acetabular reorientation is difficult to define. Over-correction may shift contact excessively medial. With elevated stress on the medial wall of the acetabulum, cartilage may become overloaded (i.e. acetabular protrusion)^{238,239}. One patient (PT 4, Fig. 3.3) demonstrated what may be excessive medial contact during

WM. It is worthy to note that this was the only patient to experience increased average contact stress on acetabular cartilage postoperatively. Surprisingly, this patient had a postoperative CEA that was within the normal range at 28.5°. This illustrates the potential importance of three-dimensional evaluations of anatomy to aide in preoperative planning, and emphasizes the complex nature of mechanics that may only be revealed using anatomically accurate computational models.

Prior studies have estimated mechanics before and after PAO with simplified models. Zhao et al. altered the geometry of a normal hip to simulate dysplasia and modeled varying degrees of acetabular reorientation to estimate the effects of PAO using FE models⁹⁸. Armiger et al. used discrete element analysis to predict acetabular contact stress and contact area before and after PAO when assuming constant cartilage thickness and nondeformable bones⁹⁵. These studies had similar conclusions to our study: that PAO shifts contact medially and reduces cartilage contact stress. However, use of constant cartilage thickness is known to predict larger contact areas with diffuse contact patterns, and use of rigid bones may over-estimate stresses¹⁴⁸. Also, simulated dysplasia may not be a realistic surrogate for actual dysplasia as it will not capture subtle differences or concomitant deformities. As a result, contact mechanics reported from these prior studies were not physiologically realistic. Estimates of contact area in the study by Armiger et al. averaged $1559 \pm 460 \text{ mm}^2$ and $2337 \pm 451 \text{ mm}^2$ pre- and postoperatively, respectively. Compared to our results, contact areas reported by Armiger et al. were ~5 times larger; compared to a prior study that modeled normal hips using subject-specific anatomy, Armiger's estimates of contact area were nearly 4 times larger^{95,149}. Therefore, estimates of mechanics in prior studies that did not accurately

represent tissue anatomy should be interpreted with caution, as predictions are considerably altered when simplified or simulated geometry with nondeformable bones are used. Finally, prior pre- and postoperative FE models did not include the labrum, which is known to have an important role in the mechanics of dysplastic hips⁹⁵.

Comparing values of average contact stress to prior patient-specific FE models of dysplasia, we report larger stresses. This is because our calculations of average stress were based on nodes with positive contact stress. In contrast, Henak et al. averaged contact stress at all nodes on the articulating surface, where more than half of the values are 0 MPa because they are not loaded (~30% of the acetabular cartilage is in contact for a given activity). Therefore, average contact stresses are substantially lower, ~1 MPa¹. In our study, averages corresponded well with Henak et al. when the average was calculated for all nodes on the articular surface; overall average contact stress was 0.71 ± 2.02 MPa pre- and 0.69 ± 1.73 MPa postoperatively.

There are some limitations that warrant discussion. The complex process to generate and analyze patient-specific FE models and repeated CT scans prohibited use of a large sample size. However, having patients serve as their own control strengthened the statistical analysis. Additionally, the degree of acetabular dysplasia in this patient group was not severe. Mechanics may differ in cases of extreme dysplasia where the deformity may introduce superfluous complexities including femoral pathologies. Follow-up time was an average of 19 months. It is possible that bone and/or cartilage remodeling may occur over a period of longer follow-up. Patients with dysplasia have been noted to have altered gait patterns; in walking, patients exhibit reduced hip extension, increased pelvic drop and rotation, and reduced ground reaction force compared to healthy controls^{62,64}. It

is unclear whether PAO improves gait kinematics, or if they remain altered^{240,241}. Our simulations applied identical kinematics from in-vivo data pre- and postoperatively. This assumption accentuated changes in mechanics due to PAO rather than altered kinematics². Cartilage was modeled as nearly-linear and nearly-incompressible hyperelastic, which is a simplification of articular cartilage behavior^{12,127,150}. Despite this simplification, the model has shown to predict mechanics in good agreement experimental results^{127,176}. Although the labrum was modeled according to its fiber structure²⁶ and represented as transversely isotropic hyperelastic²⁴², material coefficients were derived from bovine tissue. Prior work has demonstrated that labral mechanics were more affected by the constitutive model representation than differences in material coefficients²³. Therefore, changes in model predictions are likely minimal. Finally, the position of boundary between articular cartilage and labrum influences cartilage and labral mechanics. Cartilage and labral tissue are indistinguishable from each other on CTA. However, the boundary was objectively determined in a consistent manner using curvature of the underlying acetabular bone.

In conclusion, our study suggests that PAO is effective at increasing contact area and decreasing contact stress on the acetabular cartilage. Contact area increased the most medially, and the largest reductions in contact stress were found anteriorly and laterally. Articular congruency improved postoperatively. However, labral mechanics were largely unaltered. Future work will incorporate patient-specific kinematics and a more diverse patient population to encompass the spectrum and severity of dysplasia present. Additionally, a longer follow-up of the current study group could provide insights into factors that may predict premature failure; one hip exhibited increased contact stresses

medially following PAO which could have been caused by overcorrection. As a technically demanding procedure, we believe patient-specific FE models could be useful as a teaching tool and for surgical planning of PAO. In particular, models could optimize acetabular reorientation to normalize contact stresses while avoiding over-correction and iatrogenic impingement.

3.6 Acknowledgements

Financial support from NIH #R01 AR053344, #R01 GM083925, #R01 EB016701, and #R21 AR3466184 is gratefully acknowledged. Additional funding was received from the LS Peery Discovery Program in Musculoskeletal Restoration. Statistical analysis assistance from Greg Stoddard, MPH, is gratefully acknowledged. The project described was supported by the National Center for Research Resources and the National Center for Advancing Translational Sciences, National Institutes of Health, through Grant 8UL1TR000105 (formerly UL1RR025764). The content is solely the responsibility of the authors and does not necessarily represent the official views of the NIH.

3.7 References

1. Murphy LB, Helmick CG, Schwartz TA, et al. 2010. One in four people may develop symptomatic hip osteoarthritis in his or her lifetime. *Osteoarthritis and cartilage / OARS, Osteoarthritis Research Society* 18: 1372-1379.
2. Clohisy JC, Dobson MA, Robison JF, et al. 2011. Radiographic structural abnormalities associated with premature, natural hip-joint failure. *The Journal of bone and joint surgery American volume* 93 Suppl 2: 3-9.
3. Jacobsen S, Sonne-Holm S. 2005. Hip dysplasia: a significant risk factor for the development of hip osteoarthritis. A cross-sectional survey. *Rheumatology* 44: 211-218.
4. Nunley RM, Prather H, Hunt D, et al. 2011. Clinical presentation of symptomatic acetabular dysplasia in skeletally mature patients. *The Journal of bone and joint surgery American volume* 93 Suppl 2: 17-21.
5. Kosuge D, Yamada N, Azegami S, et al. 2013. Management of developmental dysplasia of the hip in young adults: current concepts. *The bone & joint journal* 95-B: 732-737.
6. Leunig M, Siebenrock KA, Ganz R. 2001. Rationale of periacetabular osteotomy and background work. *Instructional course lectures* 50: 229-238.
7. Russell ME, Shivanna KH, Grosland NM, et al. 2006. Cartilage contact pressure elevations in dysplastic hips: a chronic overload model. *Journal of orthopaedic surgery and research* 1: 6.
8. Domb B, LaReau J, Redmond JM. 2014. Combined hip arthroscopy and periacetabular osteotomy: indications, advantages, technique, and complications. *Arthroscopy techniques* 3: e95-e100.
9. Redmond JM, Gupta A, Stake CE, et al. 2014. The prevalence of hip labral and chondral lesions identified by method of detection during periacetabular osteotomy: arthroscopy versus arthrotomy. *Arthroscopy : the journal of arthroscopic & related surgery : official publication of the Arthroscopy Association of North America and the International Arthroscopy Association* 30: 382-388.
10. Henak CR, Abraham CL, Anderson AE, et al. 2014. Patient-specific analysis of cartilage and labrum mechanics in human hips with acetabular dysplasia. *Osteoarthritis and cartilage / OARS, Osteoarthritis Research Society* 22: 210-217.

11. Henak CR, Ellis BJ, Harris MD, et al. 2011. Role of the acetabular labrum in load support across the hip joint. *Journal of biomechanics* 44: 2201-2206.
12. Ganz R, Klaue K, Vinh TS, et al. 1988. A new periacetabular osteotomy for the treatment of hip dysplasias. Technique and preliminary results. *Clinical orthopaedics and related research*: 26-36.
13. Tibor LM, Sink EL. 2012. Periacetabular osteotomy for hip preservation. *The Orthopedic clinics of North America* 43: 343-357.
14. Hartig-Andreasen C, Troelsen A, Thillemann TM, et al. 2012. What factors predict failure 4 to 12 years after periacetabular osteotomy? *Clinical orthopaedics and related research* 470: 2978-2987.
15. Matheney T, Kim YJ, Zurakowski D, et al. 2009. Intermediate to long-term results following the Bernese periacetabular osteotomy and predictors of clinical outcome. *The Journal of bone and joint surgery American volume* 91: 2113-2123.
16. McKinley TO. 2010. The Bernese periacetabular osteotomy for treatment of adult hip dysplasia. *Skeletal radiology* 39: 1057-1059.
17. Peters CL, Erickson JA, Hines JL. 2006. Early results of the Bernese periacetabular osteotomy: the learning curve at an academic medical center. *The Journal of bone and joint surgery American volume* 88: 1920-1926.
18. Steppacher SD, Tannast M, Ganz R, et al. 2008. Mean 20-year followup of Bernese periacetabular osteotomy. *Clinical orthopaedics and related research* 466: 1633-1644.
19. Anderson AE, Ellis BJ, Maas SA, et al. 2008. Validation of finite element predictions of cartilage contact pressure in the human hip joint. *Journal of biomechanical engineering* 130: 051008.
20. Anderson AE, Ellis BJ, Maas SA, et al. 2010. Effects of idealized joint geometry on finite element predictions of cartilage contact stresses in the hip. *Journal of biomechanics* 43: 1351-1357.
21. Henak CR, Carruth ED, Anderson AE, et al. 2013. Finite element predictions of cartilage contact mechanics in hips with retroverted acetabula. *Osteoarthritis and cartilage / OARS, Osteoarthritis Research Society* 21: 1522-1529.
22. Henak CR, Kapron AL, Anderson AE, et al. 2014. Specimen-specific predictions of contact stress under physiological loading in the human hip: validation and sensitivity studies. *Biomechanics and modeling in mechanobiology* 13: 387-400.

23. Zhao X, Chosa E, Totoribe K, et al. 2010. Effect of periacetabular osteotomy for acetabular dysplasia clarified by three-dimensional finite element analysis. *Journal of orthopaedic science : official journal of the Japanese Orthopaedic Association* 15: 632-640.
24. Gu DY, Hu F, Wei JH, et al. 2011. Contributions of non-spherical hip joint cartilage surface to hip joint contact stress. *Conference proceedings : Annual International Conference of the IEEE Engineering in Medicine and Biology Society IEEE Engineering in Medicine and Biology Society Conference 2011*: 8166-8169.
25. Okano K, Yamada K, Takahashi K, et al. 2010. Joint congruency in abduction before surgery as an indication for rotational acetabular osteotomy in early hip osteoarthritis. *International orthopaedics* 34: 27-32.
26. Yasunaga Y, Takahashi K, Ochi M, et al. 2003. Rotational acetabular osteotomy in patients forty-six years of age or older: comparison with younger patients. *The Journal of bone and joint surgery American volume* 85-A: 266-272.
27. Clohisy JC, Nunley RM, Curry MC, et al. 2007. Periacetabular osteotomy for the treatment of acetabular dysplasia associated with major aspherical femoral head deformities. *The Journal of bone and joint surgery American volume* 89: 1417-1423.
28. Harris MD, Anderson AE, Henak CR, et al. 2012. Finite element prediction of cartilage contact stresses in normal human hips. *Journal of orthopaedic research : official publication of the Orthopaedic Research Society* 30: 1133-1139.
29. Bergmann G, Deuretzbacher G, Heller M, et al. 2001. Hip contact forces and gait patterns from routine activities. *Journal of biomechanics* 34: 859-871.
30. Puso MA, Maker BN, Ferencz RM, et al. 2007. NIKE3D: A Nonlinear, Implicit, Three-Dimensional Finite Element Code for Solid and Structural Mechanics. *User's Manual*.
31. Ateshian GA, Rosenwasser MP, Mow VC. 1992. Curvature characteristics and congruence of the thumb carpometacarpal joint: differences between female and male joints. *Journal of biomechanics* 25: 591-607.
32. Finner H. 1993. On a monotonicity problem in step-down multiple test procedures. *Journal of the American Statistical Association* 88: 920-923.
33. Guilak F, Fermor B, Keefe FJ, et al. 2004. The role of biomechanics and inflammation in cartilage injury and repair. *Clinical orthopaedics and related research*: 17-26.

34. Armiger RS, Armand M, Tallroth K, et al. 2009. Three-dimensional mechanical evaluation of joint contact pressure in 12 periacetabular osteotomy patients with 10-year follow-up. *Acta orthopaedica* 80: 155-161.
35. Crowninshield RD, Brand RA, Pedersen DR. 1983. A stress analysis of acetabular reconstruction in protrusio acetabuli. *The Journal of bone and joint surgery American volume* 65: 495-499.
36. Leunig M, Nho SJ, Turchetto L, et al. 2009. Protrusio acetabuli: new insights and experience with joint preservation. *Clinical orthopaedics and related research* 467: 2241-2250.
37. Jacobsen JS, Nielsen DB, Sorensen H, et al. 2013. Changes in walking and running in patients with hip dysplasia. *Acta orthopaedica* 84: 265-270.
38. Romano CL, Frigo C, Randelli G, et al. 1996. Analysis of the gait of adults who had residua of congenital dysplasia of the hip. *The Journal of bone and joint surgery American volume* 78: 1468-1479.
39. Endo H, Mitani S, Senda M, et al. 2003. Three-dimensional gait analysis of adults with hip dysplasia after rotational acetabular osteotomy. *Journal of orthopaedic science : official journal of the Japanese Orthopaedic Association* 8: 762-771.
40. Pedersen EN, Alkjaer T, Soballe K, et al. 2006. Walking pattern in 9 women with hip dysplasia 18 months after periacetabular osteotomy. *Acta orthopaedica* 77: 203-208.
41. Mow VC, Huiskes R. 2005. *Basic orthopaedic biomechanics & mechanobiology*: Lippincott Williams & Wilkins; p.
42. Petersen W, Petersen F, Tillmann B. 2003. Structure and vascularization of the acetabular labrum with regard to the pathogenesis and healing of labral lesions. *Archives of orthopaedic and trauma surgery* 123: 283-288.
43. Quapp KM, Weiss JA. 1998. Material characterization of human medial collateral ligament. *Journal of biomechanical engineering* 120: 757-763.

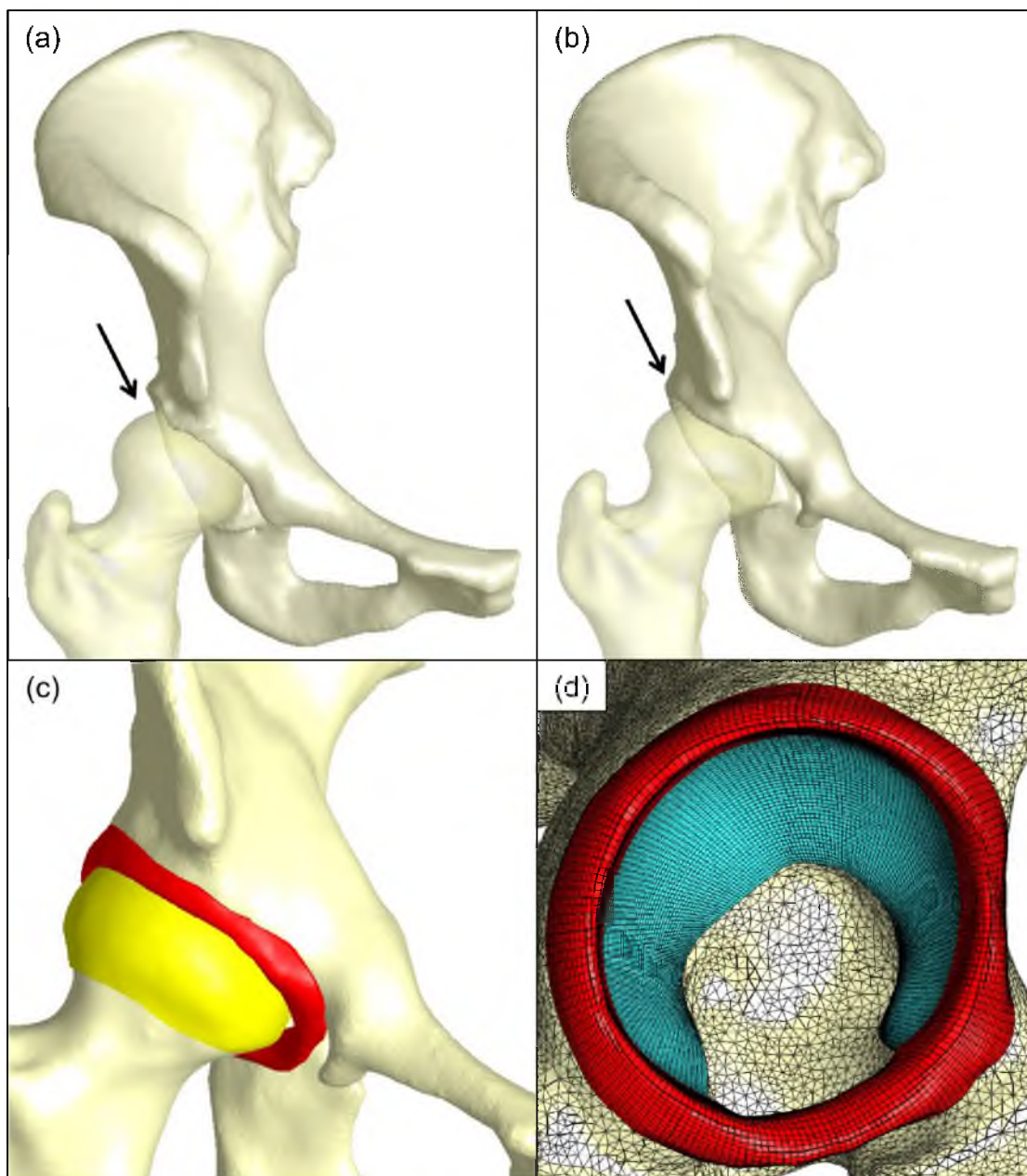


Figure 3.1. Finite element model representation for a single patient. Patient-specific 3D reconstructions of the femur and pelvis in the (a) preoperative and (b) postoperative state. The femurs are semitransparent to highlight anterolateral femoral coverage (indicated by the arrows). (c) Representative postoperative model showing bone, cartilage, and labrum. (d) Sagittal view of mesh discretization for bone (white) acetabular cartilage (blue) and labrum (red).

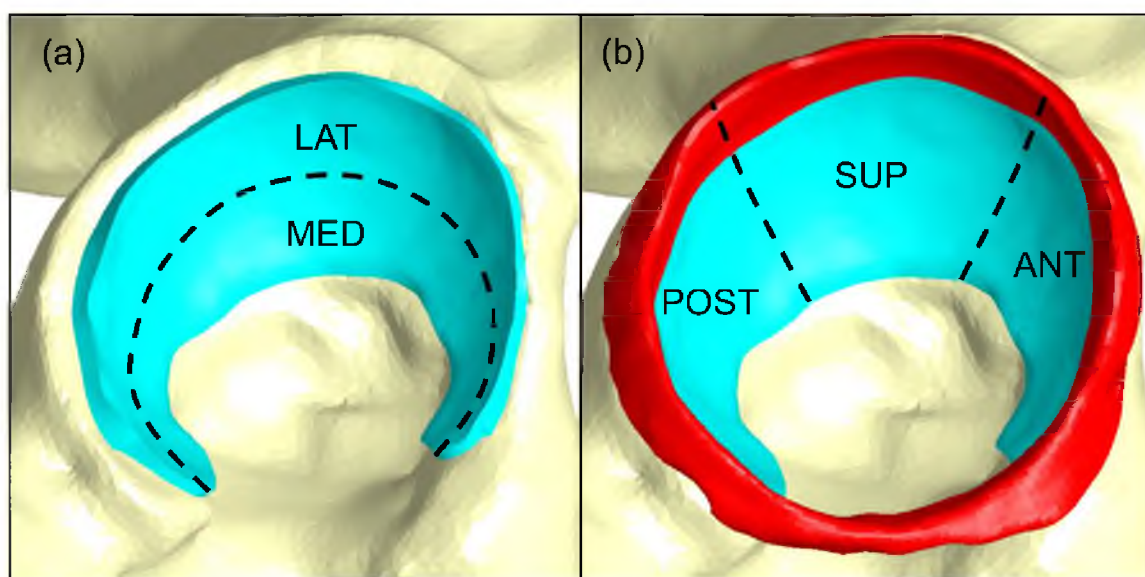


Figure 3.2. Regions of acetabular cartilage and labrum analyzed. (a) Lateral and medial regions were analyzed for acetabular cartilage. (b) A 3 region analysis partitioned acetabular cartilage and labrum into anterior, superior, and posterior regions.

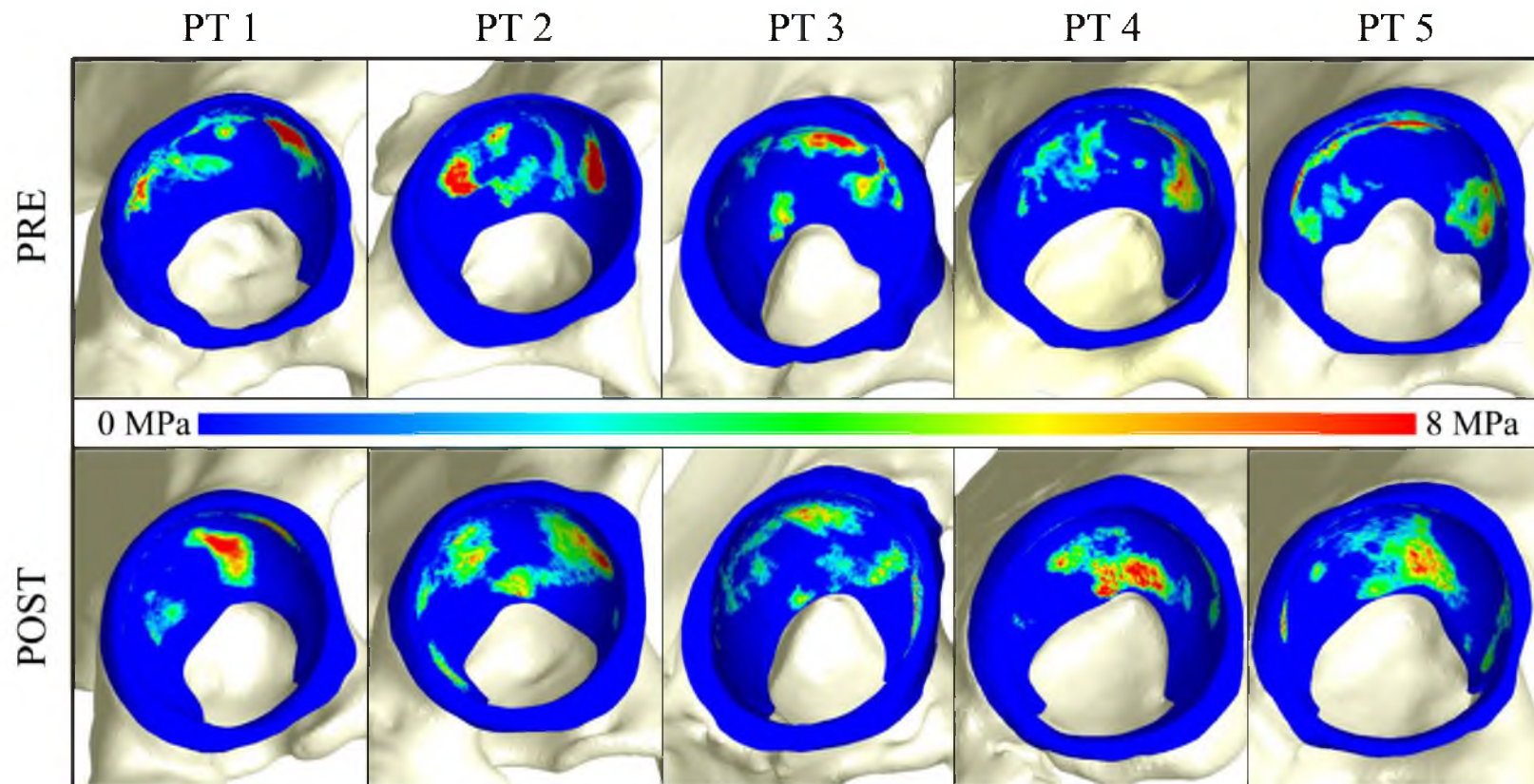


Figure 3.3. Contact stress pre- and postoperatively for walking at midstance for each patient. In general, contact was better distributed postoperatively with more stress in the medial regions. However, for one patient (PT 4), focal contact was observed on the medial portion of the acetabulum, extending to the acetabular fossa.

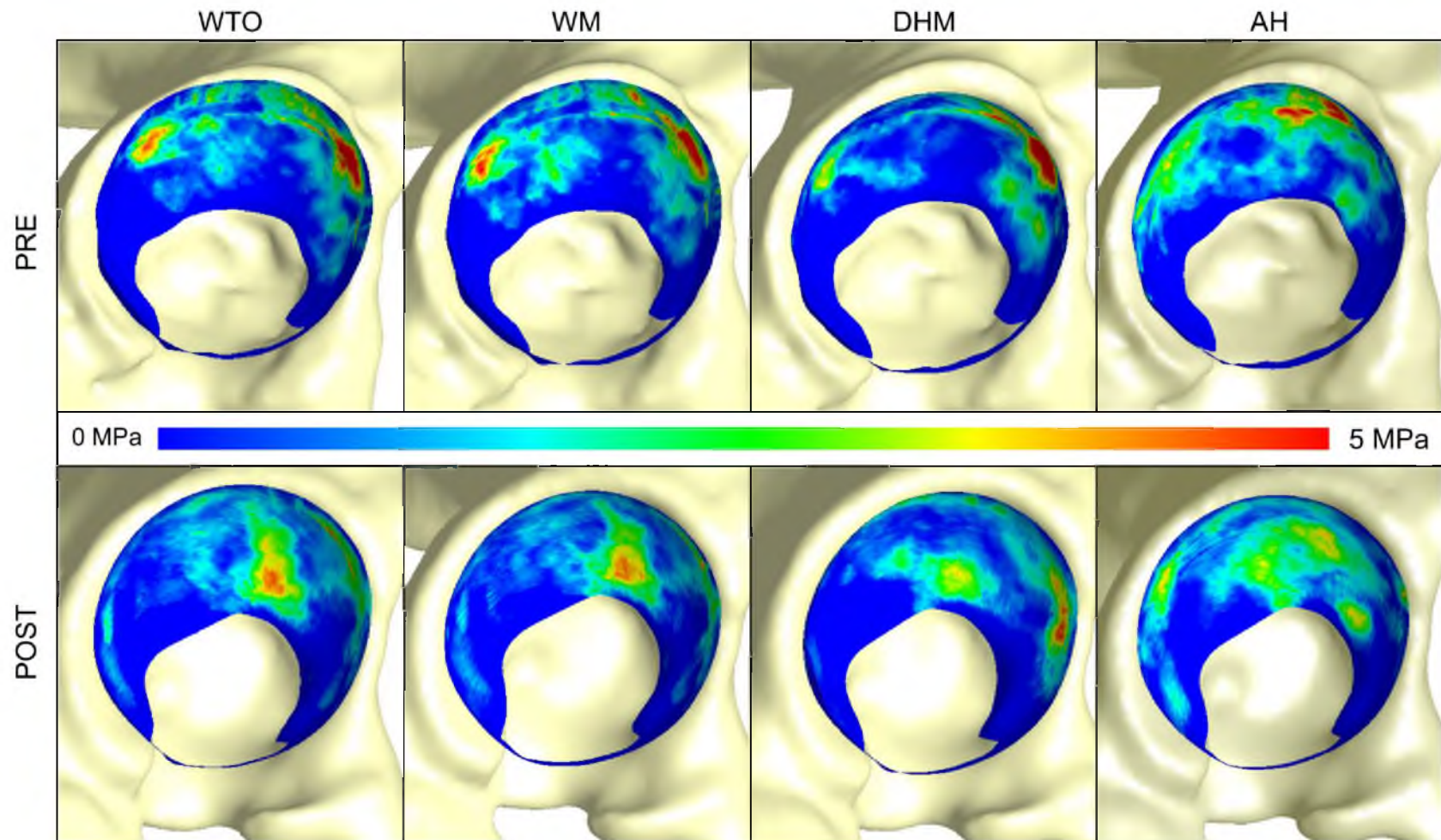


Figure 3.4. Average contact stress of all five patients pre- (top) and postoperatively (bottom) during all activities. Contact shifted medially for all patients postoperatively. Anterolateral focal loading was alleviated postoperatively. Note: contact stresses from all five subjects have been mapped to a single mesh for visualization.

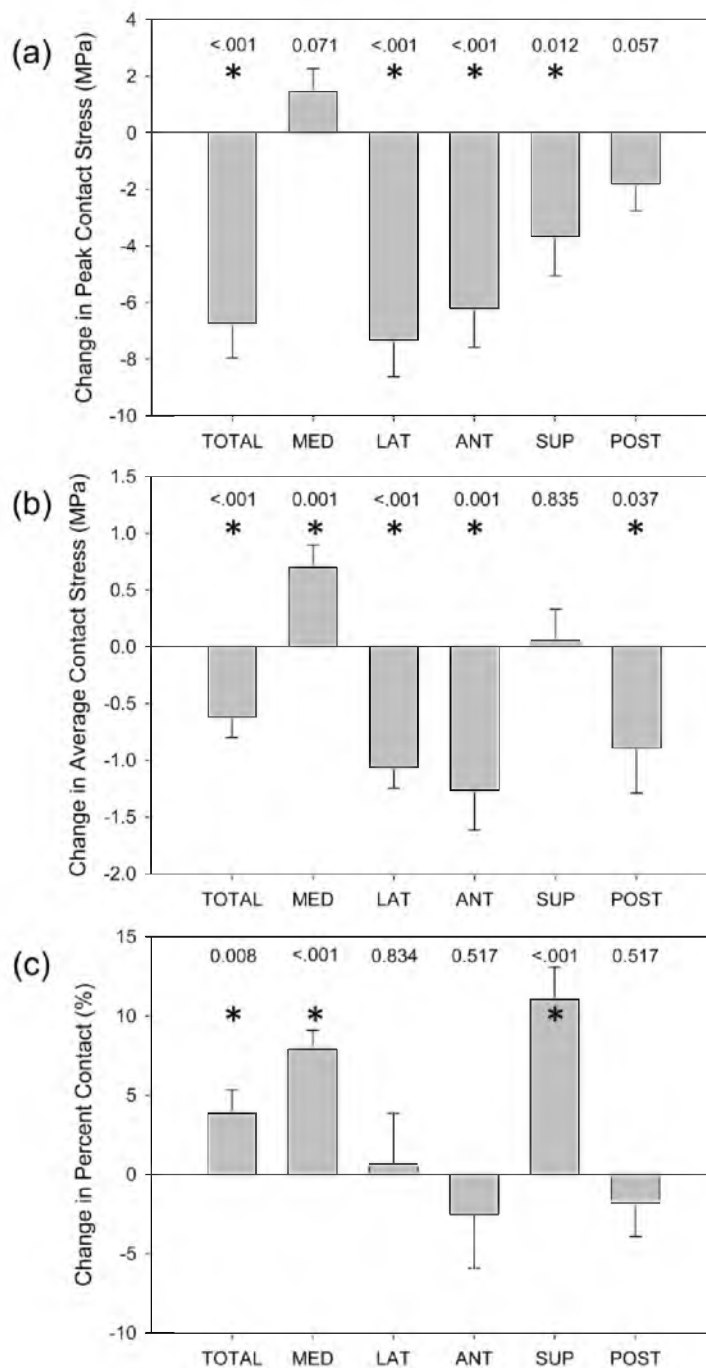


Figure 3.5. Changes in acetabular cartilage mechanics postoperatively. (a) Peak contact stress significantly decreased in lateral, anterior, and superior regions. (b) Average contact stress was significantly reduced postoperatively in lateral, anterior, and posterior regions; average contact stress increased medially. (c) Percent contact area significantly increased in medial and superior regions. Error bars indicate the standard error. P values are listed and * indicates $P \leq 0.05$ in comparison to postoperative hips.

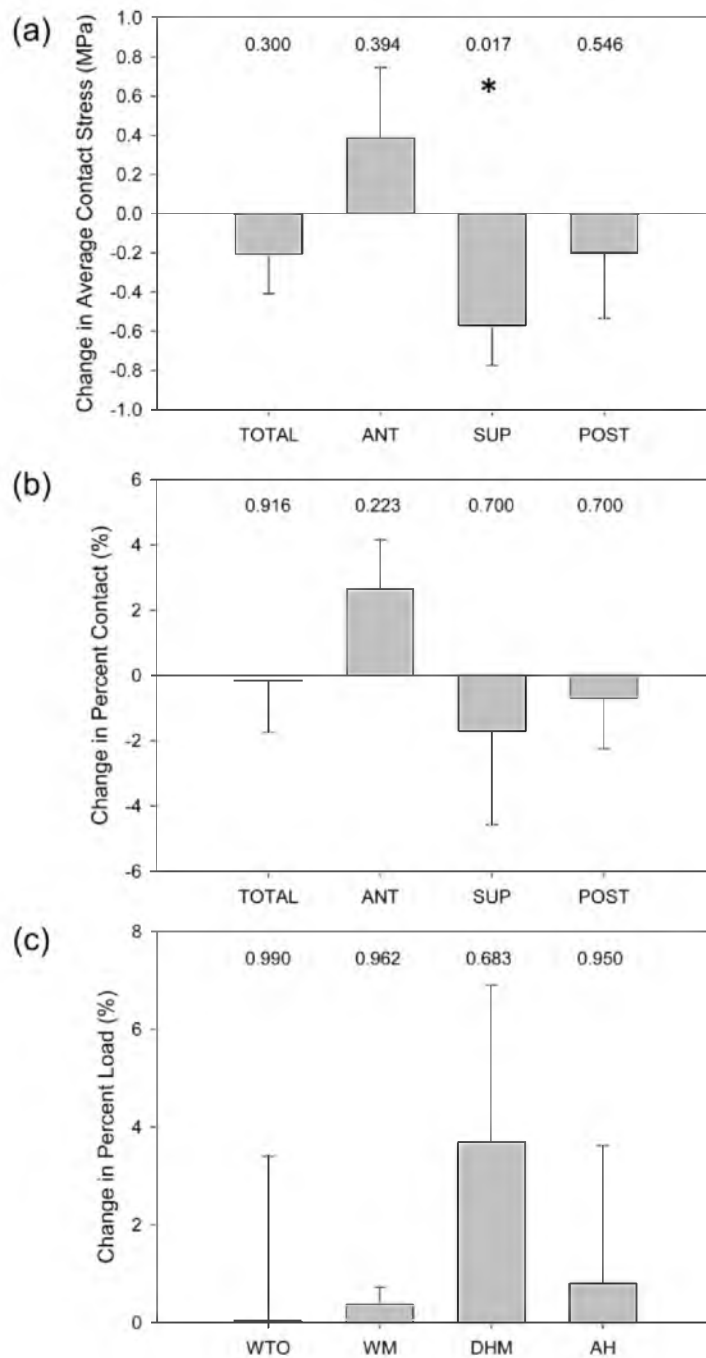


Figure 3.6. Changes in labral mechanics postoperatively. (a) Average contact stress, (b) percent contact, and (c) percent load supported by the labrum did not significantly change postoperatively. Error bars indicate the standard error. P values are listed and * indicates $P \leq 0.05$ in comparison to postoperative hips.

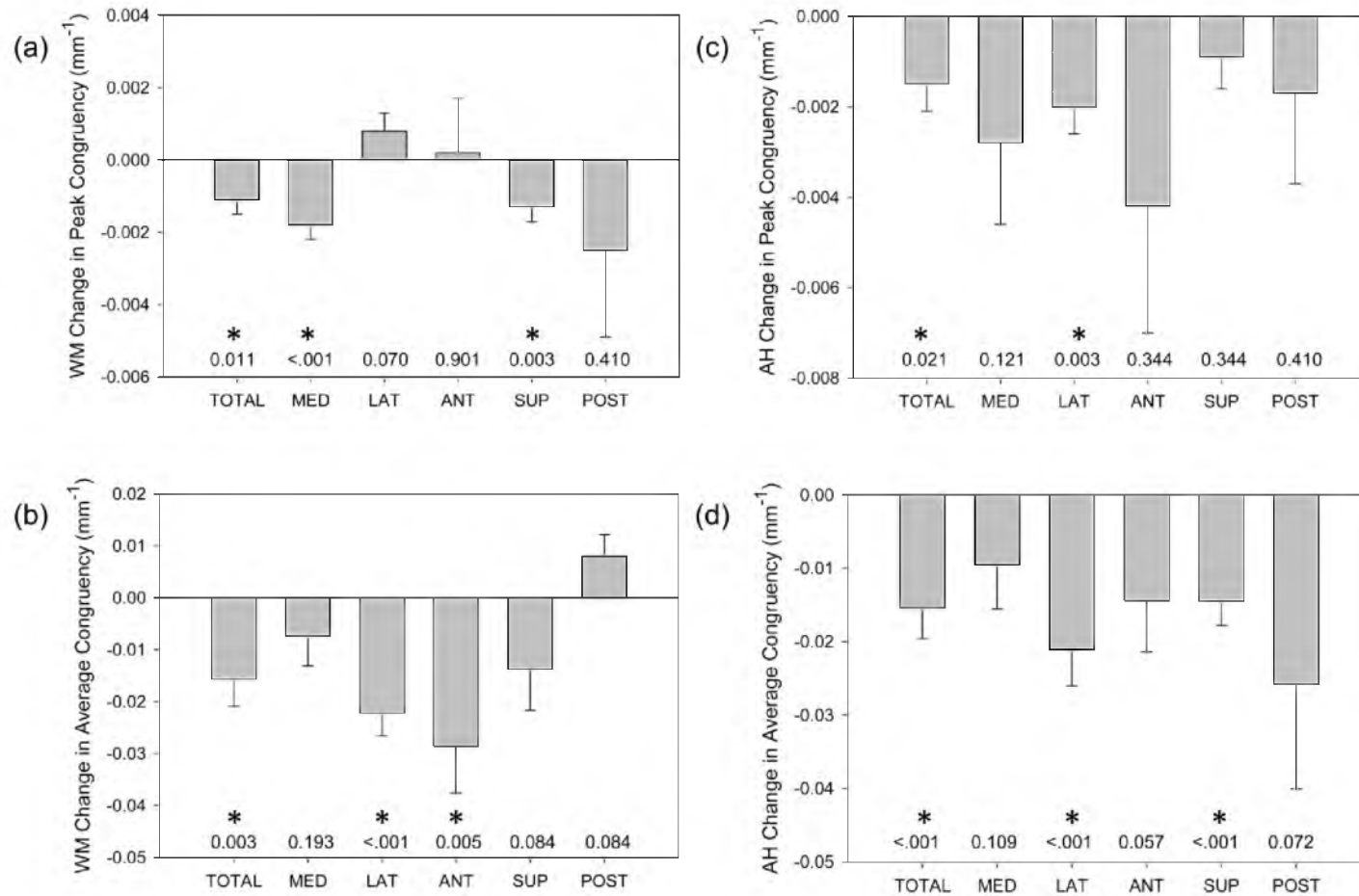


Figure 3.7. Peak congruency (most congruent point indicated by minimum RMS value) and average congruency during WM and AH overall, and by region. Most congruent point in (a) WM and (c) AH. Average congruency in (b) WM and (d) AH. Congruency was improved postoperatively in all regions for AH and all regions except for posterior in WM. Error bars indicate the standard error. P values are listed and * indicates $P \leq 0.05$ in comparison to postoperative hips.

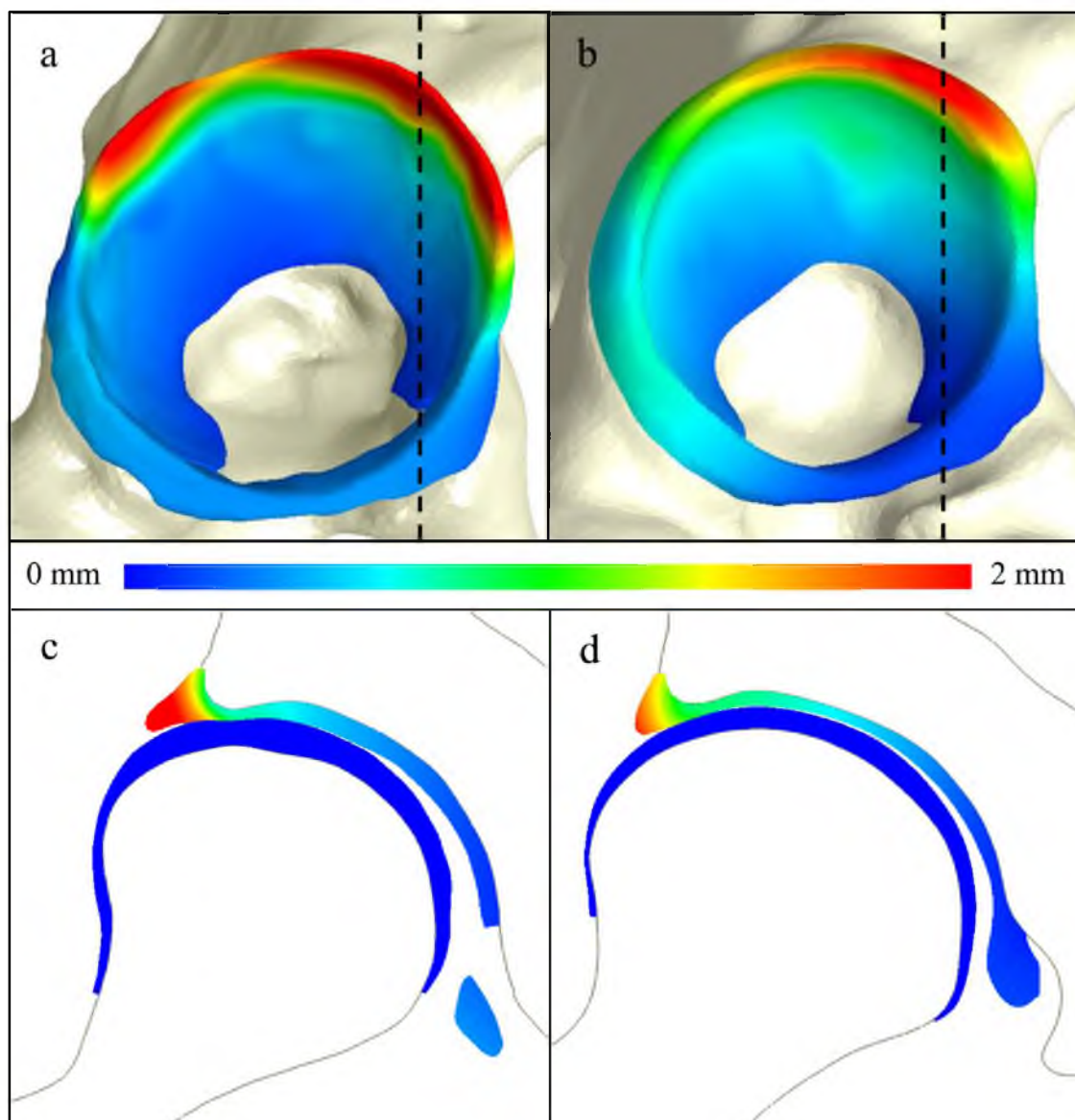


Figure 3.8. Displacement of cartilage and labrum for a representative dysplastic hip during walking at toe-off. (a) The labrum experienced larger displacements before PAO. (b) Postoperatively, displacement was more diffuse across acetabular cartilage and labrum. Dashed lines indicate the position of cross-sections. Coronal cross-section of the anterior joint (c) pre- and (d) postoperatively. The labrum is contacted and loaded (c) pre- and (d) postoperatively.

CHAPTER 4

A NEW DISCRETE ELEMENT ANALYSIS METHOD FOR PREDICTING HIP JOINT CONTACT STRESSES¹

4.1 Abstract

Quantifying cartilage contact stress is paramount to understanding hip osteoarthritis. Discrete element analysis (DEA) is a computationally efficient method to estimate cartilage contact stresses. Previous applications of DEA have underestimated cartilage stresses and yielded unrealistic contact patterns because they assumed constant cartilage thickness and/or concentric joint geometry. The study objectives were to: 1) develop a DEA model of the hip joint with subject-specific bone and cartilage geometry, 2) validate the DEA model by comparing DEA predictions to those of a validated finite element analysis (FEA) model, and 3) verify both the DEA and FEA models with a linear-elastic boundary value problem. Springs representing cartilage in the DEA model were given lengths equivalent to the sum of acetabular and femoral cartilage thickness and joint space in the FEA model. Material properties and boundary/loading conditions were equivalent. Walking, descending, and ascending stairs were simulated. Solution times for DEA and FEA models were ~7 seconds and ~65 minutes, respectively.

¹Reprinted from Journal of Biomechanics, 46(6), Abraham CL, Maas SA, Weiss JA, Ellis BJ, Peters CL, Anderson AE, A New Discrete Element Analysis Method for Predicting Hip Joint Contact Stresses, 1121-7, 2013, with permission from Elsevier.

Irregular, complex contact patterns predicted by DEA were in excellent agreement with FEA. DEA contact areas were 7.5%, 9.7%, and 3.7% less than FEA for walking, descending stairs, and ascending stairs, respectively. DEA models predicted higher peak contact stresses (9.8-13.6 MPa) and average contact stresses (3.0-3.7 MPa) than FEA (6.2-9.8 and 2.0-2.5 MPa, respectively). DEA overestimated stresses due to the absence of the Poisson's effect and a direct contact interface between cartilage layers. Nevertheless, DEA predicted realistic contact patterns when subject-specific bone geometry and cartilage thickness were used. This DEA method may have application as an alternative to FEA for preoperative planning of joint-preserving surgery such as acetabular reorientation during peri-acetabular osteotomy.

4.2 Introduction

Chronic exposure of elevated cartilage contact stresses has been shown to predict the onset and progression of osteoarthritis (OA) in the hip²⁴³⁻²⁴⁵. Thus, methods to quantify hip joint cartilage contact stresses are clinically relevant and necessary to improve our understanding of hip OA. For example, the magnitude and distribution of cartilage contact stress could be used to quantify mechanical differences between normal and pathologic hips, generate preoperative surgical plans, and predict long-term prognosis following surgical treatment. However, direct measurement of cartilage contact stresses and contact area in-vivo is currently not possible.

Computational modeling is an alternative to direct in-vivo measurement of cartilage contact stresses. Both finite element analysis (FEA)^{153,246-250} and discrete element analysis (DEA)^{95,135,251-253} have been used to estimate hip cartilage contact

stresses. FEA models of the hip can predict cartilage contact stresses consistent with experimental data when subject-specific bone and cartilage geometry are used and bones are modeled as deformable^{250,254}. However, the construction and analysis of FEA models are time-intensive and computationally expensive. Thus, many published FEA models simplify the complex geometry of the hip joint by assuming spherical geometry^{247,249} or constant cartilage thickness¹⁵³. Models that assume ideal geometry underestimate peak cartilage contact stresses by 60%, average cartilage contact stresses by 21%, and overestimate contact area by 25%²⁵⁵.

DEA (i.e. rigid body spring method) is a computationally efficient method for calculating cartilage stresses. Using DEA, bones are modeled as rigid bodies and cartilage is represented as an array of springs^{135,138,256}. Cartilage contact stress is quantified based on spring deformation. Previous DEA models have assumed concentric hip joint geometry and constant cartilage thickness^{155,251,253,257} or cartilage thickness equal to the distance between the acetabulum and femoral head²⁵². These assumptions for DEA underestimate cartilage stress and predict unrealistic, simplified contact patterns^{95,155,251,253} when compared to experimentally measured contact stress magnitudes and complex contact patterns^{124,128,258}. However, it is possible that DEA could provide realistic predictions of hip cartilage contact stress if subject-specific bone and cartilage thickness were incorporated. The study objectives were to: 1) develop a DEA model of the hip joint with subject-specific bone and cartilage geometry, 2) validate the DEA model by comparing DEA predictions to those of a validated FEA model, and 3) verify both the DEA and FEA models with a linear-elastic boundary value problem.

4.3 Methods

High-resolution CT image data (512×512, 320 mm field of view, in-plane resolution 0.625×0.625 mm, 0.6 mm slice thickness) of a 25-year-old male cadaveric hip provided baseline geometry (cortical bone and cartilage surfaces) for both the DEA and previously validated subject-specific FEA model²⁵⁴.

4.3.1 Discrete Element Analysis Implementation

A custom C++ program was written to perform DEA. A Newton solver was used to determine the position of the femur such that the sum of the spring forces balanced the applied force. As the DEA method requires rigid bones, both the pelvis and femur were modeled as rigid, triangulated surfaces with position-dependent cartilage thickness values assigned to each node. Nodal cartilage thicknesses were computed as the distance between cartilage and cortical bone surfaces projected along the surface normal vector. Cartilage was represented by a distribution of compressive springs generated in the region of the femoral head underlying the acetabulum in each loading scenario. One end of the spring was attached at the center of each triangle on the acetabulum and the other was determined by projecting the point along the acetabular surface normal onto the femoral head. The initial spring length was calculated as a distance between starting and projection points, and was defined as the sum of acetabular and femoral cartilage thickness and gap distance at the corresponding location of the FEA model (Fig. 4.1). Since the spring attachment at the femur did not necessarily terminate directly at a femur surface node, femoral cartilage thicknesses were interpolated from neighboring nodes. The springs resisted compressive forces (spring length less than the sum of acetabular

and femoral cartilage thickness) but not tensile forces (Fig. 4.1). The force generated by compression of an individual spring was calculated according to Hooke's law:

$$\mathbf{f}_i = k_i d_i \Delta x_i \mathbf{n}_i, \quad (4.1)$$

where Δx_i is the spring compression distance, k_i is spring stiffness, and \mathbf{n}_i is the local surface normal. The spring stiffness k_i depended on Young's modulus and Poisson's ratio ($E = 11.85$ MPa, $\nu = 0.45$)^{251,253}:

$$k_i = \frac{E(1-\nu)A_i}{(1-2\nu)(1+\nu)h_i}, \quad (4.2)$$

Here, A_i is a triangular element area and h_i is the sum of acetabular and femoral cartilage thicknesses. The spring forces (Eq. (4.1)) that balance the applied force are a nonlinear function of femur position. Newton's method determined the position of the femur so that spring forces balanced the applied force. The initial condition was the initial position of the femur and pelvis, positioned according to in-vivo kinematic data²⁵⁹. Newton's method was used to calculate the root of the residual function, defined as the difference between the user input force and the sum of the spring forces. The updated position of the femur was calculated at each Newton-iteration and projection points of springs on the femoral head were regenerated following each update to account for the new position of the femur. To maintain the appropriate kinematic position, rotation of the femur was restricted, and therefore, moments were not balanced. Contact stresses were calculated

from the spring force and triangular element area where each spring was attached. A convergence study determined the number of springs necessary.

4.3.2 Finite Element Analysis

Triangular shell elements defined bone geometry²⁵⁴, and were assumed rigid to correspond with DEA model assumption. Cartilage was represented using hexahedral elements as a neo-Hookean hyperelastic material, and the shear modulus, G , and bulk modulus, K , were assigned based on the Young's modulus E and Poisson's ratio ν used in the DEA analysis:

$$G = \frac{E}{2(1+\nu)} \quad (4.3)$$

$$K = \frac{E}{3(1-2\nu)} \quad (4.4)$$

FEA models were analyzed using NIKE3D²⁶⁰.

4.3.3 Loading and Boundary Conditions

The pelvis was assumed rigid and fixed in space. The femoral head was modeled as rigid but free to translate in all three axes (rotations constrained). Loading conditions and geometric orientation of the femur relative to the pelvis were based on published data for in-vivo hip loads²⁵⁹. Walking (W), descending stairs (DS), and ascending stairs (AS) for the average subject in²⁵⁹ were analyzed; 800 N bodyweight was assumed. Force was

applied to the geometric center of the femoral head, determined as the center of a sphere fit to the femoral head using a least squares optimization.

4.3.4 Data Analysis

To facilitate DEA and FEA comparisons, DEA nodal results (defined on triangulated bone surfaces) were projected onto the articulating (quadrilateral) surface of the FEA cartilage mesh and interpolated. Interpolation was accomplished by locating the closest point projection of each quadrilateral node onto the triangular bone surface. The value at the projection point was interpolated from nodal values using element shape functions. Predictions of peak contact stress, average contact stress, and contact area were compared descriptively between DEA and FEA to validate the DEA model, where validation was the process of ensuring that a computational model accurately represents the physics of the real-world system^{261,262}. Cartilage contact stress was sampled on the surface of the acetabular cartilage, and average contact stress was calculated for each loading scenario considering all articulating nodes in contact (i.e. nodes with a positive contact stress). Cartilage contact area was calculated by summing the surface area of each element in the acetabular cartilage that was in contact with the femoral cartilage. The acetabular cartilage was divided into anterior, superior, and posterior regions, where each region contained an equivalent number of elements²⁶³. Both DEA and FEA models were preprocessed using PreView and postprocessed using PostView (www.febio.org).

4.3.5 Model Verification

A linear-elastic boundary value problem (Fig. 4.2) served as verification of the DEA and FEA models, where verification was defined as determining that a computational model accurately represents the underlying mathematical model and its solution^{261,262,264}. Specifically, contact stress predictions were compared to the simplified elasticity solution of an elastic sphere supported bilaterally by concentric rigid spheres^{256,265}. The model dimensions, constitutive models, and loading conditions were comparable to physiologic hip models. Rigid hemispheres radii were 20 and 24 mm, and the elastic sphere conformed to the rigid backings and was 4 mm thick, similar to the thickness of two cartilage layers²⁶⁶⁻²⁶⁸. The simplified elasticity solution described displacement as the differential equations of equilibrium in spherical coordinates and assumed displacement was confined to the radial direction²⁶⁵.

To model the equivalent using FEA, 4 mm thick cartilage was represented with hexahedral elements as a single layer (10 through the thickness, total of 108,000 elements). The outer surface cartilage nodes were fixed and the smaller rigid sphere was represented by hexahedral elements (2 elements through thickness, total of 21,600 elements). Cartilage was a neo-Hookean, hyperelastic material ($E = 11.85$ MPa, $\nu = 0.45$, EQ 3,4) and a frictionless sliding interface was defined between the smaller rigid hemisphere and cartilage layer. An additional FEA model was generated with a frictionless sliding interface between two cartilage layers. Here, cartilage was modeled as two separate materials using hexahedral elements (2 mm thickness each, 5 elements through thickness, total of 54,000 elements for each cartilage layer). Cartilage layers

were tied to rigid bone backings. All FEA models utilized quarter symmetry and were analyzed in NIKE3D²⁶⁰.

A DEA simulation was analyzed with rigid hemispheres ($r = 20$ mm, 24 mm) and constant cartilage thickness of 4 mm. Spring stiffness was determined following material properties equivalent to the analytical solution and FEA ($E = 11.85$ MPa, $\nu = 0.45$). A convergence study determined the number of springs required. A range of forces (100 N – 4000 N) was applied through the smaller rigid hemisphere to compare predictions across loads in both FEA and DEA models.

4.4 Results

4.4.1 Contact Area

DEA and FEA contact patterns corresponded well and predicted irregular, complex contact for all three loading scenarios (Fig. 4.3). For walking and descending stairs, both methods predicted contact predominantly in the superolateral region. For ascending stairs, contact was predicted posteriorly (Fig. 4.3). DEA contact areas were 7.5%, 9.7%, and 3.7% less than FEA contact areas for walking, descending stairs, and ascending stairs, respectively (Fig. 4.4). Regional contact areas (anterior, superior, posterior) were consistently reduced in DEA compared with FEA and averaged 71.1 ± 16.7 , 85.8 ± 16.7 , and 26.4 ± 1.5 mm² less than FEA in walking, descending stairs, and ascending stairs, respectively.

4.4.2 Contact Stress

DEA contact stress distributions were similar to FEA, but DEA predictions exhibited greater variation, especially at higher magnitudes of contact stress (Fig. 4.5). Mean and median contact stresses averaged 43% and 44% higher in DEA, respectively. Peak contact stresses for DEA and FEA ranged from 9.8-13.6 and 6.2-9.8 MPa, respectively. Average contact stresses for DEA and FEA ranged from 3.0-3.7 and 2.0-2.5 MPa, respectively.

4.4.3 Verification Results

At a force of 2000 N, DEA and FEA models that analyzed a single layer of cartilage predicted peak contact stress 0.42% and 2.11% higher than the analytical solution, respectively (Fig. 4.6). Contact stress predicted by the FEA model with two layers of cartilage was reduced compared with the analytical solution and FEA model that analyzed a single layer of cartilage. The difference in contact stresses was largest at the location of maximum stress ($\theta = 0$), where DEA predicted a contact stress 18.5% greater than the 2 layer FEA model. The mean and median contact stresses were 17.1% and 15.7% higher in DEA than the 2 layer FEA model. Results were consistent over forces varying from 100 – 4000 N, a range that encompasses loads experienced *in vivo*²⁵⁹.

4.4.4 Convergence and Computation Time

The DEA convergence study demonstrated that ~20,000 and ~5,000 springs were required to achieve <5% change in average/peak contact stress and contact area upon

further refinement in the subject-specific hip models and spherical verification model, respectively. The solution time for each DEA model was ~7 seconds (IBM ThinkPad Intel Core 2 Duo cpu @2.80 GHz, 3 GB RAM). FEA models required an average solution time of ~65 minutes on a computing cluster (SUN FIRE X2270 2 cpu / 8 core Intel Xeon X5550 @ 2.67GHz (16 cores with HT) 48GB of RAM 1GB network interface).

4.5 Discussion

The results of this study demonstrated that when subject-specific bone and cartilage geometry are included in DEA, cartilage contact stress distributions in the hip are consistent with a validated FEA model. Furthermore, DEA was able to provide general trends for contact stress magnitudes and yield information about cartilage contact stress profiles. However, we found that DEA could not reliably predict the true magnitude of contact stress at specific locations in the hip joint. Despite this limitation, DEA could be a useful tool for comparative studies (normal vs. pathologic or pre- vs. postop), where the difference between groups, rather than the true magnitude of contact stress, is of primary interest. DEA could also be useful for applications where contact area or contact stress profiles are important (preoperative planning or intra-operative surgical tools).

The average increase of 43% and 44% in mean and median cartilage contact stresses (Fig. 4.5) in DEA compared to FEA may be partially explained by differences in the model representations. While FEA models have two deformable cartilage parts in contact, DEA represents cartilage as a single part, where one spring is attached to bone

on each end. The reduction in contact stresses when two deformable cartilage surfaces contact (i.e. FEA) compared to springs compressed by rigid materials on either side (i.e. DEA) was demonstrated in the verification problem, where the difference in cartilage representation and contact definition resulted in ~16% reduction in average and median contact stresses in a perfectly concentric model (Fig. 4.6). Although this does not account for the magnitude of difference in the hip model (~44%), the incongruity in the hip model likely exacerbates any differences due to representations of cartilage and the contact interface. Although the femoral head was free to translate in all directions, the DEA models did not model deformation in the lateral direction of cartilage, and Poisson's Effect was effectively ignored. Therefore, in this way, the true deformation of cartilage is not modeled in DEA. Conversely, FEA models can model the lateral response of cartilage under compression, which effectively reduces contact stresses compared to DEA.

Overall, the contact stress distributions corresponded well between DEA and FEA. This is due to two factors. First, the initial positions of bone and cartilage were identical in FEA and DEA. Second, subject-specific cartilage thickness was accounted for in DEA by assigning spring lengths equivalent to cartilage thickness, based directly on the FEA model. Therefore, despite differences in contact stress magnitudes, DEA predicted contact stress distributions that corresponded very well with FEA. In fact, contact areas were within an average of 7% of FEA. One explanation for this small difference in contact area is as follows: For the FEA model, the total area available for cartilage contact was simply the area of the cartilage-cartilage contact interface. However, in the DEA models, a true cartilage-cartilage contact interface did not exist

since a single spring represented both layers of cartilage. For DEA, the total available contact area was the area of the acetabular cartilage-bone interface in the FEA model (the acetabular cortical bone served as the spring origin). Regardless, the difference in available contact area between DEA and FEA was only 15%. Thus, it is the kinematic position and contact interface geometry (i.e. cartilage thickness) that primarily dictates the contact stress distribution and area; differences in the approach utilized to model cartilage deformation and manner in which contact area is calculated is less important.

The magnitude of the difference in contact stress and area between FEA and DEA varied with respect to the loading scenario analyzed. For example, in the ascending stairs scenario, DEA cartilage contact stresses were ~20% higher, compared to the ~40% DEA versus FEA difference in the descending stairs and walking models. The differences in DEA-FEA agreement among the loading scenarios likely resulted from the inability of DEA to model the Poisson's Effect. This becomes apparent in scenarios such as descending stairs and walking where contact stresses had a high concentration of contact stresses in the posteroinferior region of the acetabular cartilage (Fig. 4.3). In contrast, in the ascending stairs scenario, there was no contact in that region and thus less bias towards higher stress magnitudes overall.

The complex spatial distribution of contact stress and the magnitude of stresses predicted in our study are in contrast with the results of previously reported DEA models of the hip. Specifically, contact stress patterns in our study did not follow the typical unicentric, equally-distributed contact patterns seen in previously published DEA studies. Most prior studies used 2D radiographic measures to define geometry of the bone and cartilage and assumed a spherical articulating surface^{155,251,253,257}. A few studies have

improved the implementation of DEA by using CT data to model the cartilage-bone interfaces^{95,252}. However, CT images did not visualize cartilage. Thus, the articulating surface was assumed to be spherical⁹⁵ or represented by cartilage thickness equal to the joint space²⁵². The hip joint is not perfectly spherical²⁶⁷⁻²⁶⁹ and cartilage thickness varies throughout the joint^{10,269}. Accordingly, FEA and DEA models that simplify the cartilage contact interface can be expected to underestimate cartilage contact stresses and overestimate contact area^{153,255}. To obtain cartilage contact stress predictions that are consistent with in-vitro studies^{124,254,258}, it is necessary to include subject-specific bone geometry and cartilage thickness in computational models of the hip.

There are a number of limitations that deserve discussion. The first is the assumption that bones are rigid. This is a limitation that is inherent in the DEA method. In an FEA model, it has been previously shown that the rigid bone assumption increases predicted cartilage contact stresses²⁵⁵. However, in the present study, rigid bones were assumed for both FEA and DEA; error as a result of this assumption would be consistent between modeling approaches. Another inherent limitation of the DEA method is the representation of two layers of cartilage as a single spring. This simplified representation of cartilage in DEA limits results to a single force value for each spring, and therefore predicts a single value of stress throughout the cartilage thickness, which will be higher than FEA models that represent cartilage with two parts in contact. The difference in model representations of cartilage contact complicates the method by which results were compared between DEA and FEA. In DEA studies, stresses would typically be calculated at the bone surface where springs are attached. Since the cartilage geometry is often unknown, and there is no cartilage surface or mesh available, calculating stress at

the bone interface is usually the only option. In our study, contact stress was determined at the articulating cartilage surface since the cartilage surface geometry was available from the FEA model. In contrast, FEA models predict stresses throughout the cartilage thickness and are not limited to the primary result of a force value through the thickness of cartilage. Another potential limitation in our study is the difference in material models between DEA and FEA. In our study, the DEA model employed a linear-elastic spring model whereas the FEA model represented cartilage materials as neo-Hookean. Cartilage was not modeled as linear in FEA because it is not rotationally invariant (spurious strains are induced by rigid body rotations) and would therefore provide an inaccurate solution. This is not a problem with DEA because it models spring deformation as a one-dimensional strain problem. Thus, although material models are not consistent between modeling methods, the authors believe the use of a Neo-Hookean cartilage material in FEA and linear elasticity for DEA was warranted. Finally, model predictions and potential extensions of this work should be interpreted with caution considering the limited number of simulations that were performed on a single cadaveric hip.

To our knowledge, this is the first implementation of a subject-specific DEA model of the hip. When subject-specific bone geometry and cartilage thickness were included in the DEA model, realistic contact stress patterns were predicted. Although advanced imaging, such as CT or MR arthrography, may not be available to create subject-specific reconstructions of the hip that include detailed bone geometry and cartilage thickness, it is important to recognize that DEA models using simplified contact interface geometry will underestimate cartilage contact stresses, overestimate contact areas, and predict unrealistic cartilage contact stress patterns.

Assuming detailed information is available for bone and cartilage, the new DEA algorithm presented herein offers a computationally efficient alternative to FEA modeling for the prediction of contact stresses. Considering the differences in contact area predictions were small, DEA may be utilized in modeling studies where the contact area and distribution of cartilage contact stresses, and not the absolute magnitude of contact stress, is of primary importance. In particular, DEA may be clinically useful for applications that require a large number of simulations or where time is limited. For example, our DEA modeling approach could be used to generate preoperative plans, based on an optimization routine to minimize cartilage contact stress, or for intra-operative feedback systems in the treatment of hip pathologies such as dysplasia or femoroacetabular impingement.

4.6 Acknowledgements

Financial support from NIH R01AR053344 and R01GM083925 is gratefully acknowledged.

4.7 References

1. Harris WH. 1986. Etiology of osteoarthritis of the hip. *Clinical orthopaedics and related research*: 20-33.
2. Mavcic B, Igljic A, Kralj-Igljic V, et al. 2008. Cumulative hip contact stress predicts osteoarthritis in DDH. *Clin Orthop Relat Res* 466: 884-891.
3. Maxian TA, Brown TD, Weinstein SL. 1995. Chronic stress tolerance levels for human articular cartilage: two nonuniform contact models applied to long-term follow-up of CDH. *J Biomech* 28: 159-166.
4. Anderson AE, Peters CL, Tuttle BD, et al. 2005. Subject-specific finite element model of the pelvis: development, validation and sensitivity studies. *J Biomech Eng* 127: 364-373.
5. Bachtar F, Chen X, Hisada T. 2006. Finite element contact analysis of the hip joint. *Medical & biological engineering & computing* 44: 643-651.
6. Brown TD, DiGioia AM, 3rd. 1984. A contact-coupled finite element analysis of the natural adult hip. *J Biomech* 17: 437-448.
7. Chegini S, Beck M, Ferguson SJ. 2009. The effects of impingement and dysplasia on stress distributions in the hip joint during sitting and walking: a finite element analysis. *J Orthop Res* 27: 195-201.
8. Henak CR, Ellis BJ, Harris MD, et al. 2011. Role of the acetabular labrum in load support across the hip joint. *J Biomech* 44: 2201-2206.
9. Gu DY, Hu F, Wei JH, et al. 2011. Contributions of non-spherical hip joint cartilage surface to hip joint contact stress. *Conference proceedings : Annual International Conference of the IEEE Engineering in Medicine and Biology Society IEEE Engineering in Medicine and Biology Society Conference 2011*: 8166-8169.
10. Armiger RS, Armand M, Tallroth K, et al. 2009. Three-dimensional mechanical evaluation of joint contact pressure in 12 periacetabular osteotomy patients with 10-year follow-up. *Acta Orthop* 80: 155-161.
11. Chao EY, Volokh KY, Yoshida H, et al. 2010. Discrete element analysis in musculoskeletal biomechanics. *Molecular & cellular biomechanics : MCB* 7: 175-192.

12. Genda E, Iwasaki N, Li G, et al. 2001. Normal hip joint contact pressure distribution in single-leg standing--effect of gender and anatomic parameters. *J Biomech* 34: 895-905.
13. Tsumura H, Kaku N, Ikeda S, et al. 2005. A computer simulation of rotational acetabular osteotomy for dysplastic hip joint: does the optimal transposition of the acetabular fragment exist? *J Orthop Sci* 10: 145-151.
14. Yoshida H, Faust A, Wilckens J, et al. 2006. Three-dimensional dynamic hip contact area and pressure distribution during activities of daily living. *J Biomech* 39: 1996-2004.
15. Anderson AE, Ellis BJ, Maas SA, et al. 2008. Validation of finite element predictions of cartilage contact pressure in the human hip joint. *J Biomech Eng* 130: 051008.
16. Anderson AE, Ellis BJ, Maas SA, et al. 2010. Effects of idealized joint geometry on finite element predictions of cartilage contact stresses in the hip. *J Biomech* 43: 1351-1357.
17. Li G, Sakamoto M, Chao EY. 1997. A comparison of different methods in predicting static pressure distribution in articulating joints. *J Biomech* 30: 635-638.
18. Volokh KY, Chao EY, Armand M. 2007. On foundations of discrete element analysis of contact in diarthrodial joints. *Molecular & cellular biomechanics : MCB* 4: 67-73.
19. Armand M, Lepisto J, Tallroth K, et al. 2005. Outcome of periacetabular osteotomy: joint contact pressure calculation using standing AP radiographs, 12 patients followed for average 2 years. *Acta orthopaedica* 76: 303-313.
20. Genda E, Konishi N, Hasegawa Y, et al. 1995. A computer simulation study of normal and abnormal hip joint contact pressure. *Arch Orthop Trauma Surg* 114: 202-206.
21. Afoke NY, Byers PD, Hutton WC. 1987. Contact pressures in the human hip joint. *The Journal of bone and joint surgery British volume* 69: 536-541.
22. Brown TD, Shaw DT. 1983. In vitro contact stress distributions in the natural human hip. *J Biomech* 16: 373-384.
23. von Eisenhart R, Adam C, Steinlechner M, et al. 1999. Quantitative determination of joint incongruity and pressure distribution during simulated gait and cartilage

- thickness in the human hip joint. *Journal of orthopaedic research : official publication of the Orthopaedic Research Society* 17: 532-539.
24. Bergmann G, Deuretzbacher G, Heller M, et al. 2001. Hip contact forces and gait patterns from routine activities. *J Biomech* 34: 859-871.
 25. Puso MA, Maker BN, Ferencz RM, et al. 2007. NIKE3D: A Nonlinear, Implicit, Three-Dimensional Finite Element Code for Solid and Structural Mechanics. User's Manual.
 26. Henninger HB, Reese SP, Anderson AE, et al. 2010. Validation of computational models in biomechanics. *Proceedings of the Institution of Mechanical Engineers Part H, Journal of engineering in medicine* 224: 801-812.
 27. Anderson AE, Ellis BJ, Weiss JA. 2007. Verification, validation and sensitivity studies in computational biomechanics. *Computer methods in biomechanics and biomedical engineering* 10: 171-184.
 28. Athanasiou KA, Agarwal A, Dzida FJ. 1994. Comparative study of the intrinsic mechanical properties of the human acetabular and femoral head cartilage. *Journal of orthopaedic research : official publication of the Orthopaedic Research Society* 12: 340-349.
 29. 2006. *Guide for verification and validation in computational solid dynamics*.; p.
 30. Bartel DL, Burstein AH, Toda MD, et al. 1985. The effect of conformity and plastic thickness on contact stresses in metal-backed plastic implants. *J Biomech Eng* 107: 193-199.
 31. Macirowski T, Tepic S, Mann RW. 1994. Cartilage stresses in the human hip joint. *J Biomech Eng* 116: 10-18.
 32. Menschik F. 1997. The hip joint as a conchoid shape. *J Biomech* 30: 971-973.
 33. Kohnlein W, Ganz R, Impellizzeri FM, et al. 2009. Acetabular morphology: implications for joint-preserving surgery. *Clinical orthopaedics and related research* 467: 682-691.
 34. Eckstein F, von Eisenhart-Rothe R, Landgraf J, et al. 1997. Quantitative analysis of incongruity, contact areas and cartilage thickness in the human hip joint. *Acta anatomica* 158: 192-204.
 35. Shepherd DE, Seedhom BB. 1999. Thickness of human articular cartilage in joints of the lower limb. *Annals of the rheumatic diseases* 58: 27-34.

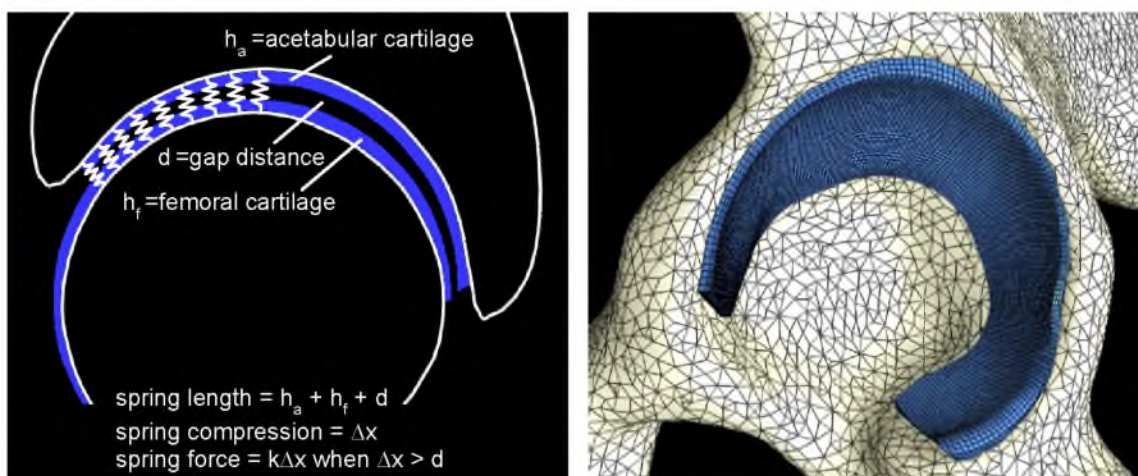


Figure 4.1. Sagittal view of DEA representation. Bones were rigid and cartilage was represented by an array of springs (left). 3D FEA model; triangular shell and hexahedral elements defined cortical bone and cartilage, respectively (right).

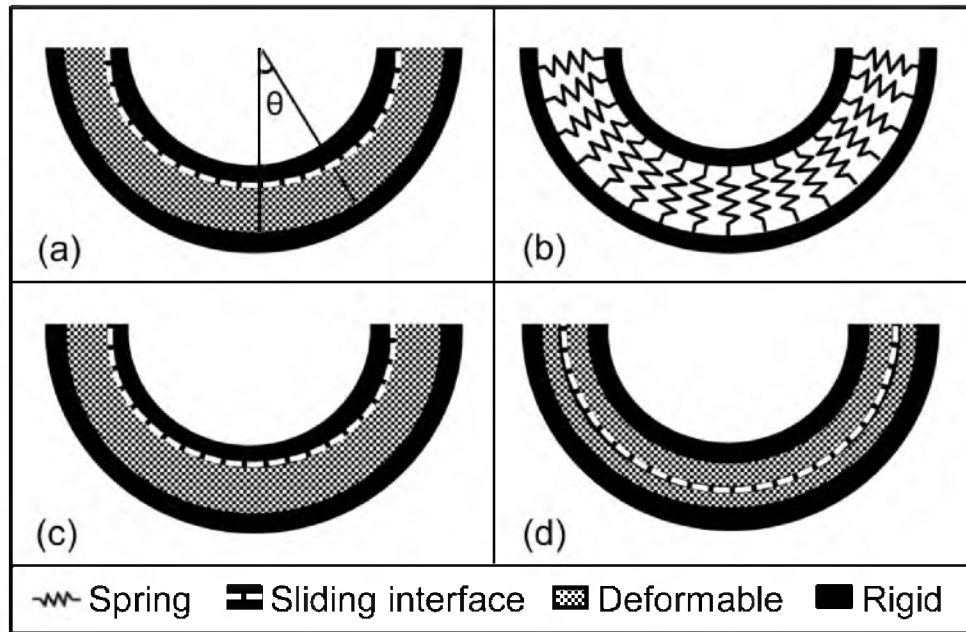


Figure 4.2. Schematic of verification problem under 2000 N load. Geometry was concentric: inner rigid material $r = 20$ mm, outer rigid material $r = 24$ mm, 4 mm thick cartilage between rigid materials. (a) Analytical solution modeled a single cartilage layer. Contact stress was calculated as a function of theta, the angle from vertical. (b) A single cartilage layer was represented by springs in DEA. (c) One layer FEA model. (d) Two layer FEA model.

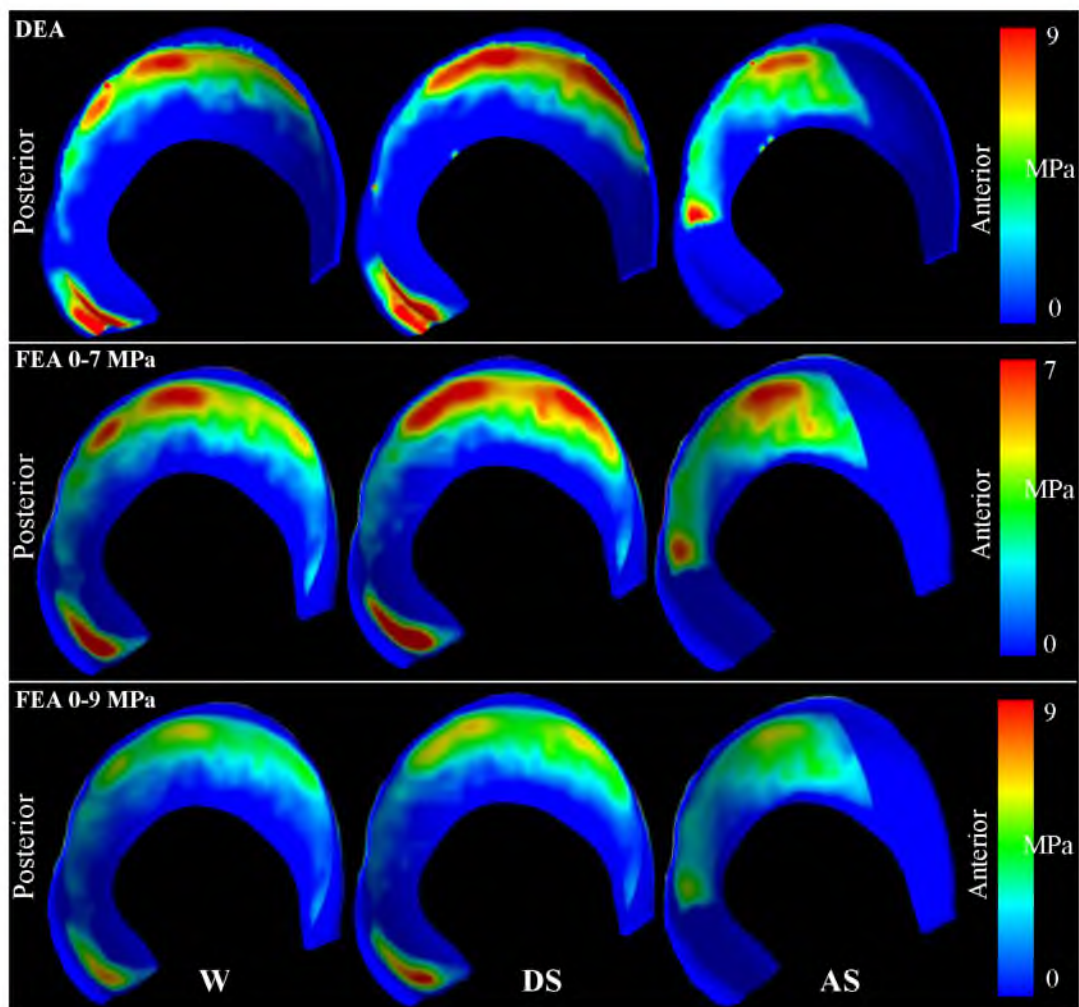


Figure 4.3. Contact stress patterns corresponded well between DEA and FEA for walking (W), descending stairs (DS), and ascending stairs (AS). The top/middle rows were scaled differently to show similarities in contact pattern. The bottom row shows the FEA results scaled the same as the DEA results (top row), indicating that DEA predicted higher contact stresses than FEA.

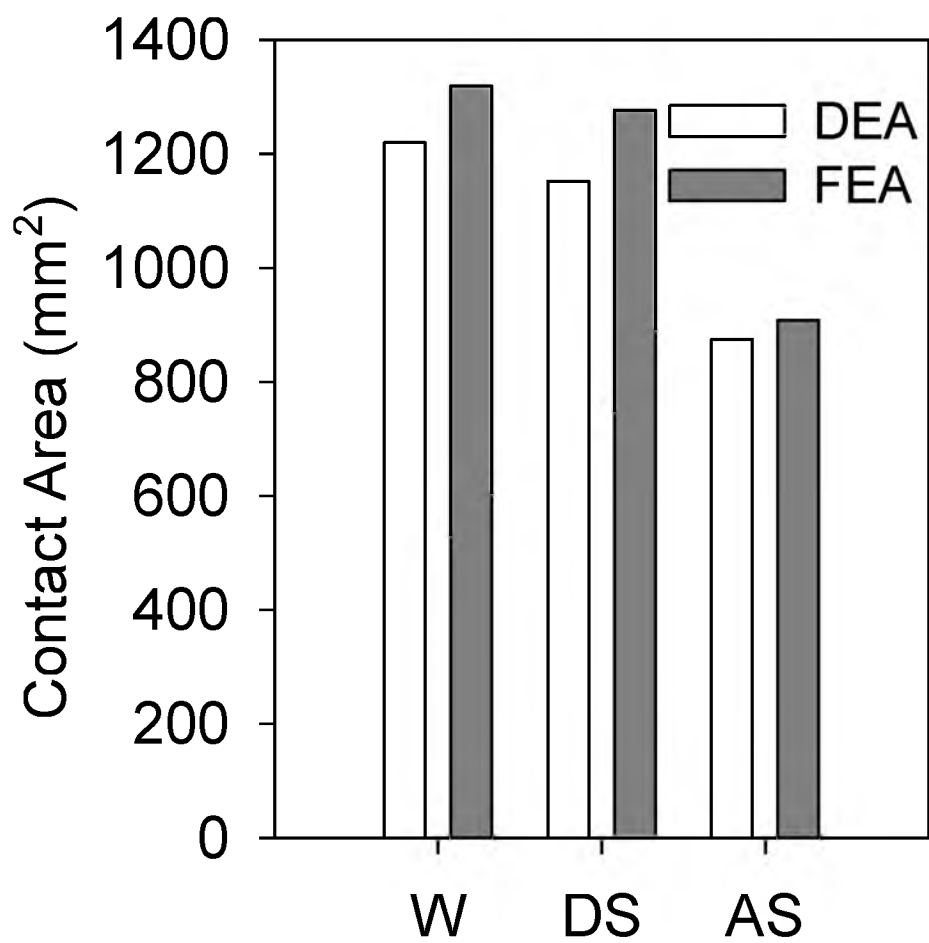


Figure 4.4. DEA contact areas were comparable to FEA predictions for walking (W), descending stairs (DS), and ascending stairs (AS).

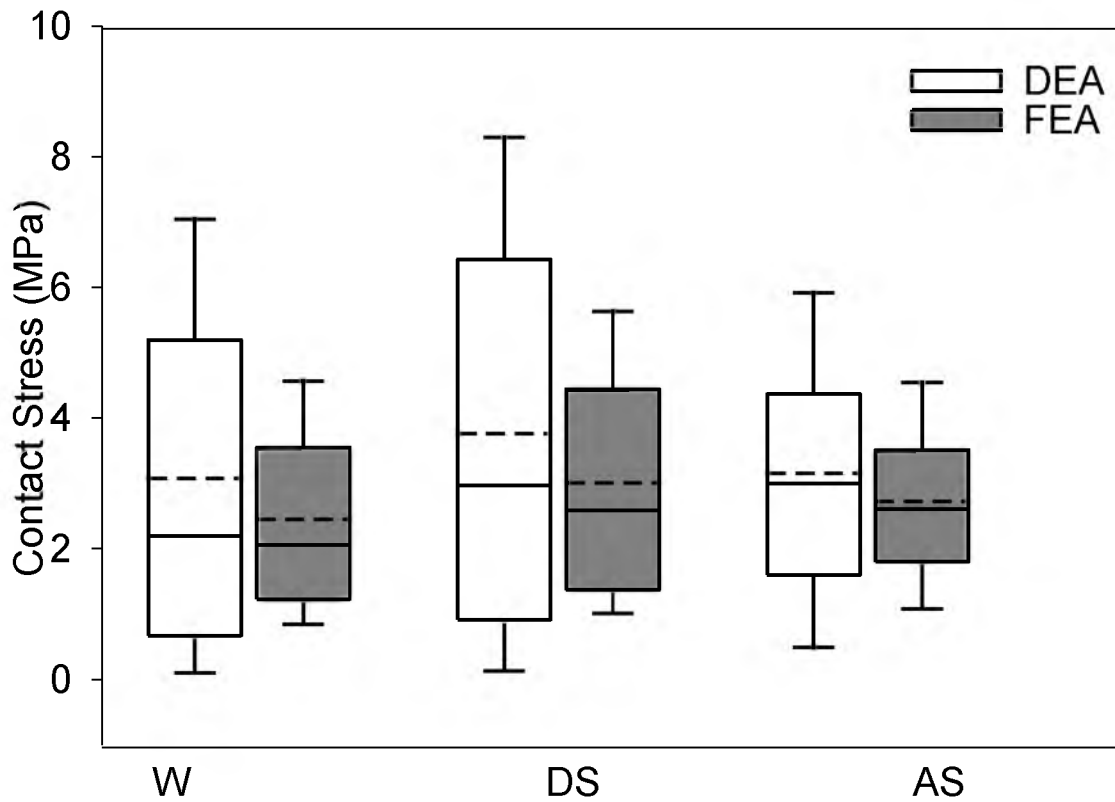


Figure 4.5. Box plots of cartilage contact stress for the DEA and FEA models under conditions of walking (W), descending stairs (DS), and ascending stairs (AS). Plots indicate the 25th and 75th percentiles and error bars indicate the 5th and 95th percentiles. Contact stresses predicted by DEA were elevated and more variable, especially at higher values. The mean (solid lines) and median contact stresses (dashed lines) were higher in DEA in all loading conditions.

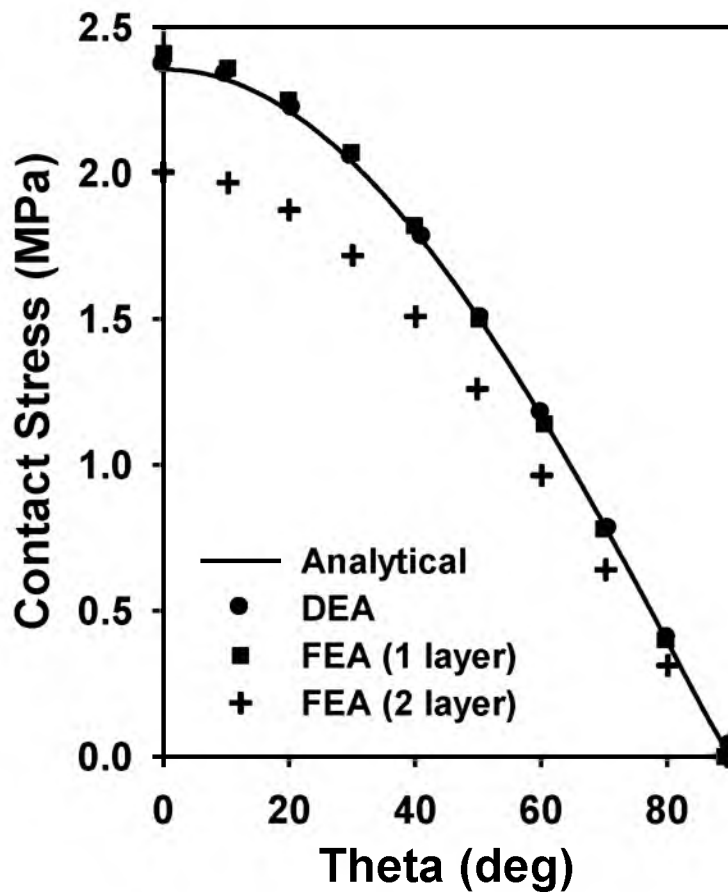


Figure 4.6. Comparisons of contact stresses predicted by FEA and DEA to an analytical solution. Contact stress predictions were consistent between analytical, DEA, FEA (1 layer) but reduced in FEA (2 layer). In the 2 layer FEA model, the difference in contact stresses was largest at the location of maximum contact stress ($\theta = 0$) where DEA predicted a contact stress higher than the two layer FEA model.

CHAPTER 5

3D DUAL ECHO STEADY STATE (DESS) MRI ACCURATELY QUANTIFIES ACETABULAR CARTILAGE THICKNESS

5.1 Abstract

The ability of hip-preserving surgery to delay osteoarthritis depends on the thickness of cartilage prior to surgery. Magnetic resonance imaging (MRI) is the preferred modality to assess hip cartilage. However, the accuracy of a high-resolution three-dimensional (3D) MRI sequence to image the thickness of hip cartilage has not been reported.

The objectives of this study were: first, to develop a 3D DESS MR arthrography protocol with hip traction; second, using physical measurements of cartilage thickness as the reference standard, quantify the accuracy of acetabular cartilage thickness estimated from 3D surfaces segmented from the 3D DESS MR images.

3D DESS MRI scans of four intact cadaver hips were obtained before and after cores of cartilage were harvested from the acetabulum; the two MRIs were spatially aligned to reference positions of the cores. The thickness of cartilage cores was measured under microscopy. Using automatic and semi-automatic segmentation, 3D reconstructions of acetabular cartilage were generated from the images. Using Bland

Altman plots, physical measurements were compared to those from the 3D reconstructions.

With traction, MR images qualitatively demonstrated excellent separation between acetabular and femoral cartilage layers; good signal contrast between subchondral bone, cartilage, and saline facilitated nearly automatic segmentation. Using both segmentation techniques, acetabular cartilage thickness from the 3D reconstructions could be estimated within ~0.5 mm of the physical measurements with 95% confidence.

The chosen 3D DESS protocol accurately measures acetabular cartilage thickness. As a nearly automatic segmentation process, 3D reconstructions from the chosen MR protocol could be used for preoperative planning.

5.2 Introduction

Hip osteoarthritis (OA) is a substantial economic and societal burden, affecting 9 million US citizens^{1,2}. Within the last decade, bony deformities characterized as acetabular dysplasia and femoroacetabular impingement (FAI) have been implicated as the primary cause of hip OA in young adults^{3,4}. In dysplasia, the mechanism of OA is thought to be decreased femoral head coverage, which causes increased loading of the labrum and cartilage. In FAI, acetabular over-coverage and/or an abnormally shaped femoral head may cause focal cartilage lesions from excessive shearing and/or premature abutment between the femur and acetabulum.

Hip-preserving surgeries aim to prevent end-stage osteoarthritis and the need for hip arthroplasty in FAI and dysplasia patients by restoring normative coverage and contact mechanics⁴⁻⁶. The success of surgery relies, in part, on an accurate preoperative

assessment of bone anatomy and cartilage thickness. The integrity and thickness of hyaline cartilage is particularly important as extensive damage or thinning to cartilage is a known contraindication for hip-preserving surgery^{5,6}. Radiographs are limited in their ability to discern subtle anatomical deformities, and do not provide detailed information of the hyaline cartilage thickness. With the addition of intra-articular contrast, CT arthrography (CTA) provides high-resolution volumetric images that have been shown to accurately visualize bone and cartilage⁷⁻¹¹. However, in recent years, MRI has become the preferred modality to assess FAI and dysplasia as it does not use ionizing radiation.

Clinical MRI protocols of the hip typically acquire two-dimensional (2D) fast spin-echo (FSE) sequences¹²⁻¹⁴. While 2D FSE sequences yield images with excellent tissue contrast and high in-plane spatial resolution, reduced out-of-plane resolution (i.e. thick image slices) may not visualize pathology due to partial volume averaging¹⁵. Three-dimensional (3D) sequences minimize partial volume effects and through-plane distortion by acquiring thin, continuous image slices. From a single scan, 3D acquisitions that are of high, nearly isotropic resolution can be postprocessed to any desired plane to enable a comprehensive assessment of the joint. Images from a 3D acquisition can also be segmented to display 3D anatomy for bone and cartilage to plan surgery¹⁶. Postprocessing of these surfaces can yield maps of cartilage thickness that may stage OA^{7,10,16,17}. Finally, 3D surfaces provide the geometry for patient-specific computer models to estimate cartilage contact mechanics (e.g. finite and discrete element analyses)^{8,9,18-21}.

MRI of the hip is inherently challenging due to its deep location in the body and spherical geometry. Long scan times may be required to obtain high-resolution images

that minimize stair-case artifact and accurately visualize thin acetabular and femoral cartilage while still obtaining adequate signal to noise (SNR) in a joint surrounded by thick soft tissue^{13,15}. Additionally, the tight fitting and congruent hip joint make it difficult to distinguish opposing layers of cartilage. With improved technology and use of 3D gradient echo imaging techniques that utilize small excitation pulses and short repetition times, 3D scans of the hip have been achieved in reasonable scan times^{3,17,22,23}. However, resolution was limited and traction was not always included, making it difficult to distinguish the boundary between acetabular and femoral cartilage^{3,22,23}.

Owed to its superior SNR and signal contrast previously demonstrated when imaging knee cartilage, 3D dual echo steady state (DESS) is a promising sequence to image the hip^{22,24-29}. 3D DESS can achieve nearly isotropic, high-resolution acquisitions in relatively short scan times. Also, using DESS, cortical bone appears to be displayed as negative signal, highlighting the potential of this protocol to image cartilage and bone in a single acquisition. With the addition of traction to separate acetabular and femoral cartilage, and intra-articular fluid to distinguish the joint space boundary, 3D DESS MRI could provide a feasible protocol to generate images of bone and cartilage in the hip. The objectives of this study were to: 1) develop a 3D DESS MR arthrography protocol with hip traction, and 2) using physical measurements of cartilage thickness as the reference standard, quantify the accuracy of acetabular cartilage thickness estimated from 3D surfaces segmented from the 3D DESS MR images.

5.3 Methods

The general approach involved obtaining 3D DESS MRI scans of four intact cadaver hips before and after cores of cartilage were harvested from the acetabulum; the two MRIs were spatially aligned to reference positions of the cores. The thickness of each core was measured and compared to those obtained from the 3D reconstructions of the first MRI scan.

5.3.1 Injection, Traction, and Initial MRI Scan

Two fresh-frozen pelvis to toe-tip cadavers (32 year female, 55 year male) were utilized (IRB# 11755). To improve delineation between femoral and acetabular cartilage, a musculoskeletal radiologist (CJH) injected 25 ml sodium chloride 0.9% (saline) into each hip through a 22-gauge spinal needle using a lateral oblique approach. To allow saline to fill the joint space, bilateral traction was applied using a custom device made of polyvinylchloride tubing (Fig. 5.1). Traction was applied by first securing the pelvis to the proximal segment of the device using a wide strap. Next, a strap was attached to the ankle; an inferiorly directed force of approximately 5-10 kg was applied to the ankle by tightening a plastic cable tie that was fixed to the distal segment of the traction device (Fig. 5.1). The process of applying traction was repeated for the contralateral limb.

The pelvis and both hip joints were imaged using a 3.0-T magnet (Magnetom Trio; Siemens Medical Solutions, Erlangen, Germany) with a built-in spine-matrix coil and body-matrix phased-array coil placed about the pelvic region. Three-dimensional MR images were acquired in the coronal plane using a water-excitation DESS sequence. The field-of-view of the scan encompassed the entire pelvis with a 0.5 x 0.5 mm in-plane

resolution and 0.7 mm thickness. Imaging parameters included a repetition time of 16.3 ms, echo time of 4.7 ms, flip angle of 25°, and bandwidth of 186 Hz/pixel. Image acquisition time was 12 minutes using an acceleration factor of 2 with generalized autocalibrating partially parallel acquisition (GRAPPA).

5.3.2 Physical Measurements of Cored Cartilage Samples

After the first MRI, the acetabulum was accessed by incising the anterior and lateral hip/thigh soft tissue. The hip was dislocated by flexing and externally rotating the thigh with the ligamentum teres excised³⁰. Osteochondral cores were harvested from the acetabulum using a 5.3-mm trephine (Stryker Instruments, Kalamazoo, MI). The trephine was modified to include a center boring pin that facilitated removal of the plug. A total of 12 cores were acquired: 3 each from the anteroinferior, anterosuperior, posteroinferior, and posterosuperior regions^{7,10,31}.

Cores were bisected longitudinally using a custom miter-box to ensure equal division. Cores were positioned on a microscope stage (Nikon SMZ800, Nikon Instruments, NY) with the bisected side facing up and a stage micrometer in the field-of-view at the level of the bisected edge. Digital microscope images (Optronics Microscope Camera, Optronics, CA) were obtained of each bisected core at a magnification of 25X (Fig. 5.2). Each image was calibrated using the micrometer. Cartilage thickness was measured at the center of each core using ImageJ³². Measurements of thickness for both halves of the core were averaged. Two observers (CLA and LSM) measured cartilage thickness; nearly 2 weeks later, one observer (CLA) repeated the measurements.

5.3.3 Second MRI Scan

After harvesting cartilage cores from both hips, a second MRI was obtained to determine the position of the cores. Prior to this scan, saline-filled cylindrical tubes sized to match the core diameter were implanted in each cored hole to serve as fiducials. The second MRI was acquired following the same imaging parameters as the first. However, dissection to remove cartilage cores made it possible to image the acetabulum in the absence of bilateral traction.

5.3.4 MRI Postprocessing

Computational methods were used to quantify cartilage thickness from MR images (Fig. 5.3). Briefly, the acetabular cortex was segmented, reconstructed, and cropped equally in both MRIs. Next, the acetabular cortex from the first MRI was aligned to the acetabulum from the second scan. This transformation was applied to the acetabular cartilage, segmented from the first MRI, to register the cartilage to the second MRI. With both acetabular cortex and cartilage surfaces transformed, the saline-filled fiducials defined the spatial location of each core. Cartilage thickness from the first scan was calculated at the appropriate locations. Details are described below.

5.3.4.1 Segmentation and Three-dimensional Reconstruction

All segmentation and surface reconstructions were generated using Amira (5.4.5, Visage Imaging, San Diego, CA). First, image stacks were cropped to include those image slices that encompassed both hip joints and up-sampled using a Lanczos filter kernel to improve the resolution of the segmentation mask (0.25 x 0.25 mm in-plane

resolution, 0.23 mm thickness)⁸. Pixels exclusively representing cortical bone, acetabular cartilage, and saline were selected in ImageJ at a midjoint axial image. These pixels defined intensity distributions to determine thresholds for segmentation. Thresholds were calculated as a weighted midpoint between maximum and minimum intensities. A weighted midpoint was chosen to account for drastic differences between intensities that would otherwise overestimate brighter pixels, caused by volumetric averaging with adjacent pixels. Thresholds were determined for each hip and scan independently.

The ability of automatic and semi-automatic segmentation techniques to define cartilage anatomy was assessed separately. Specifically, the acetabular cartilage and the outer cortex of the acetabulum in the first MRI were segmented automatically by selecting the pixels within the predetermined thresholds as defined above. Next, a user manually edited the initial automatic mask for regions that did not, on qualitative inspection, appear to correctly define the cartilage-saline and/or cartilage-bone boundary. Semi-automatic segmentation was performed on two occasions by one observer (CLA) with a time lapse of 2 weeks, and by a separate observer (LSM) to quantify inter- and intra-observer repeatability. The acetabular cortex and saline-filled fiducials were segmented and reconstructed from the second MRI scan in a similar manner. However, less soft tissue surrounded the hip joint in the second scan, which reduced SNR. Therefore, greater manual segmentation was required. All masks were reconstructed into 3D surfaces using built-in algorithms in Amira that applied controlled smoothing and decimation to reduce artifact (Fig. 5.4).

5.3.4.2 Spherical Cropping

An objective approach was applied to align 3D surfaces from the first and second MRI. First, triangulated faces representing the articular region of the acetabular cortex were selected using first principal curvature as calculated in the FEBio software suite³³. From these selected faces, the radius and center of the best-fit sphere was calculated using a linear least-squares-optimization³³. This sphere was increased to a radius of 45 or 47 mm (smaller radius for female specimen) to define a boundary at which to crop the reconstructed cortex created from each MRI scan. By spherically cropping, the two triangulated reconstructions of the acetabular cortex could be aligned without bias introduced as a result of differences in the position of the hip in the MR scanner bed between successive scans.

5.3.4.3 Surface Alignment and Transformation

Once cropped, the two acetabular cortex surfaces were aligned using an iterative closest point algorithm built into Amira (Amira MeshPack 5.4.5, Visage Imaging, San Diego, CA) that minimized the root mean square distance between surfaces. The transformation that aligned the first to second scan was applied to the acetabular cartilage reconstruction; the resulting surfaces of acetabular cartilage, acetabular cortex, and saline fiducials were then spatially positioned in the second MRI. The same transformation was used for each hip for both automatically and semi-automatically segmented reconstructions. By visualizing the surfaces together, regions where cartilage was cored (saline-filled fiducials) could be identified with respect to the reconstructions of the first scan.

5.3.4.4 Cartilage Thickness

The thickness of the reconstructed acetabular cartilage was determined using a validated algorithm¹⁹. Briefly, the distance between cartilage and cortex surfaces was determined by projecting the surface normal vector of faces representing the subchondral bone boundary to the faces representing the outer surface of cartilage. Thickness was then mapped as a 3D color fringe plot, where each node that defined the surface of the reconstructed cartilage from the first MRI scan had a unique thickness value. Finally, cartilage thicknesses at nodes surrounding each saline-filled fiducial were averaged and compared to the thickness of the physically cored sample.

5.3.5 Data Analysis and Statistics

Inter- and intra-observer repeatability of physically measured cartilage and semi-automatic segmented MRI cartilage thickness were quantified using the intraclass correlation coefficient (ICC)³⁴. Inter-observer repeatability was assessed between the first set of measurements for both observers. Observer agreement was interpreted as: slight if the ICC < 0.20, fair if 0.21-0.40, moderate if 0.41-0.60, substantial if 0.61-0.80, and almost perfect if >0.80³⁵. For subsequent analysis, the physical and semi-automatic segmented MRI thickness measurements from both observers (CLA measures 1 and 2, LSM measure 1) were averaged.

Bland-Altman plots assessed agreement between MRI-based estimates of cartilage thickness and physical measurements³⁶⁻³⁸. Results for MRI cartilage thickness determined with automatic and semi-automatic segmentation were presented separately for comparison of the two techniques. The limits of agreement were calculated and

plotted, representing the 95% confidence interval of differences between physical and MRI-based thicknesses³⁶⁻³⁸. The relationship between MRI and physical thicknesses was also assessed with linear regression, including calculations for the coefficient of determination. All statistical analyses were performed in Stata (v 11.0, StataCorp LP, College Station, TX), with plots generated using SigmaPlot (v 11.0; Systat Software, San Jose, CA). Significance was set at $P \leq 0.05$.

To account for clustered data at the level of each hip ($n = 4$) and cadaver ($n = 2$), the variance was adjusted using the design effect. The corrected variance was multiplied by the design effect, DE: $DE = 1 + (n-1)(ICC)$, where n was the average cluster size and the ICC was computed at the hip level and cadaver level of clustering^{7,39}. Both ICCs were zero when truncated to six decimal places. Therefore, the variance was not increased and conventional statistical methods that assume independence of observations were applied.

5.4 Results

With traction, 3D DESS qualitatively demonstrated excellent separation between acetabular and femoral cartilage layers in the axial, sagittal, and coronal planes (Fig. 5.4). Throughout most of the hip, good signal contrast was observed between bone, cartilage, and saline (Fig. 5.4). Except for a few regions within the articulating surface, automatic segmentation delineated cortical bone, cartilage, and saline well. Regions where this was an exception were constrained to the cartilage-saline boundary immediately around air bubbles located at the anterior injection site of two hips, in the

posteroinferior region of one hip where the joint space was not filled with ample saline, and in a region of suspected low density in subchondral bone (Fig. 5.5).

As measured experimentally, cored cartilage thickness ranged from 0.80 to 2.95 mm (mean, 1.51 ± 0.49), compared to 0.76 to 3.21 mm (mean, 1.60 ± 0.50) and 0.77 to 3.20 mm (mean, 1.56 ± 0.50) as estimated from MRI reconstructions with automatic and semi-automatic segmentation, respectively. Acetabular reconstructions with cartilage thickness plotted spatially demonstrated that cartilage was thickest along the superolateral acetabulum and thinnest in the medial aspect of the posterior region (Fig. 5.6). In general, cartilage was thinner medially and increased in thickness towards the lateral rim.

From Bland Altman analysis, cartilage was reconstructed with automatic segmentation to a bias of 0.10 mm (average difference between MRI and physical measurements) and repeatability coefficient of ± 0.51 mm (1.96 X the standard deviation of the differences between MRI and physical measurements). Using semi-automatic segmentation, the bias improved to 0.06 mm, as did the repeatability coefficient at ± 0.43 mm. The Bland Altman plot demonstrated uniform scatter. With no proportional bias, standard 95% confidence limits were -0.41 to 0.61 mm for automatic and -0.37 to 0.49 mm for semi-automatic segmentation³⁷ (Fig. 5.7).

Linear regression of MRI measured thickness versus physical thickness yielded a significant ($P < 0.001$) relationship for both automatic and semi-automatic segmentation. Linear regression of MRI values from automatic segmentation (auto MRI = $0.26 + 0.89$ X physical thickness; $R^2 = 0.74$) was very similar to that of semi-automatic segmentation (semi-automatic MRI = $0.17 + 0.93$ X physical thickness; $R^2 = 0.81$) (Fig. 5.8).

Inter- and intra-observer repeatability of cartilage thickness as measured from microscope images and estimated from reconstructions generated from semi-automatically segmented MRI images were almost perfect. For microscope measurements, inter- and intra-observer ICC values were 0.948 and 0.950, respectively, and for semi-automatically segmented MRI thicknesses, 0.968 and 0.940, respectively.

5.5 Discussion

This study demonstrated that a 3D DESS MRI protocol for the hip that includes traction and intra-articular saline provides high-resolution images with excellent separation between femoral and acetabular cartilage and delineation between bone, cartilage, and saline. Using both automatic and semi-automatic segmentation techniques, acetabular cartilage thickness from the 3D reconstructions could be estimated within ~0.5 mm of the physical measurements with 95% confidence. Thus, we believe the chosen 3D DESS MRI protocol could potentially be used to stage OA and plan treatment for patients who are candidates for hip-preservation surgery.

The acetabular cartilage thickness profiles and average thickness of 1.51 ± 0.49 mm found in our study are consistent with previous findings^{7,10,11,17,40-42}. Using MRA, Nishii et al. reported an average acetabular cartilage thickness of 1.91 mm, ranging from 1.1 to 4.0 mm, as measured from digitized anatomic slices in 4 cadaveric hips¹⁷. Also, a study of 10 cadaveric hips measured average acetabular cartilage thicknesses ranging from 1.06 ± 0.24 mm in the posteromedial acetabulum to 1.83 ± 0.45 mm in the superolateral acetabulum⁴⁰. From cartilage thickness plots (Fig. 5.6), our findings

concur with Shepherd and Seedhom that thinner cartilage is located medially, and the thickest cartilage is located in the superolateral acetabulum^{7,17,40,41}.

As reported to date, the most accurate methods described for imaging acetabular cartilage thickness have used surface reconstructions to calculate thickness rather than pixel-based measurement of thickness on image slices^{7,10,11,17,43}. Studies by Wyler et al. and Hodler et al. measured thickness on 2D images and concluded that hip cartilage thickness could not be accurately determined in at least half of MR images^{11,17,43}. Errors in referencing anatomic slice measurements to their respective image-based locations as well as the limitation of measurement accuracy from in-plane scan resolution likely explain the reduced accuracy with measurements made on image slices. In contrast, use of smoothed and decimated surfaces, as was done in our study, may yield subvoxel accuracy as reconstructions inherently remove noise.

Allen et al. and Tamura et al. utilized 3D reconstructions of CTA images to estimate acetabular cartilage thickness; their results are the most accurate to date^{7,10}. The bias and 95% tolerance limit of semi-automatic segmentation using DESS MRI in our study (0.06 ± 0.43 mm) represents a slight improvement compared to Allen et al. (0.13 ± 0.46 mm) and Tamura et al. (0.18 ± 0.75 mm). A validation study by Nishii et al. determined the mean error of measurements from surface reconstructions generated from MRI as 0.28 ± 0.23 mm¹⁷. Though each of these studies utilized 3D models, we believe our results demonstrate superior accuracy because we acquired higher resolution scans and up-sampled images for segmentation. For example, Nishii et al. utilized a 0.625 mm in-plane and 1.5 mm out-of-plane resolution compared to the 0.5 mm in-plane and 0.7 mm out-of-plane resolution utilized herein.

In our study, MRI measurements based on automatic and semi-automatic segmentation had similar accuracy when compared to physical thickness of cored specimens. Nevertheless, semi-automatic segmentation was associated with improved accuracy, evidenced by tighter 95% tolerance intervals in the Bland Altman plots and a higher coefficient of determination (Figs. 5.7, 5.8). The fact that automatic segmentation did not identify the correct boundaries in all locations where cartilage was cored explains why semi-automatic segmentation improved the accuracy (Fig. 5.5). Our study highlights the importance of eliminating air bubbles and using traction to enable saline to fill the entire joint space. The area suspected to have low subchondral bone density as the cause for segmentation error also suggests that subchondral bone should be sufficiently intact to obtain accurate measurements of cartilage thickness using 3D DESS.

There are several potential benefits to the described 3D DESS MR imaging protocol. First, as with any MR sequence, there is no exposure to ionizing radiation. Second, the accuracy of cartilage thickness measurements reported from this sequence is highest for MRI reported to date and is as good or better than CTA^{7,10}. Third, inclusion of traction enabled separation of acetabular from femoral cartilage. Clinically, it is important to assess femoral and acetabular cartilage independently to stage OA. For example, femoral cartilage thinning is typically indicative of advanced damage as deterioration of the acetabular cartilage usually precedes femoral cartilage deterioration^{4,44}. Therefore, consistent with the recommendation of others, we believe traction is a necessary component for imaging studies of the hip^{8-10,17,45-47}.

Acetabular cartilage thickness could be measured at discrete locations on a single image slice from the 3D DESS MR sequence. However, for diagnostic information and

surgical planning, we believe 3D reconstructions of the bone cortex and cartilage provide more descriptive data to guide treatment planning. Fringe plots of cartilage thickness template relative to the bony anatomy in 3D, which could elucidate damage patterns and help surgeons to choose between hip arthroplasty and hip-preserving surgery. It has been shown that predictions of cartilage contact stress by patient-specific finite element models are sensitive to changes in the thickness of cartilage as portrayed in the model⁴⁸. Therefore, beyond clinical assessments, having the ability to accurately create 3D reconstructions of cartilage from MRI directly translates into increased accuracy of computer models.

Using CTA, the attenuation of cortical bone closely represents that of the intra-articular radio-opaque contrast injected into the joint capsule^{49,50}. As a result, CTA images of the hip require substantial manual correction of segmentation to distinguish the bone-contrast boundary to create 3D models⁷⁻⁹. In contrast, DESS MR images in our study clearly delineated cortical bone, cartilage, labrum, and injected saline at varying gray-levels such that each material had a unique intensity range. Thus, use of DESS MRI may automate the process to generate 3D surface models for important structures of the hip.

There are some limitations with this study. First, the sample size was small, with a total 4 hips. Also, postprocessing of the MR images may have introduced error with the alignment procedure used to relate the first and second scans. Because bone and cartilage surfaces are generally smooth in the articulating region, we would not expect dramatic changes in thickness at the immediate regions identified by saline fiducials. Therefore, small errors in locating the spatial position of the cartilage cores would conceivably have

minimal effect on the accuracy of measurements. Finally, our approach to measure acetabular thickness relied on segmentation of the cartilage-subchondral bone boundary, but we did not explicitly quantify the accuracy of DESS MRI to measure bone anatomy. However, given the favorable results herein, we believe DESS MRI can clearly delineate the cartilage-subchondral bone boundary. Future studies will need to assess the accuracy of DESS MRI for measuring the thickness of subchondral and cortical bone.

Our study simulated patient imaging as closely as possible by scanning intact pelvis to toe-tip specimens to obtain cartilage thickness maps. Translating this protocol into live subjects may be a challenge due to motion artifact and need for extended hip traction. Future studies will incorporate methods to minimize motion artifact by scanning each hip separately. We will also develop methods to stabilize the hip in traction despite possible muscular co-contraction.

In summary, using both automatic and semi-automatic segmentation, acetabular cartilage thickness from 3D reconstructions of DESS MR images could be estimated within ~ 0.5 mm of the physical measurements with 95% confidence. Implementation of 3D DESS MRI of the hip may be beneficial to the clinical care of patients as it avoids radiation while maintaining the highest reported accuracy of cartilage thickness measurements from the available volumetric imaging modalities. As a nearly automatic segmentation process, 3D reconstructions from the chosen MR protocol could stage hip OA for preoperative decision making.

5.6 Acknowledgements

Financial support from NIH #R01AR053344 and the University of Utah Funding Incentive Seed Grant Program is gratefully acknowledged.

5.7 References

1. Felson DT. 1994. Do occupation-related physical factors contribute to arthritis? *Bailliere's clinical rheumatology* 8: 63-77.
2. Murphy LB, Helmick CG, Schwartz TA, et al. 2010. One in four people may develop symptomatic hip osteoarthritis in his or her lifetime. *Osteoarthritis and cartilage / OARS, Osteoarthritis Research Society* 18: 1372-1379.
3. Apprigh S, Mamisch TC, Welsch GH, et al. 2012. Evaluation of articular cartilage in patients with femoroacetabular impingement (FAI) using T2* mapping at different time points at 3.0 Tesla MRI: a feasibility study. *Skeletal radiology* 41: 987-995.
4. Ganz R, Leunig M, Leunig-Ganz K, et al. 2008. The etiology of osteoarthritis of the hip: an integrated mechanical concept. *Clinical orthopaedics and related research* 466: 264-272.
5. Clohisy JC, Knaus ER, Hunt DM, et al. 2009. Clinical presentation of patients with symptomatic anterior hip impingement. *Clinical orthopaedics and related research* 467: 638-644.
6. Cunningham T, Jessel R, Zurakowski D, et al. 2006. Delayed gadolinium-enhanced magnetic resonance imaging of cartilage to predict early failure of Bernese periacetabular osteotomy for hip dysplasia. *The Journal of bone and joint surgery American volume* 88: 1540-1548.
7. Allen BC, Peters CL, Brown NA, et al. 2010. Acetabular cartilage thickness: accuracy of three-dimensional reconstructions from multidetector CT arthrograms in a cadaver study. *Radiology* 255: 544-552.
8. Harris MD, Anderson AE, Henak CR, et al. 2012. Finite element prediction of cartilage contact stresses in normal human hips. *Journal of orthopaedic research : official publication of the Orthopaedic Research Society* 30: 1133-1139.
9. Henak CR, Carruth ED, Anderson AE, et al. 2013. Finite element predictions of cartilage contact mechanics in hips with retroverted acetabula. *Osteoarthritis and cartilage / OARS, Osteoarthritis Research Society* 21: 1522-1529.
10. Tamura S, Nishii T, Shiomi T, et al. 2012. Three-dimensional patterns of early acetabular cartilage damage in hip dysplasia; a high-resolution CT arthrography study. *Osteoarthritis and cartilage / OARS, Osteoarthritis Research Society* 20: 646-652.

11. Wyler A, Bousson V, Bergot C, et al. 2009. Comparison of MR-arthrography and CT-arthrography in hyaline cartilage-thickness measurement in radiographically normal cadaver hips with anatomy as gold standard. *Osteoarthritis and cartilage / OARS, Osteoarthritis Research Society* 17: 19-25.
12. Gold SL, Burge AJ, Potter HG. 2012. MRI of hip cartilage: joint morphology, structure, and composition. *Clinical orthopaedics and related research* 470: 3321-3331.
13. Mamisch TC, Bittersohl B, Hughes T, et al. 2008. Magnetic resonance imaging of the hip at 3 Tesla: clinical value in femoroacetabular impingement of the hip and current concepts. *Seminars in musculoskeletal radiology* 12: 212-222.
14. Smith TO, Hilton G, Toms AP, et al. 2011. The diagnostic accuracy of acetabular labral tears using magnetic resonance imaging and magnetic resonance arthrography: a meta-analysis. *European radiology* 21: 863-874.
15. Kijowski R, Gold GE. 2011. Routine 3D magnetic resonance imaging of joints. *Journal of magnetic resonance imaging : JMRI* 33: 758-771.
16. Peters CL, Erickson JA, Anderson L, et al. 2009. Hip-preserving surgery: understanding complex pathomorphology. *The Journal of bone and joint surgery American volume* 91 Suppl 6: 42-58.
17. Nishii T, Sugano N, Sato Y, et al. 2004. Three-dimensional distribution of acetabular cartilage thickness in patients with hip dysplasia: a fully automated computational analysis of MR imaging. *Osteoarthritis and cartilage / OARS, Osteoarthritis Research Society* 12: 650-657.
18. Abraham CL, Maas SA, Weiss JA, et al. 2013. A new discrete element analysis method for predicting hip joint contact stresses. *Journal of biomechanics* 46: 1121-1127.
19. Anderson AE, Peters CL, Tuttle BD, et al. 2005. Subject-specific finite element model of the pelvis: development, validation and sensitivity studies. *Journal of biomechanical engineering* 127: 364-373.
20. Gu DY, Hu F, Wei JH, et al. 2011. Contributions of non-spherical hip joint cartilage surface to hip joint contact stress. *Conference proceedings : Annual International Conference of the IEEE Engineering in Medicine and Biology Society IEEE Engineering in Medicine and Biology Society Conference 2011*: 8166-8169.

21. Yoshida H, Faust A, Wilckens J, et al. 2006. Three-dimensional dynamic hip contact area and pressure distribution during activities of daily living. *Journal of biomechanics* 39: 1996-2004.
22. Ellermann J, Ziegler C, Nissi MJ, et al. 2014. Acetabular cartilage assessment in patients with femoroacetabular impingement by using T2* mapping with arthroscopic verification. *Radiology* 271: 512-523.
23. Stelzeneder D, Mamisch TC, Kress I, et al. 2012. Patterns of joint damage seen on MRI in early hip osteoarthritis due to structural hip deformities. *Osteoarthritis and cartilage / OARS, Osteoarthritis Research Society* 20: 661-669.
24. Duc SR, Pfirrmann CW, Schmid MR, et al. 2007. Articular cartilage defects detected with 3D water-excitation true FISP: prospective comparison with sequences commonly used for knee imaging. *Radiology* 245: 216-223.
25. Eckstein F, Cicuttini F, Raynauld JP, et al. 2006. Magnetic resonance imaging (MRI) of articular cartilage in knee osteoarthritis (OA): morphological assessment. *Osteoarthritis and cartilage / OARS, Osteoarthritis Research Society* 14 Suppl A: A46-75.
26. Friedrich KM, Reiter G, Kaiser B, et al. 2011. High-resolution cartilage imaging of the knee at 3T: basic evaluation of modern isotropic 3D MR-sequences. *European journal of radiology* 78: 398-405.
27. Knuesel PR, Pfirrmann CW, Noetzli HP, et al. 2004. MR arthrography of the hip: diagnostic performance of a dedicated water-excitation 3D double-echo steady-state sequence to detect cartilage lesions. *AJR American journal of roentgenology* 183: 1729-1735.
28. Sutter R, Zubler V, Hoffmann A, et al. 2014. Hip MRI: how useful is intraarticular contrast material for evaluating surgically proven lesions of the labrum and articular cartilage? *AJR American journal of roentgenology* 202: 160-169.
29. Wirth W, Nevitt M, Hellio Le Graverand MP, et al. 2010. Sensitivity to change of cartilage morphometry using coronal FLASH, sagittal DESS, and coronal MPR DESS protocols--comparative data from the Osteoarthritis Initiative (OAI). *Osteoarthritis and cartilage / OARS, Osteoarthritis Research Society* 18: 547-554.
30. Ganz R, Gill TJ, Gautier E, et al. 2001. Surgical dislocation of the adult hip a technique with full access to the femoral head and acetabulum without the risk of avascular necrosis. *The Journal of bone and joint surgery British volume* 83: 1119-1124.

31. El-Khoury GY, Alliman KJ, Lundberg HJ, et al. 2004. Cartilage thickness in cadaveric ankles: measurement with double-contrast multi-detector row CT arthrography versus MR imaging. *Radiology* 233: 768-773.
32. Schneider CA, Rasband WS, Eliceiri KW. 2012. NIH Image to ImageJ: 25 years of image analysis. *Nature methods* 9: 671-675.
33. Maas SA, Ellis BJ, Ateshian GA, et al. 2012. FEBio: finite elements for biomechanics. *Journal of biomechanical engineering* 134: 011005.
34. Streiner D, Norman G. 1995. *Health Measurement scales: A practical guide to their development and use*, 2nd ed. Oxford, England: Oxford University Press; p.
35. Landis JR, Koch GG. 1977. The measurement of observer agreement for categorical data. *Biometrics* 33: 159-174.
36. Bland JM, Altman DG. 1986. Statistical methods for assessing agreement between two methods of clinical measurement. *Lancet* 1: 307-310.
37. Ludbrook J. 2010. Confidence in Altman-Bland plots: a critical review of the method of differences. *Clinical and experimental pharmacology & physiology* 37: 143-149.
38. Mantha S, Roizen MF, Fleisher LA, et al. 2000. Comparing methods of clinical measurement: reporting standards for bland and altman analysis. *Anesthesia and analgesia* 90: 593-602.
39. McCarthy W, Thompson, DR. 2007. *The Analysis of Pixel Intensity (Myocardial Signal Density) Data: The Quantification of Myocardial Perfusion by Imaging Methods. COBRA Preprint Series: Working Paper 23.*
40. Athanasiou KA, Agarwal A, Dzida FJ. 1994. Comparative study of the intrinsic mechanical properties of the human acetabular and femoral head cartilage. *Journal of orthopaedic research : official publication of the Orthopaedic Research Society* 12: 340-349.
41. Shepherd DE, Seedhom BB. 1999. Thickness of human articular cartilage in joints of the lower limb. *Annals of the rheumatic diseases* 58: 27-34.
42. von Eisenhart R, Adam C, Steinlechner M, et al. 1999. Quantitative determination of joint incongruity and pressure distribution during simulated gait and cartilage thickness in the human hip joint. *Journal of orthopaedic research : official publication of the Orthopaedic Research Society* 17: 532-539.

43. Hodler J, Trudell D, Pathria MN, et al. 1992. Width of the articular cartilage of the hip: quantification by using fat-suppression spin-echo MR imaging in cadavers. *AJR American journal of roentgenology* 159: 351-355.
44. Redmond JM, Gupta A, Stake CE, et al. 2014. The prevalence of hip labral and chondral lesions identified by method of detection during periacetabular osteotomy: arthroscopy versus arthrotomy. *Arthroscopy : the journal of arthroscopic & related surgery : official publication of the Arthroscopy Association of North America and the International Arthroscopy Association* 30: 382-388.
45. Nakanishi K, Tanaka H, Nishii T, et al. 1999. MR evaluation of the articular cartilage of the femoral head during traction. Correlation with resected femoral head. *Acta radiologica* 40: 60-63.
46. Nishii T, Nakanishi K, Sugano N, et al. 1998. Articular cartilage evaluation in osteoarthritis of the hip with MR imaging under continuous leg traction. *Magnetic resonance imaging* 16: 871-875.
47. Wettstein M, Guntern D, Theumann N. 2008. Direct MR arthrography of the hip with leg traction: feasibility for assessing articular cartilage. *AJR American journal of roentgenology* 191: W206; author reply W207.
48. Anderson AE, Ellis BJ, Maas SA, et al. 2010. Effects of idealized joint geometry on finite element predictions of cartilage contact stresses in the hip. *Journal of biomechanics* 43: 1351-1357.
49. Chai JW, Choi JA, Choi JY, et al. 2014. Visualization of joint and bone using dual-energy CT arthrography with contrast subtraction: in vitro feasibility study using porcine joints. *Skeletal radiology* 43: 673-678.
50. Simoni P, Leyder PP, Albert A, et al. 2014. Optimization of computed tomography (CT) arthrography of hip for the visualization of cartilage: an in vitro study. *Skeletal radiology* 43: 169-178.

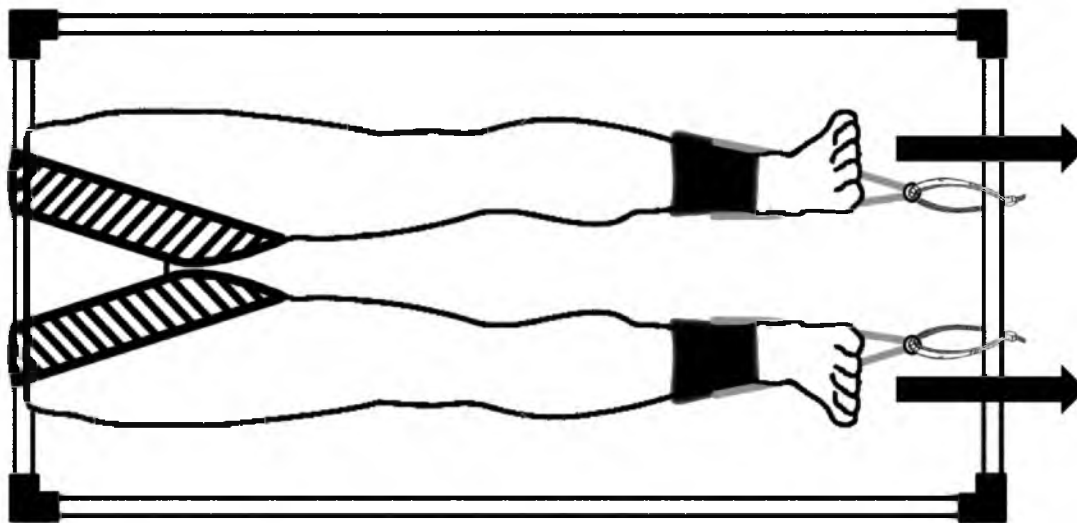


Figure 5.1. Schematic of custom traction frame made of polyvinylchloride. The pelvis was secured to the proximal segment of the traction device using wide Velcro™ straps. Bilateral traction was applied through straps attached to the ankles. An inferiorly directed force (indicated by arrows) was applied to each ankle strap with a plastic cable tie that was then fixed to the distal segment of the traction device.

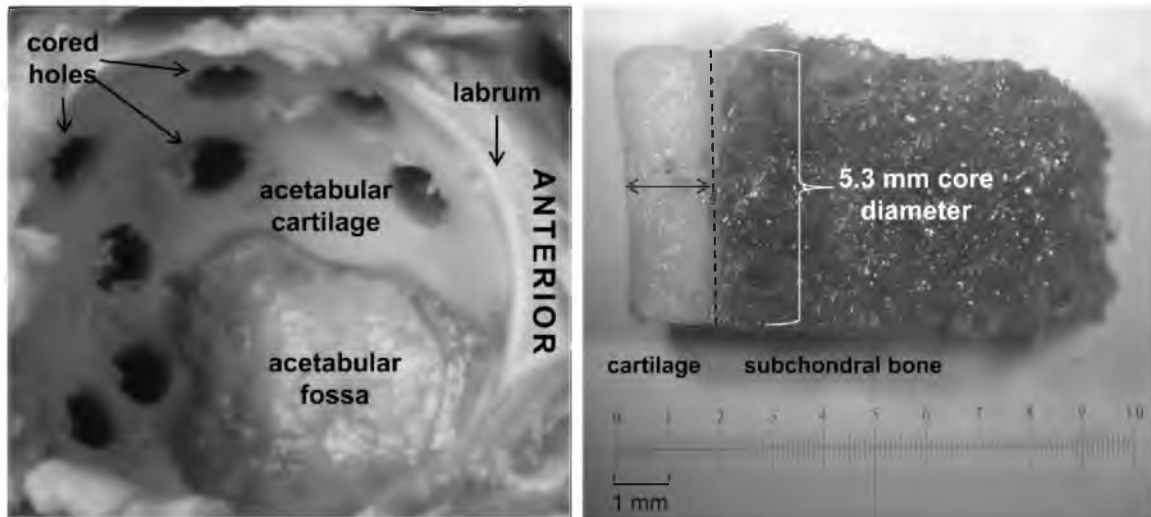


Figure 5.2. Photo illustration of cartilage core positioning and cross-sectional measurements. (left) Exposed acetabulum after 5.3 mm cartilage cores were harvested. (right) Digital microscope image of bisected core with micrometer at 25X magnification. The dashed line labels the bone-cartilage interface and the arrows indicate cartilage thickness measurement.

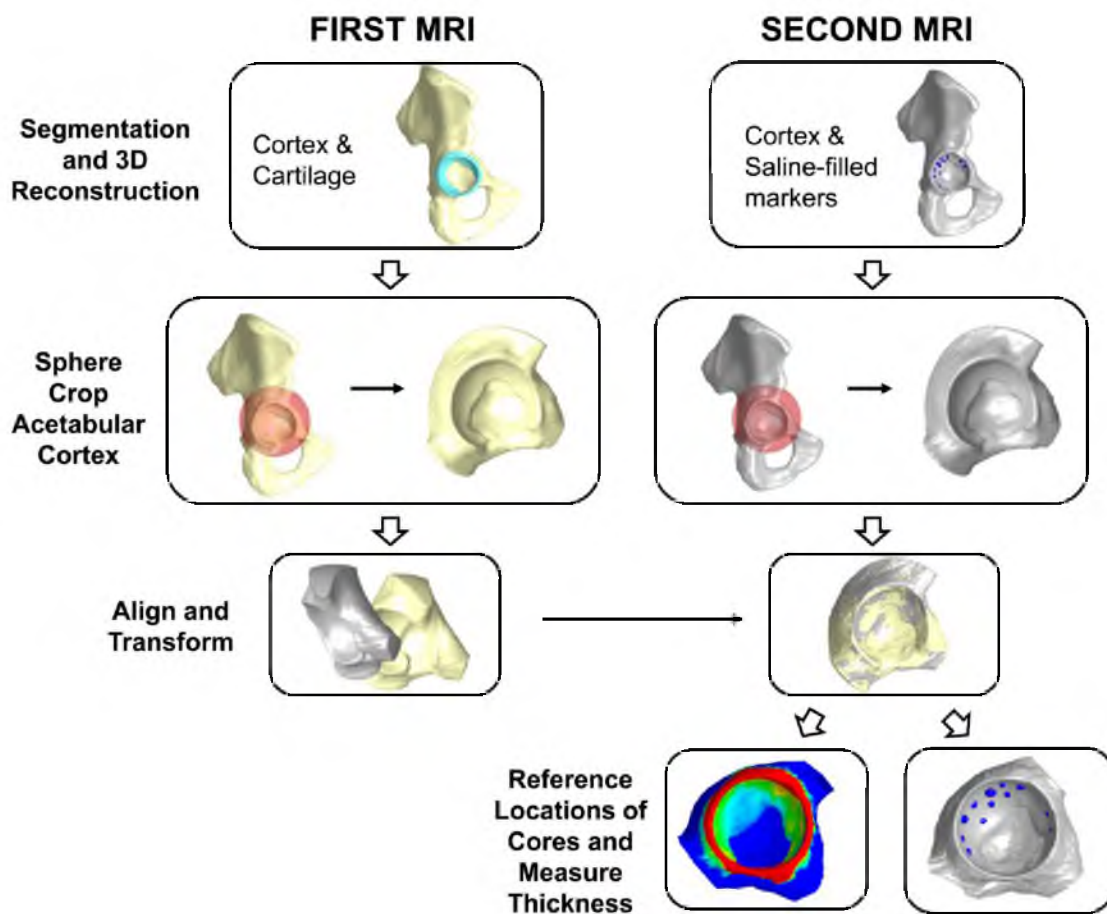


Figure 5.3. MRI postprocessing workflow. Analysis occurred from top to bottom with different stages designated by separate rows beginning with the segmentation and generation of surfaces and ending with the determination of cartilage thickness at marker locations.

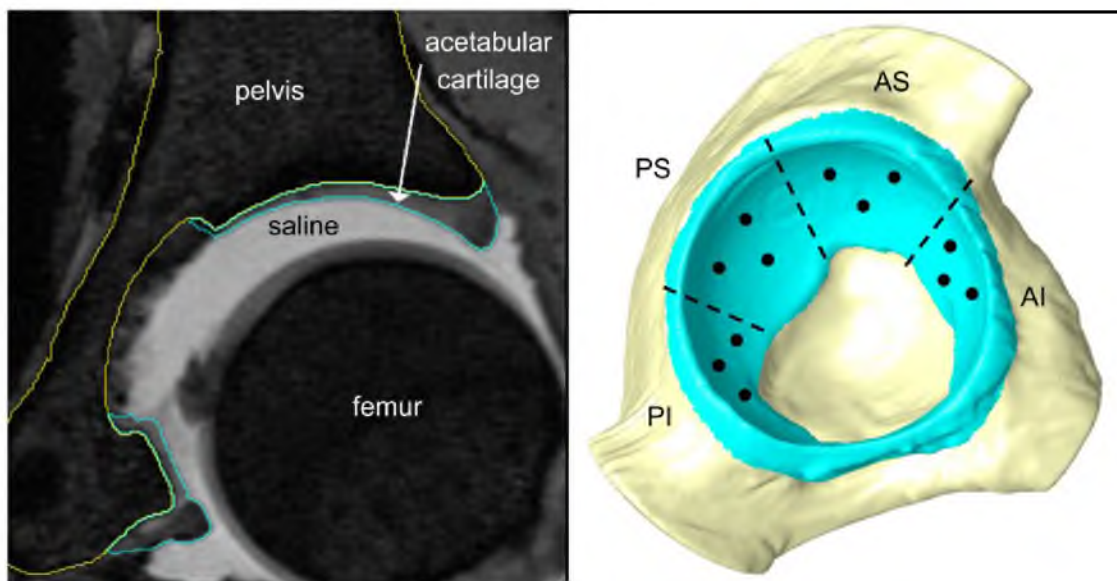


Figure 5.4. Segmentation and surface reconstructions of cortex and cartilage. (left) Midjoint coronal slice of DESS MRI with bone, cartilage, and saline clearly visualized. The acetabular cortex and cartilage automatically defined segmentation masks are outlined in yellow and blue, respectively. (right) Lateral view of surface reconstruction of acetabular cortex and cartilage with anteroinferior (AI), anterosuperior (AS), posteroinferior (PI), posterosuperior (PS) regions identified and approximate locations of cartilage cores shown.

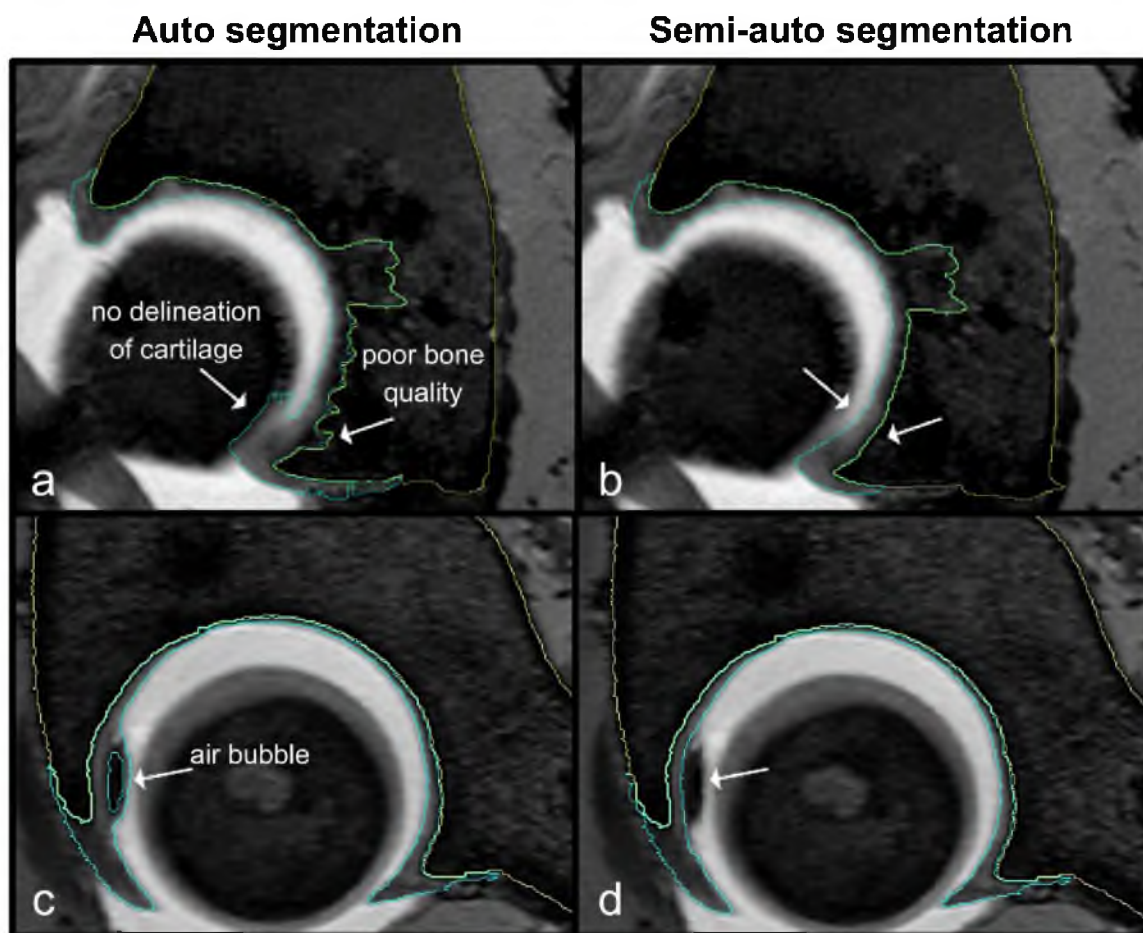


Figure 5.5. Regions where automatic segmentation failed to delineate bone-cartilage and cartilage-saline boundaries correctly on qualitative visual inspection. Coronal slice in the posterior acetabulum where (a) automatic segmentation did not properly identify bone-cartilage or cartilage-saline boundary. (b) Manual correction (indicated by arrows) was used to define bone boundary in the region of suspected low bone density and to define cartilage boundary where saline failed to delineate cartilage-saline boundary inferiorly. (c) Sagittal image where an air bubble introduced into the anterior joint space disrupted automatic segmentation of cartilage. (d) Segmentation was corrected manually at the site of the air bubble as indicated by the arrow.

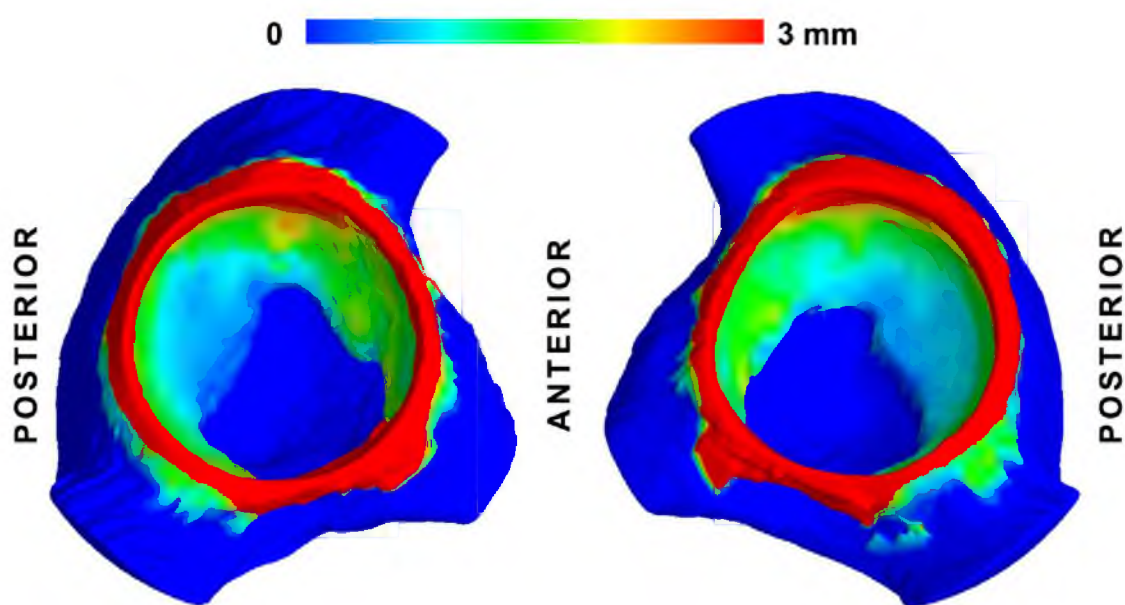


Figure 5.6. Cartilage thickness plots of both hips from one cadaver. The labrum was included in the cartilage surface reconstructions, and is much thicker than articular cartilage (indicated by the red color on the thickness plot); analysis of the thickness of the labrum was not performed. The thickest and thinnest cartilage is observed in the superolateral and posteromedial acetabulum, respectively.

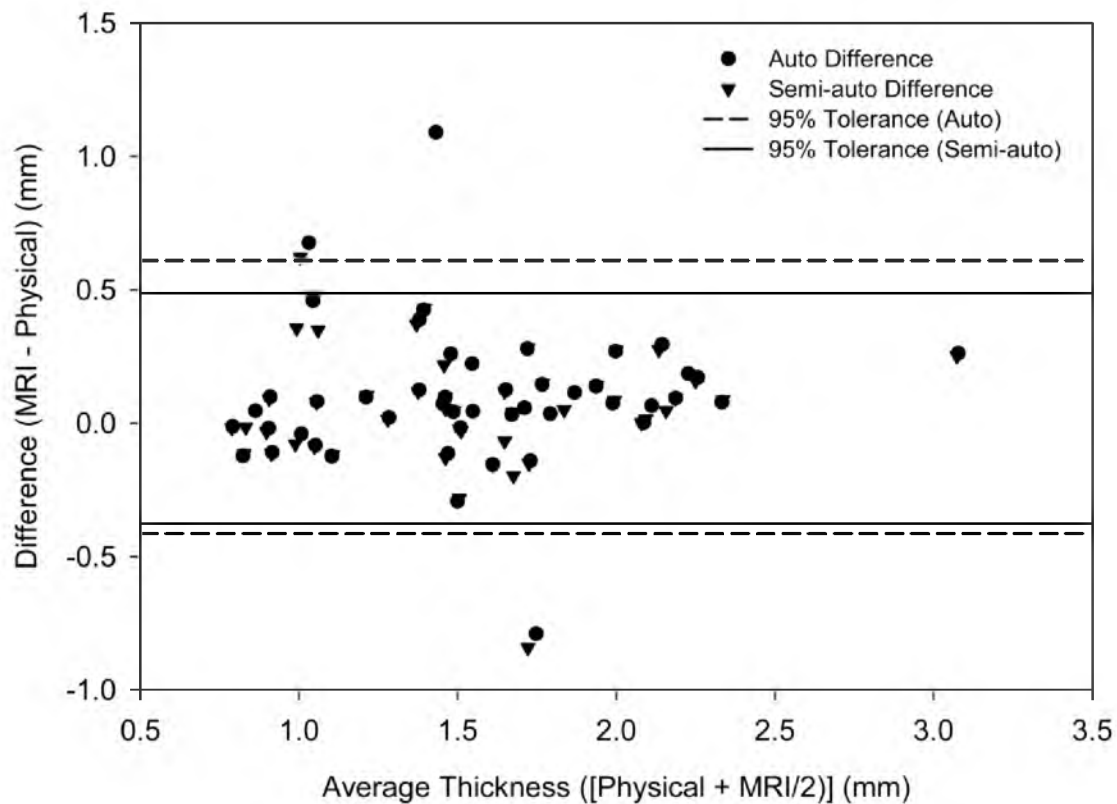


Figure 5.7. Bland Altman plots comparing physical and MRI measurements. The average thickness of physical and MRI measurement are plotted against the difference between physical and MRI measurements. Automatic and semi-automatic points are indicated by circles and triangles, respectively. Improved accuracy of semi-automatic segmentation is evidenced by tighter 95% tolerance limits for semi-automatic segmentation (solid lines) compared to those of automatic segmentation (dashed lines).

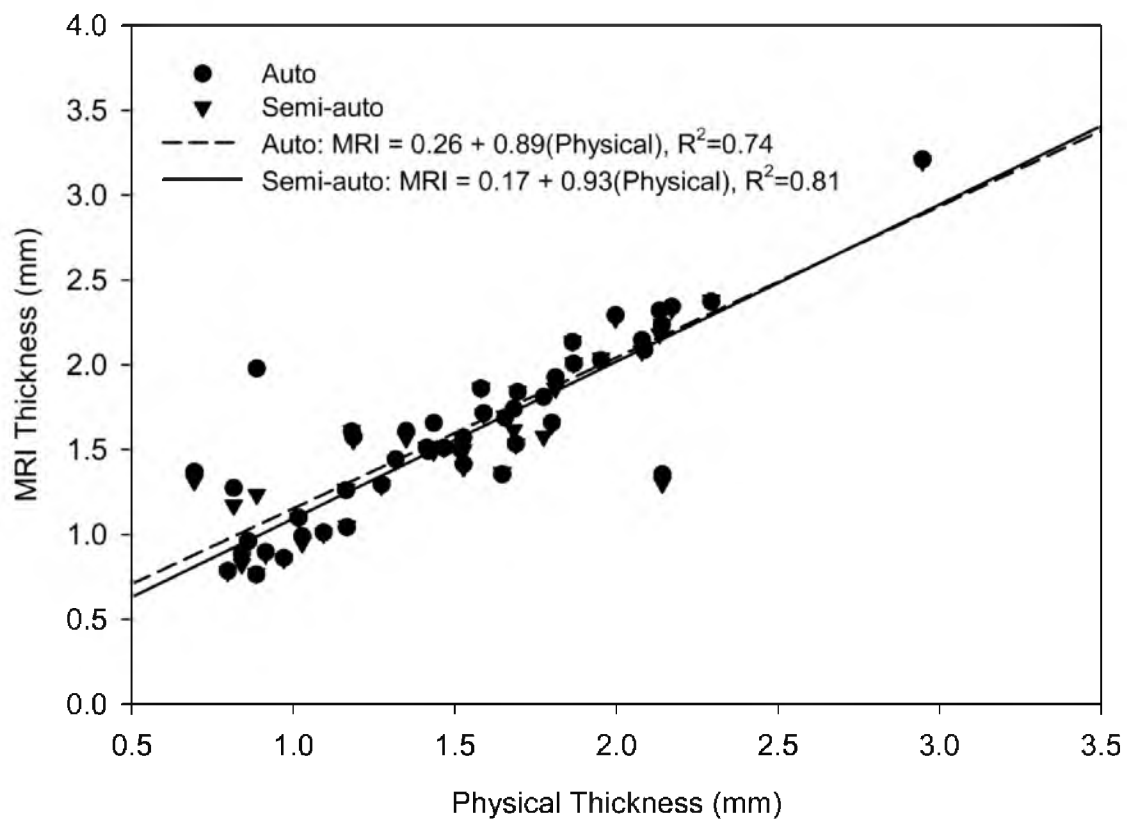


Figure 5.8. Scatterplot of physical thickness versus MRI thickness. Linear regressions of both automatic and semi-automatic MRI measurements demonstrated a strong predictive relationship with physical thickness ($R^2 = 0.74$ and 0.81 for auto and semi-auto) and near one-to-one correspondence (slopes approximately 1).

CHAPTER 6

CONCLUSION

6.1 Summary and Impact

At 20 year follow-up, nearly 40% of patients with acetabular dysplasia treated by PAO developed end-stage OA¹. Methods to improve and standardize the success of PAO would therefore be of great clinical value. Altered mechanics are believed to initiate OA in acetabular dysplasia^{2,3}. Accordingly, treatment should incorporate knowledge regarding the relationship between abnormal morphology and biomechanics. As concomitant deformities often present with acetabular dysplasia, diagnosis and treatment should be as objective as possible, analyzing the complex, 3D nature of the hip.

To date, most modeling approaches that have attempted to analyze hip mechanics before and after PAO have relied on over-simplifying assumptions, representing hip anatomy as a perfect sphere, or reducing the analysis to two dimensions. By accurately modeling the anatomy of the hip cartilage, bone, and labrum, this dissertation laid the foundation for enhancing our pre- and postoperative morphological and mechanistic understanding of acetabular dysplasia. More specifically, this dissertation: 1) quantified changes in femoral head coverage, cartilage thickness, congruency and chondrolabral contact mechanics following PAO performed by a single surgeon, 2) validated a

computationally efficient method for estimating hip contact mechanics, and 3) established 3D DESS MRI as an accurate volumetric imaging protocol. This chapter serves to summarize the findings, and discusses future work that could build upon the research herein.

6.1.1 Morphology and Mechanics in PAO

PAO has become the accepted surgical treatment for acetabular dysplasia. The objective of PAO is to restore normal joint mechanics by reorienting the acetabulum into a position that increases femoral head coverage. However, previous studies have not confirmed that PAO increases coverage and improves mechanics of the dysplastic hip using methods that include 3D patient-specific anatomy of living subjects.

Contrary to common belief, data from Chapter 2 demonstrated that femoral coverage did not significantly increase overall following PAO. Although lateral femoral coverage was found to significantly increase after PAO, medial coverage decreased; postoperative coverage was therefore balanced to the same percent found preoperatively. These data suggest that PAO is limited to improving coverage on a regional basis, at the sacrifice of reducing coverage in other regions.

Although overall femoral coverage may not be increased after PAO, model predictions from Chapter 3 demonstrated that contact mechanics did improve throughout the hip. In fact, cartilage contact stress was distributed more diffusely after PAO, which was likely the result of more balanced coverage between the medial and lateral regions. However, estimates of contact mechanics showed a great deal of variation between patients, and FE model predictions suggested that PAO did not improve mechanics in one

of the five patients, which was likely due to overcorrection. Our finding that contact stresses varied between patients was in agreement with prior modeling studies by our group. Specifically, we found larger variation in contact stress between individual patients than across loading scenarios for a single subject. Considering the variation in patient morphology, and that predictions of mechanics are unique to each patient, patient-specific biomechanical models may be useful to improve and standardize long-term results of PAO.

6.1.2 Accurate and Time-efficient Predictions of Mechanics

To integrate patient-specific mechanical analysis into clinical practice, more accessible and time-efficient methods are desired. In Chapter 4, DEA provided realistic distributions of cartilage contact stress about the acetabulum, and was able to complete the analysis in an average of 7 seconds; this is over 500 times faster than corresponding FE models. Prior DEA models of the hip were limited to assumptions of constant cartilage thickness, or modeling the joint as a sphere^{4,5}. Our research group has demonstrated that models that simplify cartilage geometry predict concentric contact patterns with reduced stress magnitudes and larger contact areas that are not supported by experimental studies⁶⁻¹⁰. Thus, the DEA model reported in Chapter 4 accurately incorporated cartilage thickness and underlying anatomy for the cortical bone. As a result, our DEA model provided physiologically realistic predictions of the distribution of cartilage contact stress.

Beyond the fast run time, other features of DEA make it feasible for clinical use. First, the intuitive nature of the representation of cartilage as springs is easily understood

by clinicians. Second, the computational ease makes DEA an ideal modeling approach that does not require substantial computing resources (models can be solved using processors common to a basic laptop computer). Though additional validation studies would be necessary, it is reasonable to assume the DEA protocol described herein could be extended to model contact mechanics in other joints besides the hip.

While DEA is computationally efficient, certain modeling assumptions cause DEA to over-estimate contact stresses. Specifically, compared to FE estimates of stress, DEA predicted an average increase of 43% and 44% in mean and median cartilage contact stresses. The discrepancy in stress magnitudes can be explained by the manner in which contact is modeled using DEA. In FEA, opposing layers of cartilage are modeled as distinct bodies in contact. However, with DEA contact is modeled as the deformation of a single spring between two rigid bodies (representing cortical bone of the acetabulum and femur). Also, the spring model in DEA did not simulate the lateral response of cartilage under compression due to Poisson's Effect. Despite the fact that DEA over-estimated contact stress magnitude, the overall distribution of contact stress (i.e. contact pattern) compared well between FE and DEA- contact areas were estimated within 10% of FE predictions. Therefore, DEA may be effective for applications where contact distributions and contact area are more important than stress magnitudes. For example, the development of an optimization routine for preoperative planning of PAO could be well suited for DEA. DEA could efficiently optimize the position of the acetabulum to minimize average contact stress, or maximize contact area. It would be computationally expensive to use FE modeling for this purpose as each model requires about 60 minutes of processing time using advanced computing servers. Conversely, the DEA model

would only require approximately 7 seconds, allowing one to analyze several simulated rotations of the acetabulum in a very short period of time.

6.1.3 3D DESS MRI of the Hip

Imaging is critical to both clinical and research applications in orthopaedics. For example, imaging is required to diagnose dysplasia, and provides the geometry of 3D biomechanical models. Improved methods to acquire high-resolution volumetric images that visualize bone, cartilage, and labrum could standardize the diagnosis of dysplasia and possibly expedite the development of 3D computer models. Results from Chapter 5 showed that using 3D DESS MRI with intra-articular saline injection and traction, acetabular cartilage thickness measurements obtained from automatically segmented 3D reconstructions can be estimated within ~0.5 mm of the gold standard with 95% confidence. This accuracy is among the best reported for measuring acetabular cartilage thickness from volumetric images, including CTA¹¹⁻¹³.

Beyond improvements in accuracy, the MRI protocol described in Chapter 5 offers additional benefits for clinical care and basic science research. First, considering the increase in the number of patients diagnosed and treated for developmental hip disorders within the past decade, imaging with MRI alleviates concerns with radiation exposure. This is especially true given that the patient population presenting with dysplasia consists of young adults who may require numerous evaluations throughout their lifetime. The use of intra-articular injection of nonionic CT contrast agents such as iopamidol has been linked to the development of insidious hip pain¹⁴. Anesthetics are commonly added to numb the hip during injection of contrast media. Within the last few

years, reports have recently surfaced that use of anesthetics during intra-articular injection may induce chondrocyte and synovial cell apoptosis^{15,16}. Therefore, a second benefit of the described DESS protocol is that it only requires saline, an inert and biocompatible substance, to serve as the intra-articular contrast media. Finally, from both clinical and research perspectives, DESS could streamline the process to generate 3D reconstructions of bone and cartilage. Specifically, using DESS, bone, cartilage, and intra-articular saline have different intensities. Conversely, cortical bone and injected contrast have similar attenuations on CTA images. Therefore, automatic segmentation, based on thresholding alone, could generate surface reconstructions in a fraction of the time compared to CTA.

6.2 Limitations and Future Directions

Although the studies presented within this dissertation provide the foundations for integrating biomechanical analysis into the clinical setting, there are limitations that should be addressed in the context of future research.

Estimating hip contact mechanics with computational models is limited by the modeling assumptions. While the finite element models used to evaluate changes in mechanics after PAO are the most complex and geometrically accurate models in the literature, refinements are possible. For example, cartilage and labrum material properties were assumed from the literature for bovine tissue, and were homogeneously distributed throughout these soft-tissue structures. Future research could quantify material properties and constitutive behavior of human tissue. Ideally, the constitutive models would consider the time- and loading-dependent nature of the tissues as well as

site-specific properties. While prior studies have determined that model predictions of contact mechanics are relatively insensitive to subject-specific and site-specific properties for articular cartilage, predictions of transchondral mechanics are indeed dependent on material models and coefficients^{17,18}. Future modeling studies that incorporate more detailed constitutive models could evaluate changes in transchondral mechanics in the normal and dysplastic hips. Use of physiologic material models may also provide more accurate predictions of shear stress at the cartilage-bone and cartilage-labrum boundaries, which represent the locations where damage is observed clinically.

Patients with acetabular dysplasia have altered kinematics and kinetics¹⁹⁻²¹, but the boundary and loading conditions incorporated herein were generalized and applied from a group of patients treated for THA²². Also, kinematics were held constant between patients, with only the applied load varying according to the body weight of the patient. The need for patient-specific boundary and loading conditions could be assessed by quantifying joint articulation and load transfer in each patient. To incorporate patient-specific kinematics, skin marker tracking is unlikely to provide the resolution necessary to discern subtle differences across patients. However, high-speed dual fluoroscopy could provide submillimeter accuracy of patient-specific hip joint kinematics²³. By simultaneously measuring ground reaction forces during activities of daily living, joint reaction forces could be estimated using muscle modeling software. Together, joint kinematics (measured by dual fluoroscopy) and joint reaction forces (estimated by muscle models) would provide patient-specific boundary and loading conditions. FE predictions could then be compared between models that incorporate patient-specific boundary and loading conditions to those that utilize generic data from the literature.

Another limitation of this work was that the sample size was small. Though dysplasia is relatively common, the time-intensive nature of the studies described herein inherently limits the number of subjects that can be analyzed over a period of a few years. Also, patients imaged preoperatively with CTA may not reside within a reasonable distance from the University of Utah Medical Center, making follow-up difficult. Finally, the studies described herein required two CTA scans within a period of 1-2 years; many patients are averse to repeat CT scans. One focus of this dissertation was therefore to validate the accuracy of 3D DESS MRI as an alternative to CTA.

As noted in Chapters 1-3, dysplastic hips often present with concomitant deformities, including: acetabular retroversion, hypertropic labra, or impingement. As 2D projections of complex anatomy, radiographs often fail to comprehensively diagnosis dysplasia and the aforementioned deformities. Thus, it was very challenging to determine, a-priori, which patients would be ideal candidates for the studies presented in Chapters 2 and 3 based on radiographs alone. Therefore, a final limitation of the described work is that the cohort of dysplastic hips was not homogenous. Future research could utilize more advanced imaging, such as radial MRI/CT, and 3D reconstructions to exclude patients who may appear to be homogenous upon inspection of radiographs. Nevertheless, the research presented in Chapters 2 and 3 is the most comprehensive to date; subtle deformities in bone and cartilage were included. Also, by modeling the labrum in both pre- and postoperative states, the data from Chapter 3 demonstrate that load may continue to be increased in dysplastic hips following PAO. This finding is especially important as the awareness of labral pathology in dysplastic hips increases.

The techniques described within this body of work must be integrated to realize the end goal of transitioning biomechanical analysis into clinical care of acetabular dysplasia. To develop accurate biomechanical models, DESS MRI imaging is certainly a promising sequence. However, the accuracy of DESS MRI may depend on image resolution and signal to noise ratio. Specifically, images described in Chapter 5 were acquired using a 3 Tesla (T) scanner, but most clinical scanners are 1.5 T. Future research could compare 3D reconstructions generated using a 1.5 and 3.0 T magnet. Also, in the future, it will also be necessary to develop improved methods to apply traction to distract opposing layers of cartilage in the hip of living subjects. Chapter 5 established the accuracy of the DESS protocol in vitro. In practice, there are several challenges when imaging the hip using arthrography. For example, gradual release of traction during an MRI scan could induce motion artefact. Motion artefact is not an issue with CT as the scan typically lasts less than 15 seconds. Fortunately, prior studies have described the use of hip traction during MRI without reporting any problems, even for scan times that exceeded 10 minutes^{24,25}. Our lab is currently developing an MRI-compatible traction device that shows excellent potential to distract the hip while limiting motion artifact.

With a DESS imaging protocol in place, modeling studies could be streamlined with automatic segmentation. In Chapter 2, changes in femoral coverage and acetabular and femoral cartilage thickness based on segmented surfaces were evaluated after PAO. While femoral coverage is not sensitive to minor differences in segmentation, the calculation of cartilage thickness is sure to be dependent on segmentation. Future studies could avoid the subjectivity of semiautomatic segmentation by using direct thresholding of DESS images as described in Chapter 5.

The subject-specific DEA hip model presented in Chapter 4, and the 3D DESS MR imaging sequence detailed in Chapter 5, could be used together to efficiently estimate mechanics in the clinical setting. Implementation of the DEA technique requires inputs for surface reconstructions of the femur and pelvis bone with cartilage thickness calculated at the articulating nodes. With cartilage and bone surfaces automatically segmented using 3D DESS MRI, subject-specific DEA models could be generated in substantially less time than the current method that requires manual adjustment to segmentation. Together, generating surface reconstructions from DESS MRI has the potential to diagnose and plan surgical treatment options for patients. Diagnosis with biomechanical models could identify which region of the acetabulum is overloaded, and an optimization routine could be used to determine the optimal reorientation for PAO to minimize contact stress. This framework for generating patient-specific surgical plans for PAO has been attempted by other research groups; however, accurate cartilage geometry has not been integrated into prior studies^{4,26}.

The final hurdle in implementing patient-specific diagnosis and treatment of acetabular dysplasia relies on accurately replicating the optimized surgical plan in the operating room. With advanced computer navigation systems, it is possible to follow predetermined surgical plans either by tracking the position of the acetabulum after it is separated from the pelvis during PAO^{27,28}. However, the more practical method would be to integrate the DEA hip model with a computer navigation system to provide real-time estimates of contact stress distributions based on the position of the acetabulum. The surgeon could alter the degree of rotation until he/she was satisfied with both the intra-operative fluoroscopic measures and analysis of hip contact mechanics.

Though results of long-term studies of PAO are mixed¹, it is reasonable to assume that the procedure has been refined over time. Accordingly, performed today by an experienced surgeon, PAO may have better success rates than those reported from procedures performed decades ago. However, outcomes could likely be further improved if a biomechanical analysis were integrated into the clinical care of acetabular dysplasia. To substantiate such claims, patients would need follow-up imaging with methods such as DESS MRI to closely monitor the progression of hip OA. Biochemical MR imaging, which seeks to quantify cartilage health in-vivo, is a relatively new area of musculoskeletal imaging that has great potential. Different techniques including T2 mapping, ADC mapping, and dGEMRIC have been used to detect early cartilage deterioration²⁹⁻³¹. Each technique targets a different component of articular cartilage to assess cartilage biochemical integrity. Therefore, these methods have the potential to detect early cartilage damage before significant irreversible degeneration has occurred. From diagnosis through treatment monitoring, biochemical MRI could play an important role in clinical care. However, additional research is necessary to support the validity of biochemical imaging and establish its role for conditions such as hip dysplasia. In this regard, hip contact mechanics could be correlated to biochemical imaging findings to better understand the role between altered mechanics and development of early hip OA. If such relationships were established, it may be possible to predict hip biomechanics using biochemical imaging findings alone. In other words, it would not be necessary to develop complex computer models on a per-patient basis. Biochemical imaging using MRI is therefore an important area of orthopaedic research and could greatly impact the clinical care of hip dysplasia.

In summary, the research presented in the context of the body of this dissertation provides critical insights into the mechanics of the dysplastic hips before and after surgery. By including the complex, 3D anatomy of bone, cartilage, and labrum, we successfully quantified morphological changes following PAO. The implementation of a DEA protocol that incorporates subject-specific cartilage geometry provides a platform for future work to develop optimized surgical plans for PAO on a per-patient basis. Finally, successful application of the validated 3D DESS MRI protocol to a cohort of living subjects in the future could substantiate a noninvasive imaging protocol of the hip that would provide accurate reconstructions of cartilage anatomy without the added risk of ionizing radiation.

6.3 References

1. Steppacher SD, Tannast M, Ganz R, et al. 2008. Mean 20-year followup of Bernese periacetabular osteotomy. *Clinical orthopaedics and related research* 466: 1633-1644.
2. Ganz R, Leunig M, Leunig-Ganz K, et al. 2008. The etiology of osteoarthritis of the hip: an integrated mechanical concept. *Clinical orthopaedics and related research* 466: 264-272.
3. Jacobsen S, Sonne-Holm S. 2005. Hip dysplasia: a significant risk factor for the development of hip osteoarthritis. A cross-sectional survey. *Rheumatology* 44: 211-218.
4. Armiger RS, Armand M, Tallroth K, et al. 2009. Three-dimensional mechanical evaluation of joint contact pressure in 12 periacetabular osteotomy patients with 10-year follow-up. *Acta orthopaedica* 80: 155-161.
5. Yoshida H, Faust A, Wilckens J, et al. 2006. Three-dimensional dynamic hip contact area and pressure distribution during activities of daily living. *Journal of biomechanics* 39: 1996-2004.
6. Adams D, Swanson SA. 1985. Direct measurement of local pressures in the cadaveric human hip joint during simulated level walking. *Annals of the rheumatic diseases* 44: 658-666.
7. Afoke NY, Byers PD, Hutton WC. 1987. Contact pressures in the human hip joint. *The Journal of bone and joint surgery British volume* 69: 536-541.
8. Anderson AE, Ellis BJ, Maas SA, et al. 2008. Validation of finite element predictions of cartilage contact pressure in the human hip joint. *Journal of biomechanical engineering* 130: 051008.
9. Anderson AE, Ellis BJ, Maas SA, et al. 2010. Effects of idealized joint geometry on finite element predictions of cartilage contact stresses in the hip. *Journal of biomechanics* 43: 1351-1357.
10. Brown TD, Shaw DT. 1983. In vitro contact stress distributions in the natural human hip. *Journal of biomechanics* 16: 373-384.
11. Allen BC, Peters CL, Brown NA, et al. 2010. Acetabular cartilage thickness: accuracy of three-dimensional reconstructions from multidetector CT arthrograms in a cadaver study. *Radiology* 255: 544-552.

12. Tamura S, Nishii T, Shiomi T, et al. 2012. Three-dimensional patterns of early acetabular cartilage damage in hip dysplasia; a high-resolution CT arthrography study. *Osteoarthritis and cartilage / OARS, Osteoarthritis Research Society* 20: 646-652.
13. Wyler A, Bousson V, Bergot C, et al. 2009. Comparison of MR-arthrography and CT-arthrography in hyaline cartilage-thickness measurement in radiographically normal cadaver hips with anatomy as gold standard. *Osteoarthritis and cartilage / OARS, Osteoarthritis Research Society* 17: 19-25.
14. Weiland FL, Marti-Bonmati L, Lim L, et al. 2013. Comparison of patient comfort between iodixanol and iopamidol in contrast-enhanced computed tomography of the abdomen and pelvis: a randomized trial. *Acta radiologica* 55: 715-724.
15. Grishko V, Xu M, Wilson G, et al. 2010. Apoptosis and mitochondrial dysfunction in human chondrocytes following exposure to lidocaine, bupivacaine, and ropivacaine. *The Journal of bone and joint surgery American volume* 92: 609-618.
16. Rao AJ, Johnston TR, Harris AH, et al. 2014. Inhibition of chondrocyte and synovial cell death after exposure to commonly used anesthetics: chondrocyte apoptosis after anesthetics. *The American journal of sports medicine* 42: 50-58.
17. Henak CR, Ateshian GA, Weiss JA. 2014. Finite element prediction of transchondral stress and strain in the human hip. *Journal of biomechanical engineering* 136: 021021.
18. Henak CR, Kapron AL, Anderson AE, et al. 2014. Specimen-specific predictions of contact stress under physiological loading in the human hip: validation and sensitivity studies. *Biomechanics and modeling in mechanobiology* 13: 387-400.
19. Jacobsen JS, Nielsen DB, Sorensen H, et al. 2013. Changes in walking and running in patients with hip dysplasia. *Acta orthopaedica* 84: 265-270.
20. Pedersen EN, Simonsen EB, Alkjaer T, et al. 2004. Walking pattern in adults with congenital hip dysplasia: 14 women examined by inverse dynamics. *Acta orthopaedica Scandinavica* 75: 2-9.
21. Romano CL, Frigo C, Randelli G, et al. 1996. Analysis of the gait of adults who had residua of congenital dysplasia of the hip. *The Journal of bone and joint surgery American volume* 78: 1468-1479.
22. Bergmann G, Deuretzbacher G, Heller M, et al. 2001. Hip contact forces and gait patterns from routine activities. *Journal of biomechanics* 34: 859-871.

23. Kapron AL, Aoki SK, Peters CL, et al. 2014. Accuracy and Feasibility of Dual Fluoroscopy and Model-Based Tracking to Quantify In Vivo Hip Kinematics During Clinical Exams. *Journal of applied biomechanics*.
24. Nakanishi K, Tanaka H, Nishii T, et al. 1999. MR evaluation of the articular cartilage of the femoral head during traction. Correlation with resected femoral head. *Acta radiologica* 40: 60-63.
25. Nishii T, Tanaka H, Nakanishi K, et al. 2005. Fat-suppressed 3D spoiled gradient-echo MRI and MDCT arthrography of articular cartilage in patients with hip dysplasia. *AJR American journal of roentgenology* 185: 379-385.
26. Tsumura H, Kaku N, Ikeda S, et al. 2005. A computer simulation of rotational acetabular osteotomy for dysplastic hip joint: does the optimal transposition of the acetabular fragment exist? *Journal of orthopaedic science : official journal of the Japanese Orthopaedic Association* 10: 145-151.
27. Langlotz F, Nolte LP, Tannast M. 2006. [The foundations of computer assisted surgery]. *Der Orthopade* 35: 1032-1037.
28. Langlotz F, Stucki M, Bachler R, et al. 1997. The first twelve cases of computer assisted periacetabular osteotomy. *Computer aided surgery : official journal of the International Society for Computer Aided Surgery* 2: 317-326.
29. Apprich S, Mamisch TC, Welsch GH, et al. 2012. Evaluation of articular cartilage in patients with femoroacetabular impingement (FAI) using T2* mapping at different time points at 3.0 Tesla MRI: a feasibility study. *Skeletal radiology* 41: 987-995.
30. Bittersohl B, Miese FR, Hosalkar HS, et al. 2012. T2* mapping of hip joint cartilage in various histological grades of degeneration. *Osteoarthritis and cartilage / OARS, Osteoarthritis Research Society* 20: 653-660.
31. Ellermann J, Ziegler C, Nissi MJ, et al. 2014. Acetabular cartilage assessment in patients with femoroacetabular impingement by using T2* mapping with arthroscopic verification. *Radiology* 271: 512-523.